Global performance of covariant energy density functionals: Ground state observables of even-even nuclei and the estimate of theoretical uncertainties

S. E. Agbemava,[1] A. V. Afanasjev,[1] D. Ray,[1] and P. Ring[2]
[1]*Department of Physics and Astronomy, Mississippi State University, Mississippi State, Mississippi 39762, USA*
[2]*Fakultät für Physik, Technische Universität München, D-85748 Garching, Germany*
(Received 28 February 2014; revised manuscript received 18 April 2014; published 27 May 2014)

Covariant density functional theory is a modern theoretical tool for the description of nuclear structure phenomena. The current investigation aims at the global assessment of the accuracy of the description of the ground state properties of even-even nuclei. We also estimate *theoretical uncertainties* defined here as the spreads of predictions within four covariant energy density functionals in known regions of the nuclear chart and their propagation towards the neutron drip line. Large-scale axial relativistic Hartree-Bogoliubov calculations are performed for all $Z \leqslant 104$ even-even nuclei between the two-proton and two-neutron drip lines with four modern covariant energy density functionals such as NL3*, DD-ME2, DD-MEδ, and DD-PC1. The physical observables of interest include the binding energies, two-particle separation energies, charge quadrupole deformations, isovector deformations, charge radii, neutron skin thicknesses, and the positions of the two-proton and two-neutron drip lines. The predictions for the two-neutron drip line are also compared in a systematic way with the ones obtained in nonrelativistic models.

DOI: 10.1103/PhysRevC.89.054320 PACS number(s): 21.60.Jz, 21.10.Dr, 21.10.Ft, 21.10.Gv

I. INTRODUCTION

Density functional theories (DFT's) are extremely useful for the microscopic description of quantum mechanical many-body systems. They map the complicated N-body systems on an effective systems of N uncorrelated single particles. They have been applied with great success for many years in Coulombic systems [1,2], where they are, in principle, exact and where the functional can be derived without any phenomenological adjustments directly from the Coulomb interaction. In nuclear physics the situation is much more complicated.

Nuclei are self-bound systems with translational invariance. Because of the large spin-orbit interaction spin degrees of freedom play an important role and cannot be neglected. There are also isospin degrees of freedom and many open-shell nuclei are superfluid systems. In addition, there are strong indications [3] that an optimal description of nuclei should be relativistic. As a consequence, the single-particle wave functions form at each point in r-space a spinor of dimension 4, or 8 (with superfluidity), or 16 (in the relativistic case).

The bare nuclear force is usually adjusted to scattering data. This requires additional assumptions and is connected with additional uncertainties such as the off-shell behavior. As compared to the Coulomb force, the two-body part of the nuclear force is extremely strong at short distances and has a relatively short range. There are convincing indications that it contains, on the nonrelativistic level, an important three-body part.

Despite all these restrictions, in the past 40 years nonrelativistic and relativistic (covariant) DFT's have been developed and successfully applied to the description of a variety of nuclear phenomena [4–7] with great success. All of these applications are based on phenomenological parametrizations of the underlying density functionals. Usually the form of these functionals is determined by arguments of symmetry and simplicity and the remaining set of parameters is fitted to experimental data in finite nuclei, such as binding energies, radii, etc. Only recently have there been attempts to reduce the number of phenomenological parameters by using information from *ab initio* calculations for nonrelativistic [8–10] and relativistic [11,12] functionals. It is clear, however, that the required accuracy of a few hundred keV for the binding energies, i.e., in heavy nuclei an accuracy of 10^{-4} and below, can, in the foreseeable future, only be achieved by additional fine tuning of a few extra phenomenological parameters.

Among these nuclear DFT's, covariant DFT is one of most attractive because covariant energy density functionals exploit basic properties of QCD at low energies, such as symmetries and the separation of scales [5]. They provide a consistent treatment of the spin degrees of freedom and include the complicated interplay between the large Lorentz scalar and vector self-energies induced on the QCD level by the in-medium changes of the scalar and vector quark condensates [13]. In addition, these functionals include *nuclear magnetism* [14], i.e., a consistent description of currents and time-odd mean fields important for odd-mass nuclei [15], the excitations with unsaturated spins, magnetic moments [16], and nuclear rotations [17,18]. Because of Lorentz invariance no new adjustable parameters are required for the time-odd parts of the mean fields. Of course, at present, all attempts to derive these functionals directly from the bare forces [19–22] do not reach the required accuracy. However, in recent years modern phenomenological covariant density functionals have been derived [11,12,23] which provide an excellent description of ground and excited states all over the nuclear chart [6,7] with a high predictive power. Modern versions of these forces derive the density dependence of the vertices from state-of-the-art *ab initio* calculations and use only the remaining few parameters for a fine tuning of experimental masses in finite spherical [12] or deformed [11] nuclei.

The theoretical description of ground state properties of nuclei is important for our understanding of their structure. It is also important for nuclear astrophysics, where we are facing the problem of an extrapolation to the nuclei with large isospin. Many of such nuclei will never be studied experimentally, even with the next generation of facilities. Thus, it is important to answer two questions. First, how well do the existing nuclear energy density functionals (EDF's) describe available experimental data? Second, how well do they extrapolate to the region of unknown nuclei?

Unfortunately, even the answer on the first question is not possible for the majority of nuclear EDF's because their global performance is not known. This is especially true for covariant energy density functionals. Very few of them were confronted with experimental data on a global scale. Even the new generation of covariant energy density functionals (CEDF's) such as NL3* [24], DD-ME2 [23], DD-MEδ [12], and DD-PC1 [11], which were fitted during past decade, have not passed this critical test. This is because only limited sets of nuclei, usually located in the region of nuclei used in the fitting protocol, were confronted with calculations. Thus, it is not known how well they describe ground state properties on a global scale and what are their strong and weak points in that respect.

The answer to the question "How well does a given CEDF extrapolate towards neutron-rich nuclei?" is intimately connected with the answer to the first question. This is because one can estimate its reliability for the description of nuclei far away from the region of known nuclei only by assessing its global performance on existing experimental data. Of course, a good performance in known nuclei is only a necessary condition and one has to be very careful with extrapolations of models where this good performance has only been achieved with a large number of phenomenological parameters. It is one of the essential advantages of relativistic models that covariance reduces the number of parameters considerably.

It was suggested in Refs. [25–27] to use the methods of information theory and to define the uncertainties in the EDF parameters. These uncertainties come from the selection of the form of EDF as well as from the fitting protocol details, such as the selection of the nuclei under investigation, the physical observables, or the corresponding weights. Some of them are called *statistical errors* and can be calculated from a statistical analysis during the fit, others are systematic errors, such as, for instance, the form of the EDF under investigation. On the basis of these statistical errors and under certain assumptions on the independence of the form of many EDF's one hopes to be able to deduce in this way *theoretical error bars* for the prediction of physical observables [25–27]. It is very difficult to perform the analysis of statistical errors on a global scale because the properties of transitional and deformed nuclei have to be calculated repeatedly for different variations of original CEDF. Thus, such statistical analysis has been performed mostly for spherical nuclei [25,28] or selected isotopic chains of deformed nuclei [26].

Although such an analysis has its own merits, at present, it does not allow to fully estimate theoretical uncertainties in the description of physical observables. This is because they originate not only from the uncertainties in model parameters, but also from the definition and the limitations of the model itself, in particular, from an insufficient form of the nuclear energy density functional. The later uncertainties are very difficult to estimate. As a consequence, any analysis of theoretical uncertainties (especially, for extrapolations to neutron-rich nuclei) contains a degree of arbitrariness related to the choice of the model and fitting protocol.

Thus, in the given situation we concentrate mostly on the uncertainties related to the present choice of energy density functionals which can be relatively easily deduced globally. We therefore define *theoretical systematic uncertainties* for a given physical observable via the spread of theoretical predictions within the four CEDF's,

$$\Delta O(Z,N) = |O_{\max}(Z,N) - O_{\min}(Z,N)|, \qquad (1)$$

where $O_{\max}(Z,N)$ and $O_{\min}(Z,N)$ are the largest and smallest values of the physical observable $O(Z,N)$ obtained with the four employed CEDF's for the (Z,N) nucleus. In the following we use the word *spread* for these theoretical systematic uncertainties for the CEDF's. Three different classes of the CEDF's are used for this purpose (see Sec. II). Note that these *theoretical uncertainties* are only spreads of physical observables owing to a very small number of functionals and, thus, they are only a crude approximation to the *systematic theoretical errors* discussed in Ref. [27]. As in the case of present Skyrme functionals, the different covariant functionals do not form an independent statistical ensemble. Their number is very small and they are all based on a very similar form. For example, no tensor terms are present in the relativistic case and simple power laws are used for the density dependence in the Skyrme DFT. The parameters of these functionals are fitted according to similar protocols, including similar types of physical observables such as binding energies and radii.

Thus, there are two main goals of the current paper. First is the assessment of global performance of the state-of-the art CEDF's. In the future it will make it possible to define the strategies for new fits of CEDF's. The second goal is to estimate differences in the description of various physical observables on a global scale and especially in the regions of unknown nuclei.

The paper is organized as follows. The four state-of-the-art covariant energy density functionals and the details of their fitting protocols are discussed in Sec. II. Section III describes the solutions of the relativistic Hartree-Bogoliubov equations. The treatment of the pairing interaction and the selection of its strength are considered in Sec. IV. We report on the results for masses (binding energies) and two-particle separation energies in Secs. V and VI, respectively. Section VII contains a discussion of the two-proton drip line and the accuracy of its description in model calculations. The predictions for the two-neutron drip line, an analysis of sources for uncertainties of its definition, and a comparison of two-neutron drip-line predictions of covariant and nonrelativistic DFT's are presented in Sec. VIII. Calculated charge quadrupole and hexadecapole deformations and isovector quadrupole deformations are considered in Sec. IX. Charge radii and neutron skin thicknesses are discussed in Sec. X. Note that theoretical uncertainties of relevant physical observables are

discussed in each of Secs. V, VI, VII, VIII, IX, and X. Finally, Sec. XI summarizes the results of our work.

II. COVARIANT ENERGY DENSITY FUNCTIONALS

Three classes of covariant density functional models are used throughout this paper: the nonlinear meson-nucleon coupling model (NL), the density-dependent meson-exchange (DD-ME) model, and the density-dependent point-coupling (DD-PC) model. The main differences between them lie in the treatment of the range of the interaction and in the density dependence. The interaction in the first two classes has a finite range that is determined by the mass of the mesons. For fixed density it is of Yukawa type and the range is given by the inverse of the meson masses. For large meson masses, i.e., for small ranges, the meson propagator can be expanded in terms of this range. In zeroth order we obtain δ forces and in higher order derivative terms. This leads to the third class of density functionals, the point-coupling models. It is well known from the nonrelativistic Skyrme functionals that pure δ-forces are not able to describe properly at the same time nuclear binding energies and radii. One needs at least one derivative term in the isoscalar-scalar channel because the σ mass is considerably smaller than the masses of the other mesons.

For realistic calculations the density dependence is very important. It is taken into account by nonlinear meson couplings in the NL models and by an explicit density dependence of the coupling constants in the other two cases, i.e., by density-dependent meson-nucleon vertices in the DD-ME and DD-PC models.

Each of these classes is represented in the current paper by the CEDF's considered to be state-of-the-art, i.e., by NL3* [24] for the NL models, by DD-ME2 [23] and DD-MEδ [12] for the DD-ME models, and by DD-PC1 [11] for the point-coupling models.

In the meson-exchange models [12,23,24], the nucleus is described as a system of Dirac nucleons interacting via the exchange of mesons with finite masses leading to finite-range interactions. The starting point of covariant density functional theory (CDFT) for these two models is a standard Lagrangian density [29],

$$\begin{aligned}\mathcal{L} = {} & \bar{\psi}[\gamma\cdot(i\partial - g_\omega\omega - g_\rho\vec{\rho}\,\vec{\tau} - eA) - m - g_\sigma\sigma - g_\delta\vec{\tau}\vec{\delta}]\psi \\ & + \tfrac{1}{2}(\partial\sigma)^2 - \tfrac{1}{2}m_\sigma^2\sigma^2 + \tfrac{1}{2}(\partial\vec{\delta})^2 - \tfrac{1}{2}m_\delta^2\vec{\delta}^2 \\ & - \tfrac{1}{4}\Omega_{\mu\nu}\Omega^{\mu\nu} + \tfrac{1}{2}m_\omega^2\omega^2 - \tfrac{1}{4}\vec{R}_{\mu\nu}\vec{R}^{\mu\nu} + \tfrac{1}{2}m_\rho^2\vec{\rho}^{\,2} \\ & - \tfrac{1}{4}F_{\mu\nu}F^{\mu\nu}, \end{aligned} \tag{2}$$

which contains nucleons described by the Dirac spinors ψ with the mass m and several effective mesons characterized by the quantum numbers of spin, parity, and isospin. They create effective fields in a Dirac equation, which corresponds to the Kohn-Sham equation [1] of nonrelativistic DFT. The Lagrangian (2) contains as parameters the meson masses m_σ, m_ω, m_δ, and m_ρ and the coupling constants g_σ, g_ω, g_δ, and g_ρ. e is the charge of the protons and it vanishes for neutrons.

This linear model has first been introduced by Walecka [30,31]. However, it has failed to describe the surface properties of realistic nuclei. In particular, the resulting incompressibility of infinite nuclear matter is much too large [32] and nuclear deformations are too small [29]. Therefore, Boguta and Bodmer [32] introduced a density dependence via a nonlinear meson coupling replacing the term $\frac{1}{2}m_\sigma^2\sigma^2$ in Eq. (2) with

$$U(\sigma) = \tfrac{1}{2}m_\sigma^2\sigma^2 + \tfrac{1}{3}g_2\sigma^3 + \tfrac{1}{4}g_3\sigma^4. \tag{3}$$

The nonlinear meson-coupling models are represented by the parameter set NL3* [24] (see Table I), which is a modern version of the widely used parameter set NL3 [33]. Both contain no δ meson. Apart from the fixed values for the masses m, m_ω, and m_ρ, there are six phenomenological parameters, m_σ, g_σ, g_ω, g_ρ, g_2, and g_3, which have been fitted in Ref. [24] to a set experimental data in spherical nuclei: 12 binding energies, 9 charge radii, and 4 neutron skin thicknesses.

The density-dependent meson-nucleon coupling model has an explicit density dependence for the meson-nucleon vertices. There are no nonlinear terms for the σ meson, i.e., $g_2 = g_3 = 0$. For the form of the density dependence the Typel-Wolter

TABLE I. The parameters of the NL3*, DD-ME2, and DD-MEδ CEDF's. The masses are given in MeV and the dimension of g_2 in NL3* is fm^{-1}. All other parameters are dimensionless. Note that $g_\sigma = g_\sigma(\rho_{\rm sat})$, $g_\omega = g_\omega(\rho_{\rm sat})$, $g_\delta = g_\delta(\rho_{\rm sat})$, and $g_\rho = g_\rho(\rho_{\rm sat})$ in the case of the DD-ME2 and DD-MEδ CEDF's.

Parameter	NL3*	DD-ME2	DD-MEδ
m	939	939	939
m_σ	502.5742	550.1238	566.1577
m_ω	782.600	783.000	783.00
m_δ			983.0
m_ρ	763.000	763.000	763.0
g_σ	10.0944	10.5396	10.3325
g_ω	12.8065	13.0189	12.2904
g_δ			7.152
g_ρ	4.5748	3.6836	6.3128
g_2	−10.8093		
g_3	−30.1486		
a_σ		1.3881	1.3927
b_σ		1.0943	0.1901
c_σ		1.7057	0.3679
d_σ		0.4421	0.9519
e_σ		0.4421	0.9519
a_ω		1.3892	1.4089
b_ω		0.9240	0.1698
c_ω		1.4620	0.3429
d_ω		0.4775	0.9860
e_ω		0.4775	0.9860
a_δ			1.5178
b_δ			0.3262
c_δ			0.6041
d_δ			0.4257
e_δ			0.5885
a_ρ		0.5647	1.8877
b_ρ			0.0651
c_ρ			0.3469
d_ρ			0.9417
e_ρ			0.9737

ansatz [34] has been used,

$$g_i(\rho) = g_i(\rho_{\rm sat}) f_i(x) \quad \text{for} \quad i = \sigma,\omega,\delta,\rho, \tag{4}$$

where the density dependence is given by [12,23,34]

$$f_i(x) = a_i \frac{1 + b_i(x + d_i)^2}{1 + c_i(x + e_i)^2}, \tag{5}$$

where x is defined as the ratio between the baryonic density ρ at a specific location and the baryonic density at saturation $\rho_{\rm sat}$ in symmetric nuclear matter. The parameters in Eq. (5) are not independent, but constrained as follows: $f_i(x = 1) = 1$, $f_\sigma''(x = 1) = f_\omega''(x = 1)$, and $f_i''(x = 0) = 0$. In addition, the constraints $d_\sigma = e_\sigma$ and $d_\omega = e_\omega$ are used. These constraints reduce the number of independent parameters for the density dependence. The density-dependent meson-nucleon coupling model is represented here by the CEDF's DD-ME2 [23] and DD-MEδ [12]. The selection of DD-MEδ in this class is motivated by the desire to understand the role of the extra (δ) meson. Note that in the case of DE-ME2 we have no δ meson and the density dependence of Eq. (5) is used only for the σ and ω mesons. For the ρ meson we have an exponential density dependence,

$$f_\rho(x) = \exp[-a_\rho(x - 1)], \tag{6}$$

in DD-ME2.

There is an important difference between the functional NL3* and three other functionals considered in this investigation. NL3*, as all older nonlinear meson coupling functionals like NL1 [35], NL3 [33], or TM1 [36], have no nonlinearities in the isovector channel. Therefore, in infinite nuclear matter, the isovector fields are proportional to the isovector density, which are given by $N - Z$. This leads to a very stiff symmetry energy as a function of the density and to relatively large values for the symmetry energy J and its slope L at saturation (see Table V). J is particularly large in NL1. The fits of other above-mentioned nonlinear meson coupling functionals have tried to reduce this value. However, because of the stiffness of the linear ansatz this is possible only to a certain extent. Although these functionals are very successful for static CDFT close to the valley of stability [24], their common feature is that the neutron skin thicknesses are larger than those of successful Skyrme EDF's and DD CEDF's (see Sec. X for more details). The majority of experimental estimates of the neutron skin thickness based on hadronic probes favor lower values for this quantity. However, these experimental values strongly depend on model assumptions. Only the central value of the neutron skin thickness obtained in the recent PREX [37] experiment is in agreement with CEDF's linear in the isovector channel. This experiment is, however, characterized by large statistical errors. On the other hand, the information on the symmetry energy (for more details concerning the present status of our knowledge on the symmetry energy in nuclei see Ref. [38]) from *ab initio* calculations and from isovector excitations such as the giant dipole resonance (GDR) indicate clearly that one needs a density dependence in the isovector channel [39], as we have it in the CEDF's DD-ME2, DD-MEδ, or DD-PC1.

For the functional DD-ME2 [23] the masses m, m_ω, and m_ρ are kept at fixed values. As discussed above the density dependence of the coupling constants $f_i(x)$ $i = \sigma,\omega,\rho$ is given by four independent parameters. Therefore, together with the four parameters m_σ, $g_\sigma(\rho_{\rm sat})$, $g_\omega(\rho_{\rm sat})$, and $g_\rho(\rho_{\rm sat})$ DD-ME2 contains eight independent parameters which have been fitted in Ref. [23] to a set experimental data in spherical nuclei: 12 binding energies, 9 charge radii, and 3 neutron skin thicknesses.

The functional DD-MEδ [12] differs from the earlier DD-ME functionals in the fitting strategy. It tries to use only a minimal number of free parameters adjusted to the data in finite nuclei and to use *ab initio* calculations to determine the density dependence of the meson-nucleon vertices. Relativistic *ab initio* calculations [20,21] show clearly that the isovector scalar self-energy, i.e., the field of the δ meson, is not negligible. Therefore, the functional DD-MEδ differs also from the other functionals by including the δ meson, which leads to a different effective Dirac mass for protons and neutrons:

$$m^*_{n,p} = m + g_\sigma\sigma \pm g_\delta\delta. \tag{7}$$

As a consequence, the splittings of the spin-orbit doublets with large orbital angular momentum l are slightly different in the models with and without δ meson. However, this effect is too small to be seen in present experiments [12]. All the other effects of the δ meson on experimental isovector properties of nuclear structure at densities below and slightly above saturation can be completely absorbed by a renormalization of the ρ-meson-nucleon vertex [12]. Therefore, successful phenomenological CEDF's do not need to include the δ meson. However, the effects of the δ meson are important for a proper description of the nuclear equation of state (EoS) at higher densities (see Ref. [12] and references given there), which play a role in heavy-ion reactions and in astrophysics.

In the earlier parameter sets DD-ME1 [39] and DD-ME2 [23] all eight independent parameters were adjusted to experimental data in finite nuclei, whereas for DD-MEδ only the four independent parameters m_σ, $g_\sigma(\rho_{\rm sat})$, $g_\omega(\rho_{\rm sat})$, and $g_\rho(\rho_{\rm sat})$ have been adjusted to experimental data in finite nuclei. This data set includes 161 binding energies and 86 charge radii of spherical nuclei. The parameter $g_\delta(\rho_{\rm sat})$ and the density dependence $f_i(x)$ have been fitted to parameter-free *ab initio* calculations of infinite nuclear matter of various densities, as, for instance, the EoSs for symmetric nuclear matter and pure neutron matter, and the difference of the effective Dirac masses $m^*_p - m^*_n$. Thus, the functional DD-MEδ is the most microscopically justified CEDF among those used in this investigation.

The Lagrangian for the DD-PC model [11,40] is given by

$$\begin{aligned}\mathcal{L} = {} & \bar\psi(i\gamma\cdot\partial - m)\psi - \tfrac{1}{4}F_{\mu\nu}F^{\mu\nu} - e\bar\psi\gamma\cdot A\psi \\ & - \tfrac{1}{2}\alpha_S(\rho)(\bar\psi\psi)(\bar\psi\psi) - \tfrac{1}{2}\alpha_V(\rho)(\bar\psi\gamma^\mu\psi)(\bar\psi\gamma_\mu\psi) \\ & - \tfrac{1}{2}\alpha_{TV}(\rho)(\bar\psi\vec\tau\gamma^\mu\psi)(\bar\psi\vec\tau\gamma_\mu\psi) - \tfrac{1}{2}\delta_S(\bar\psi\psi)\Box(\bar\psi\psi).\end{aligned} \tag{8}$$

It contains the free-nucleon part, the coupling of the proton to the electromagnetic field, and the point-coupling interaction terms. The derivative term with the D'Alembert operator $\Box$ accounts for the leading effects of finite-range interaction which are important in nuclei. In analogy with meson-exchange models, this model contains isoscalar-scalar (S),

TABLE II. The parameters of the DD-PC1 CEDF.

Parameter	DD-PC1
m	939
a_S	−10.046 16
b_S	−9.150 42
c_S	−6.427 29
d_S	1.372 35
a_V	5.919 46
b_V	8.863 70
d_V	0.658 35
b_{TV}	1.835 95
d_{TV}	0.640 25

isoscalar-vector (V), and isovector-vector (TV) interactions. The coupling constants $\alpha_i(\rho)$ are density dependent.

In the present work the Lagrangian (8) is represented by the parametrization DD-PC1 [11] given in Table II. The following ansatz is used for the functional form of the couplings,

$$\alpha_i(\rho) = a_i + (b_i + c_i x)e^{-d_i x}, \quad \text{for } i = S,V,TV, \qquad (9)$$

where $x = \rho/\rho_{\text{sat}}$ denotes the nucleon density in units of the saturation density of symmetric nuclear matter. In the isovector channel a pure exponential dependence is used, i.e., $a_{TV} = 0$ and $c_{TV} = 0$. The remaining set of ten constants, a_S, b_S, c_S, d_S, a_V, b_V, c_V, d_V, b_{TV}, and d_{TV}, which control the strength and density dependence of the interaction Lagrangian, was adjusted in a multistep parameter fit exclusively to the experimental masses of 64 axially deformed nuclei.

The fitting protocols used for the derivation of the various CEDF's differ in the amount and the type of experimental data. Figure 1 shows the nuclei which were used in the fits of the different CEDF's. NL3*, DD-ME2, and DD-MEδ CEDF were fitted to spherical nuclei, while DD-PC1 was fitted to deformed nuclei in the rare-earth and actinide regions. Only 12 spherical nuclei were used in the fitting protocols of NL3* and DD-ME2. On the contrary, the fits of other CEDF's rely on more extensive sets of experimental data (161 spherical nuclei in the DD-MEδ CEDF and 64 deformed nuclei in the DD-PC1 CEDF). In all these fitting protocols, the binding energies were used. In addition, the charge radii were employed in the fitting of NL3*, DD-ME2, and DE-MEδ. In contrast to nonrelativistic models, no single-particle information has been used in the fits. The number of independent parameters in the NL3*, DD-ME2, DD-MEδ, and DD-PC1 CEDF is 6, 8, 14, and 10, respectively. Note, however, that in the case of DD-MEδ, only the 4 parameters are fitted to the properties of finite nuclei and the additional 10 parameters are fitted to pseudodata obtained from *ab initio* calculations of nuclear matter.

III. SOLUTION OF THE RHB EQUATIONS

Pairing correlations play an important role in all open-shell nuclei. On the mean-field level they are taken into account by Bardeen-Cooper-Schrieffer (BCS) or Hartree-Fock-Bogoliubov (HFB) theory and in the relativistic case by relativistic Hartree-Bogoliubov (RHB) theory [41–43]. Therefore, DFT in nuclei always has to go beyond the simple

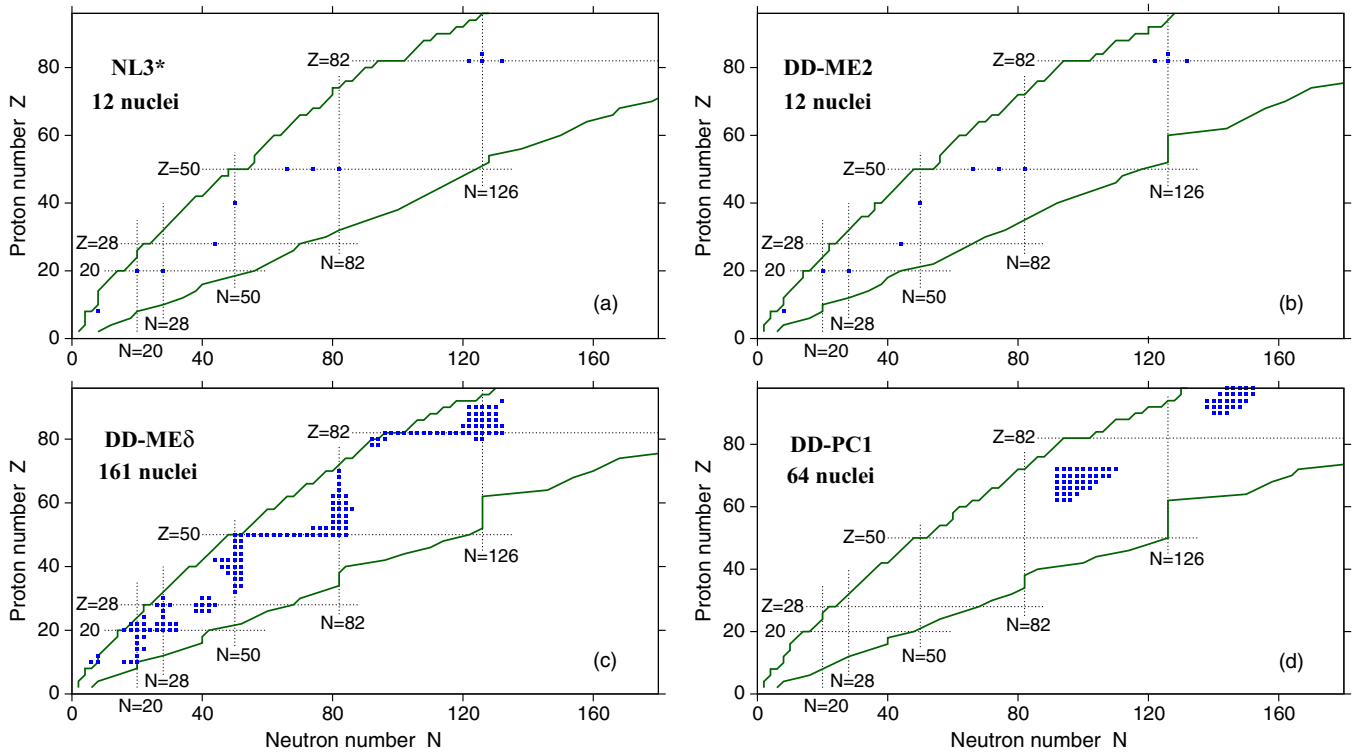

FIG. 1. (Color online) The nuclei (solid squares), shown in the (N,Z) plane, which were used in the fit of indicated CDFT parametrizations. Their total number is shown below the parametrization label. Magic shell closures are shown by dashed lines.

DFT used in most of the DFT applications in Coulombic systems, where the energy depends only on the normal single-particle density ρ. Nuclear energy density functionals depend on two densities, the normal density,

$$\rho_{n_1 n_2} = \langle \Phi | c^\dagger_{n_2} c_{n_1} | \Phi \rangle, \tag{10}$$

and the anomalous density,

$$\kappa_{n_1 n_2} = \langle \Phi | c_{n_2} c_{n_1} | \Phi \rangle, \tag{11}$$

usually called the pairing tensor. $|\Phi\rangle$ is the RHB wave function, a generalized Slater determinant [44] and, therefore, the density ρ as well as κ depend on the pairing correlations. In particular, the density matrix ρ is no longer a projector on the subspace of occupied states:

$$\rho^2 - \rho = \kappa\kappa^*. \tag{12}$$

In the relativistic form the nuclear energy functional is usually given by

$$E_{\rm RHB}[\rho,\kappa] = E_{\rm RMF}[\rho] + E_{\rm pair}[\kappa], \tag{13}$$

where $E_{\rm RMF}[\rho]$ has the same functional form as the CEDF's discussed in the last section, but it is now a functional of the density ρ in Eq. (10) depending on the RHB wave function $|\Phi\rangle$. The pairing energy[1] is given by

$$E_{\rm pair}[\kappa] = \frac{1}{4} \sum_{n_1 n_2, n_1' n_2'} \kappa^*_{n_1 n_2} \langle n_1 n_2 | V^{pp} | n_1' n_2' \rangle \kappa_{n_1' n_2'}. \tag{14}$$

The Dirac equation for fermion fields $\psi(\boldsymbol{r})$ is now replaced by the RHB equation. In the present paper, the RHB framework with finite range pairing and its separable limit are used for a systematic study of ground state properties of all even-even nuclei from the proton to neutron drip line. It has the proper coupling to the continuum at the neutron drip line and, therefore, it allows a correct description of weakly bound nuclei close to the neutron drip line. Even nuclear halo phenomena can be described by this method, if a proper basis is used, such as the coordinate space [45,46] or a Woods-Saxon basis [47].

The RHB equations for the fermions are given by [43]

$$\begin{pmatrix} \hat{h}_D - \lambda & \hat{\Delta} \\ -\hat{\Delta}^* & -\hat{h}^*_D + \lambda \end{pmatrix} \begin{pmatrix} U(\boldsymbol{r}) \\ V(\boldsymbol{r}) \end{pmatrix}_k = E_k \begin{pmatrix} U(\boldsymbol{r}) \\ V(\boldsymbol{r}) \end{pmatrix}_k, \tag{15}$$

Here $\hat{h}_D$ is the Dirac Hamiltonian for the nucleons with mass m, λ is the chemical potential defined by the constraints on the average particle number for protons and neutrons, $U_k(\boldsymbol{r})$ and $V_k(\boldsymbol{r})$ are quasiparticle Dirac spinors [41–43], and E_k denotes the quasiparticle energies. The Dirac Hamiltonian

$$\hat{h}_D = \boldsymbol{\alpha}(\boldsymbol{p} - \boldsymbol{V}) + V_0 + \beta(m + S) \tag{16}$$

contains an attractive scalar potential,

$$S(\boldsymbol{r}) = g_\sigma \sigma(\boldsymbol{r}), \tag{17}$$

a repulsive vector potential,

$$V_0(\boldsymbol{r}) = g_\omega \omega_0(\boldsymbol{r}) + g_\rho \tau_3 \rho_0(\boldsymbol{r}) + e A_0(\boldsymbol{r}), \tag{18}$$

and a magnetic potential,

$$\boldsymbol{V}(\boldsymbol{r}) = g_\omega \boldsymbol{\omega}(\boldsymbol{r}) + g_\rho \tau_3 \boldsymbol{\rho}(\boldsymbol{r}) + e\boldsymbol{A}(\boldsymbol{r}). \tag{19}$$

The last term breaks time-reversal symmetry and induces currents. Time-reversal symmetry is broken when the time-reversed orbitals are not occupied pairwise. This takes place in odd-mass nuclei [15]. In the Dirac equation, the spacelike components of the vector mesons $\boldsymbol{\omega}(\boldsymbol{r})$ and $\boldsymbol{\rho}(\boldsymbol{r})$ have the same structure as the spacelike component $\boldsymbol{A}(\boldsymbol{r})$ generated by the photons. Because $\boldsymbol{A}(\boldsymbol{r})$ is the vector potential of the magnetic field, by analogy the effect owing to presence of the vector field $\boldsymbol{V}(\boldsymbol{r})$ is called *nuclear magnetism* [14]. It affects the properties of odd-mass nuclei [15]. Thus, the spatial components of the vector mesons are properly taken into account for such nuclei. This is done only for the study of odd-even mass staggerings in Sec. IV as it has been successfully done earlier for the studies of single-particle [48,49] and pairing [50] properties of deformed nuclei. Nuclear magnetism, i.e., currents and time-odd mean fields, plays no role in the studies of even-even nuclei. The systematic investigations of such nuclei are performed within the axial RHB computer code outlined below. As the absolute majority of nuclei are known to be axially and reflection symmetric in their ground states, we consider only axial and parity-conserving intrinsic states and solve the RHB equations in an axially deformed harmonic oscillator basis [29,51].

We have developed a parallel version of the axial RHB computer code starting from a considerably modified version of the computer code DIZ [51]. This code is based on an expansion of the Dirac spinors and the meson fields in terms of harmonic oscillator wave functions with cylindrical symmetry. The calculations are performed by successive diagonalizations using the method of quadratic constraints [44]. The parallel version allows simultaneous calculations for a significant number of nuclei and deformation points in each nucleus. For each nucleus, we minimize

$$E_{\rm RHB} + \frac{C_{20}}{2}(\langle \hat{Q}_{20} \rangle - q_{20})^2, \tag{20}$$

where $E_{\rm RHB}$ in Eq. (13) is the total energy and $\langle \hat{Q}_{20} \rangle$ denotes the expectation value of the mass quadrupole operator,

$$\hat{Q}_{20} = 2z^2 - x^2 - y^2, \tag{21}$$

where q_{20} is the constrained value of the multipole moment and C_{20} the corresponding stiffness constant [44]. To provide the convergence to the exact value of the desired multipole moment we use the method suggested in Ref. [52]. Here the quantity q_{20} is replaced with the parameter $q^{\rm eff}_{20}$, which is automatically modified during the iteration in such a way that we obtain $\langle \hat{Q}_{20} \rangle = q_{20}$ for the converged solution. This method works well in our constrained calculations.

For each nucleus the potential energy curve is calculated in a large deformation range from $\beta_2 = -0.4$ up to $\beta_2 = 1.0$ by means of the constraint on the quadrupole moment q_{20}. The lowest in energy minimum is defined from the potential energy curve. Then, unconstrained calculations are performed in this minimum and the correct ground state configuration and its energy are determined. This procedure is especially important for the cases of shape coexistence.

[1]The details for the treatment of pairing are presented in Sec. IV

The truncation of the basis is performed in such a way that all states belonging to the major shells up to $N_F = 20$ fermionic shells for the Dirac spinors and up to $N_B = 20$ bosonic shells for the meson fields are taken into account. In constrained calculations, the deformation of the basis is selected in such a way that it corresponds to the desired deformation of the converged solution. The Coulomb field is determined by integrating over the Green's function [51]. The comparison with the results obtained with $N_F = 26$ and $N_B = 26$ clearly shows that this truncation scheme provides sufficient numerical accuracy for the description of weakly bound nuclei in the vicinity of the neutron drip line and of superheavy nuclei. This is even more true for the nuclei in the vicinity of β-stability line and for the nuclei with masses $A \leqslant 260$ away from neutron drip line.

It has been found in axial reflection-symmetric calculations for superheavy nuclei with $Z \geqslant 106$ that the superdeformed minimum is frequently lower in energy than the normal deformed one [53,54]. As long as triaxial [54] and octupole [53,54] deformations are not included, this minimum is stabilized by the presence of an outer fission barrier. Including such deformations, however, it often turns out that this minimum becomes a saddle point, unstable against fission [53,54]. Because these deformations are not included in the present calculations, we restrict our consideration to nuclei with $Z \leqslant 104$. The investigation of ground state properties of superheavy $Z \geqslant 106$ nuclei is inevitably connected with the studies of fission barriers; such investigations are currently in progress and their results will be reported in a forthcoming paper [55]. Of course, in the nuclear chart there exist also a small number of nuclei with stable octupole or triaxial deformations not considered here which we have to leave for future investigations.

IV. THE EFFECTIVE PAIRING INTERACTION

The pair field $\hat{\Delta}$ in RHB theory is given by

$$\hat{\Delta} \equiv \Delta_{n_1 n_2} = \frac{1}{2} \sum_{n_1' n_2'} \langle n_1 n_2 | V^{pp} | n_1' n_2' \rangle \kappa_{n_1' n_2'}. \tag{22}$$

It contains the pairing tensor κ of Eq. (11),

$$\kappa = V^* U^T, \tag{23}$$

and the effective interaction V^{pp} in the particle-particle channel.

In the literature on nuclear DFT several types of effective pairing forces V^{pp} have been used. The most simple force is the seniority force of Kerman [56] with constant pairing matrix elements G. For problems with time-reversal symmetry the corresponding pairing matrix Δ in Eq. (22) is proportional to unity for this force and RHB theory is equivalent to RMF + BCS. This force is widely used, but it has many limitations, e.g., correlations in pairs with higher angular momentum are neglected, the scattering between pairs with different shells is not constant in realistic forces, the coupling to the continuum is not properly taken into account and the predictive power is limited. Nonetheless, this method is used in the constant gap approximation in most of the large-scale adjustments of CEDF's, in particular, also for DD-ME2 [23] and DD-PC1 [11]. For each nucleus in the fit, the gap parameter is determined directly from odd-even mass differences of neighboring nuclei. In this case the occupation numbers v_k^2 in the neighborhood of the Fermi surface, which depend crucially on the gap parameter, have rather reasonable values and in this way all quantities depending only on the v_k^2's are not influenced further either by the value of G or by the pairing window. Of course, the pairing energy (14) depends on the constant G and on the pairing window. The actual value of G producing this experimental gap parameter is determined after the self-consistent solution of the BCS equations and depends on the nucleus under consideration and on the pairing window. However, for a reasonable pairing window the total change in binding energy caused by pairing, which is the difference between the gain in binding owing to the pairing energy (14) and the loss in binding owing to the reoccupation of the single-particle levels, is rather small. Therefore, there is a clear separation of scales between the total binding energy, which is of the order of 1000 MeV and more for heavy nuclei, and the additional binding of a few MeV caused by pairing. For this reason the conventional procedure to adjust the parameters of the Lagrangian in the constant gap approximation by RMF + BCS calculations and to use for all further RHB calculations a more realistic pairing force is very successful. In this way all the problems of the monopole pairing force are avoided.

In the present investigation two types of realistic effective pairing interaction have been used. Both of them have finite range and, therefore, provide an automatic cutoff of high-momentum components. These are as follows.

(i) The Brink-Booker part of phenomenological non-relativistic D1S Gogny-type finite-range interaction,

$$V^{pp}(1,2) = f \sum_{i=1,2} e^{-[(\boldsymbol{r}_1 - \boldsymbol{r}_2)/\mu_i]^2} (W_i + B_i P^\sigma - H_i P^\tau - M_i P^\sigma P^\tau). \tag{24}$$

The motivation for such an approach to the description of pairing is given in Refs. [43,57]. In Eq. (24), μ_i, W_i, B_i, H_i, and M_i ($i = 1,2$) are the parameters of the force and P^σ and P^τ are the exchange operators for the spin and isospin variables. The D1S parametrization of the Gogny force [58,59] is used here. Note that a scaling factor f is introduced in Eq. (24). Its role is discussed below.

(ii) A separable pairing interaction of finite range introduced by Tian *et al.* [60]. Its matrix elements in r space have the form

$$V(\boldsymbol{r}_1, \boldsymbol{r}_2, \boldsymbol{r}_1', \boldsymbol{r}_2') = -f\, G \delta(\boldsymbol{R} - \boldsymbol{R}') \times P(r) P(r') \tfrac{1}{2}(1 - P^\sigma), \tag{25}$$

with $\boldsymbol{R} = (\boldsymbol{r}_1 + \boldsymbol{r}_2)/2$ and $\boldsymbol{r} = \boldsymbol{r}_1 - \boldsymbol{r}_2$ being the center of mass and relative coordinates. The form factor $P(r)$ is of Gaussian shape,

$$P(r) = \frac{1}{(4\pi a^2)^{3/2}} e^{-r^2/4a^2}. \tag{26}$$

The parameters of this interaction have been derived by a mapping of the $^1S_0$ pairing gap of infinite nuclear matter to that of the Gogny force D1S. The resulting parameters are $G = 738$ fm^3 and $a = 0.636$ fm [60]. The scaling factor f is the same as in Eq. (24).

Both in theory and in experiment the strength of pairing correlations is usually accessed via the three-point indicator [61],

$$\Delta^{(3)}(N) = \frac{\pi_N}{2}\left[B(N-1) + B(N+1) - 2B(N)\right], \quad (27)$$

which quantifies the odd-even staggering (OES) of binding energies. Here $\pi_N = (-1)^N$ is the number parity and $B(N)$ is the (negative) binding energy of a system with N particles. In Eq. (27), the number of protons Z is fixed, and N denotes the number of neutrons; i.e., this indicator gives the neutron OES. The factor depending on the number parity π_N is chosen so that the OES centered on even and odd neutron number N will both be positive. An analogous proton OES indicator $\Delta^{(3)}(Z)$ is obtained by fixing the neutron number N and replacing N with Z in Eq. (27).

As discussed in Ref. [50], in many applications of RHB theory with the pairing force D1S the same scaling factor f has been used across the nuclear chart. However, it was found a decade ago that a proper description of rotational properties in actinides [48] requires weaker pairing as compared with the rare-earth region [43,62]. Subsequent systematic studies of pairing (via the three-point indicator $\Delta^{(3)}$) and rotational properties of actinides confirmed this observation in Refs. [50,63]. The investigation of odd-even mass staggerings in spherical nuclei in Ref. [64] also confirms the need for a scaling factor f which depends on the region in the nuclear chart. The studies of Refs. [48,50,64] show also a weak dependence of the scaling factor f on the CDFT parametrization. We therefore introduce in Eqs. (24) and (25) a scaling factor f for a fine tuning of the effective pairing force.

The scaling factor f used in the present investigation has been selected based on the results of a comparison between experimental moments of inertia and those obtained in cranked RHB calculations with the CEDF NL3*. As verified in the actinides in Ref. [50], the strengths of pairing defined by means of the moments of inertia and by the three-point indicators $\Delta^{(3)}$ strongly correlate in deformed nuclei. Following the results obtained in Ref. [50], the scaling factor has been fixed at $f = 1.0$ in the $Z \geqslant 88$ actinides and superheavy nuclei. The analysis of the moments of inertia in the rare-earth region [65] leads to a scaling factor of $f = 1.075$ for the $56 \leqslant Z \leqslant 76$ rare-earth nuclei. For $Z \leqslant 44$ nuclei, the scaling factor was fixed at $f = 1.12$ [65]. The scaling factor gradually changes with Z between these regions. Because the strength parameter G of the separable force has been determined in Ref. [60] by a direct mapping to the Gogny force D1S, the same scaling factors are also used in the following RHB calculations with separable pairing.

Figures 2 and 3 compare calculated (open red circles) and experimental (solid black circles) three-point indicators $\Delta^{(3)}$ for different chains of spherical nuclei. In both theory and experiment, these quantities have been obtained from binding energies. The calculations have been performed within the RHB formalism of Refs. [43,48], which allows a fully self-consistent treatment of even-even and odd-mass nuclei. Blocking and time-odd mean fields have been taken into account in the case of odd-mass nuclei. The Gogny force D1S of Eq. (24) with the scaling factors f has been used in these calculations. As shown in Ref. [15] the impact of the time-odd mean fields on the $\Delta^{(3)}$ indicators cannot be ignored. Large peaks appear in the experimental $\Delta^{(3)}$ indicators at shell closures. This is connected with the fact that pairing correlations disappear in these cases and the peaks are not produced by pairing, but by the increasing shell gap for closed-shell configurations. Therefore, they are not relevant for the present discussions.

One can see that, on average, the RHB calculations reproduce the experimental data and the magnitude of the observed staggering in $\Delta^{(3)}$ rather well. However, in some nuclei the calculations somewhat overestimate experimental $\Delta^{(3)}$ indicators. There are two possible reasons for that. First, particle-vibration coupling in odd-mass nuclei is neglected in these calculations. Extra correlations induced by this coupling increases the binding energy in odd-mass nuclei. According to Eq. (27), this will lead to smaller $\Delta^{(3)}$ values. Thus, the agreement with experiments could improve if we would take into account the additional correlations owing to particle-vibrational coupling in odd-mass nuclei. The analysis of Ref. [66] suggests that this effect is non-negligible and that it can reach up to 300 keV. In addition, we have to keep in mind that the effects of particle-vibration coupling are state-dependent [67]. The second reason for the deviations between theory and experiment in Fig. 2 has to do with the deficiencies in the underlying single-particle structure produced by the CEDF NL3* [49,67].

Figure 2 also shows that the accuracy of the description of the $\Delta^{(3)}$ indicators depends on the structure of underlying single-particle states. For example, reasonable agreement between theory and experiment is obtained in the Ni isotopes between the $N = 28$ shell and the $N = 40$ subshell closures where the active neutrons occupy the spherical $2p_{3/2}$, $1f_{5/2}$, and $2p_{1/2}$ orbits. However, the calculations systematically overestimate the experiment between the $N = 40$ subshell and the $N = 50$ shell closure where the active neutron occupies the $1g_{9/2}$ orbit. A similar situation and a reduced accuracy in the description of experimental data can be seen in the chain of Sn [Fig. 2(c)] and Pb [Fig. 2(d)] isotopes when crossing the $N = 82$ and $N = 126$ shell closures. We do not have a clear explanation for these features but two factors may contribute: first, the state dependence of particle-vibration coupling mentioned above, and second, a deficiency of the Gogny force D1S to reproduce a possible state dependence of pairing correlations.

There are clearly some differences in the approaches based on fixing the pairing strength to the data in deformed and in spherical nuclei. This is also seen in the Skyrme EDF [68], where, similar to our case, the pairing strength adjusted to rotational structures leads to too high $\Delta^{(3)}$ indicators in spherical nuclei. As illustrated in Ref. [50], deformed nuclei offer the opportunity to fix the strength of pairing to two independent physical observables, the rotational moments of inertia and the $\Delta^{(3)}$ indicators. The accuracy of the description of the latter quantity

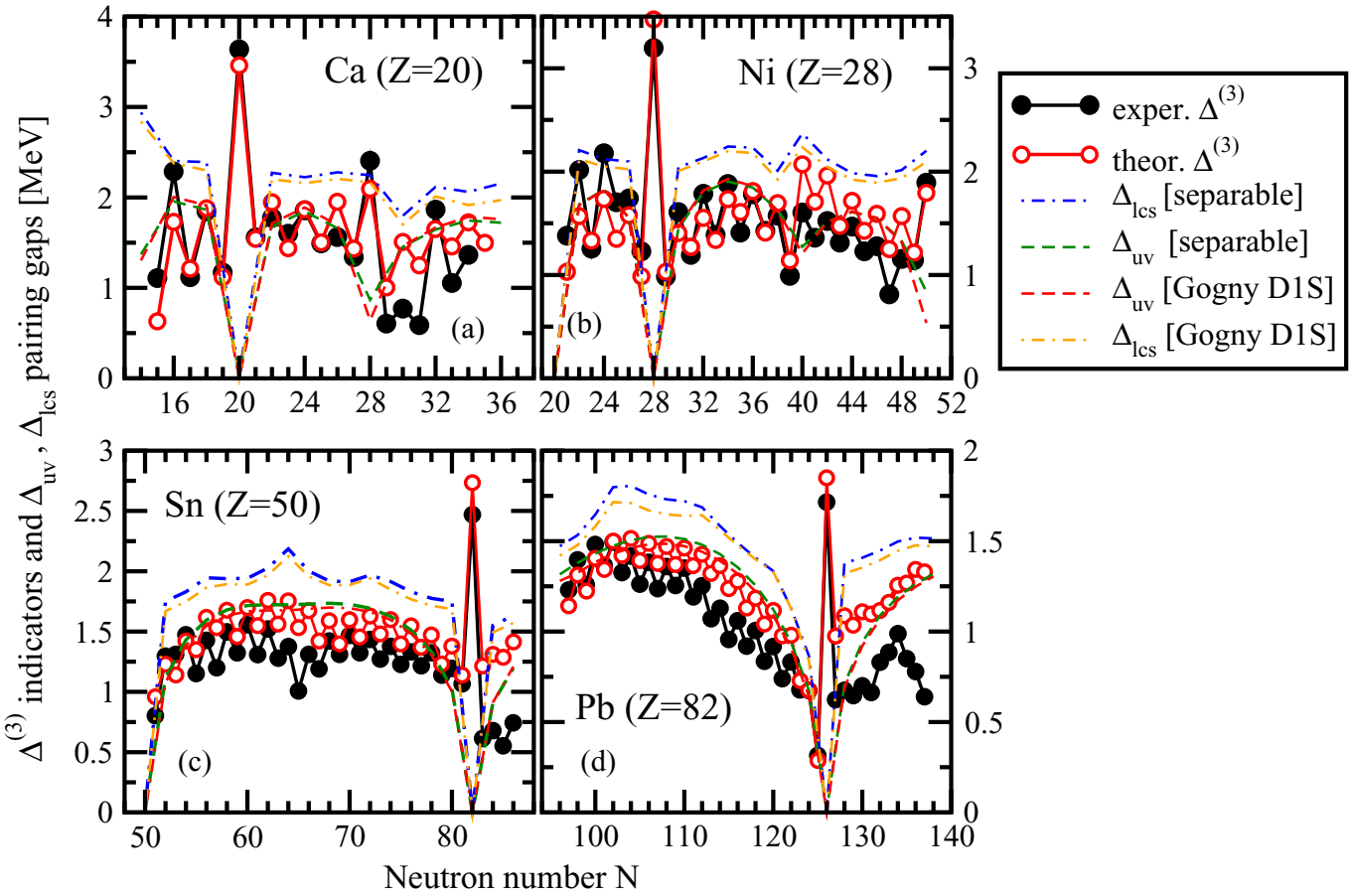

FIG. 2. (Color online) Experimental and calculated neutron three-point indicators $\Delta^{(3)}(N)$ and calculated pairing gaps Δ_{uv} and Δ_{lcs} as functions of the neutron number N. Theoretical $\Delta^{(3)}(N)$ indicators shown by open red circles are derived from calculated binding energies of odd- and even-even nuclei; they are obtained in RHB calculations with the CEDF NL3* and the Gogny force D1S of Eq. (24) in the pairing channel. The calculated pairing gaps Δ_{uv} and Δ_{lcs} are shown by lines. They are calculated in even-even nuclei with the Gogny force D1S (labeled as "Gogny D1S") and its separable approximation in Eq. (25) (labeled as "separable" in the figure).

in deformed nuclei depends on the correctness of the reproduction of the ground state configuration in the odd-mass nuclei and the impact of particle-vibration coupling (see Sec. III E of Ref. [50]). However, these factors have less influence on the calculated moments of inertia. Particle-vibration coupling is expected to be more pronounced in spherical nuclei as compared with deformed ones (see discussion in Sec. VI B of Ref. [48]). Thus, we believe that the experimental data in deformed nuclei allows a better and more reliable estimate of pairing strength as compared with the one in spherical nuclei.

However, it is too time consuming to perform the analysis presented in Refs. [50,65] for the remaining three functionals. Thus, we looked on alternative indicators for the strength of the effective pairing force. It is well known that the connection between the $\Delta^{(3)}$ (or $\Delta^{(5)}$) indicators and theoretical pairing gaps is not straightforward. Thus, several expressions for pairing gaps aimed at circumventing this problem have been proposed. On the one hand, they have the advantage of being calculated in even-even nuclei, thus avoiding the complicated problem of calculating the blocked states in odd-mass nuclei (see Refs. [49,50]). However, their validity for the comparison with experimental $\Delta^{(3)}$ indicators is not clear.

In the literature the following definitions for the average pairing gap have been used.

(i) The pairing gap

$$\Delta_{vv} = \frac{\sum_k v_k^2 \Delta_k}{\sum_k v_k^2} \tag{28}$$

has been introduced in Ref. [69]. The sum runs over the states k in the *canonical* basis (for details, see Ref. [44]). v_k^2 are the corresponding occupation probabilities and Δ_k is the diagonal matrix element of the pairing field in this basis.

(ii) The pairing gap

$$\Delta_{uv} = \frac{\sum_k u_k v_k \Delta_k}{\sum_k u_k v_k} \tag{29}$$

is related to the average of the state-dependent gaps over the pairing tensor.

(iii) The pairing gap Δ_{lcs} (lcs stands for lowest canonical state) [68] is defined by the smallest quasiparticle

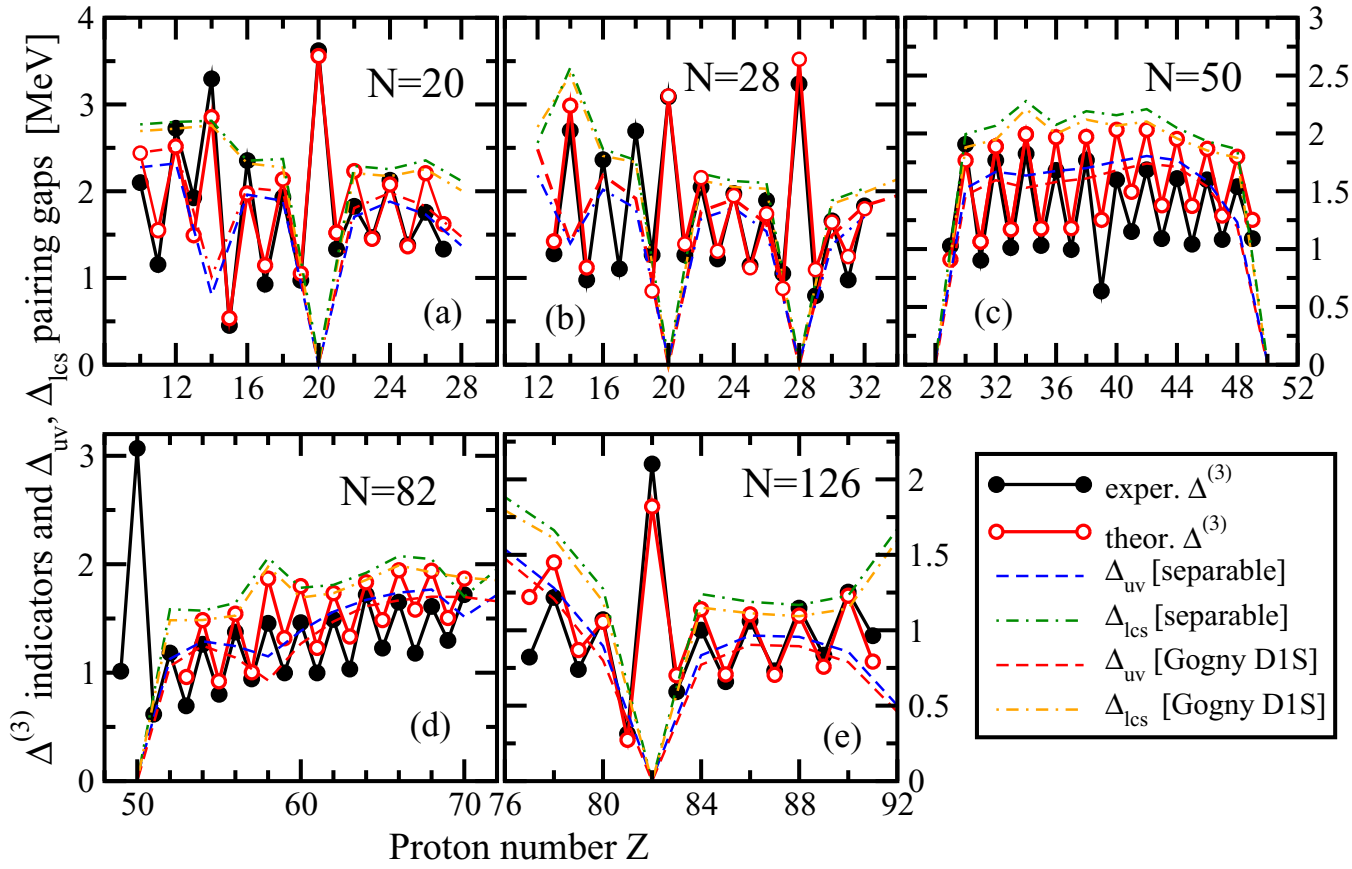

FIG. 3. (Color online) The same as Fig. 2 but for proton three-point indicators $\Delta^{(3)}(Z)$ and proton pairing gaps Δ_{uv} and Δ_{lcs} as a function of proton number Z. Note that it was not possible to get a convergence for a few odd-mass nuclei in the $N = 28$ and $N = 82$ isotone chains in the RHB calculations with Gogny D1S force in pairing channel. This leads to the absence of theoretical $\Delta^{(3)}$ values in some proton number range.

energy,

$$E_k = \sqrt{(\varepsilon_k - \lambda)^2 + \Delta_k^2}, \tag{30}$$

which is approximately equal to the gap Δ_k of the orbit closest to the Fermi surface. Here ε_k is the diagonal matrix element of the single-particle field $\hat{h}$ in the canonical basis.

All these definitions have advantages and disadvantages. Δ_{vv} averages over the occupation numbers v_k^2. For heavy nuclei with many fully occupied states most of the contributions are therefore determined by deeply bound states far from the Fermi surface, which have little to do with the pairing phenomenon and the scattering of Cooper pairs around the Fermi surface. Δ_{lcs} considers only the canonical orbit closest to the Fermi surface and, therefore, it is more connected to the pairing phenomenon. However, it has the disadvantage, that it depends on a specific orbit and that it is not really an average. Δ_{uv} finally averages over $u_k v_k$, a quantity which is concentrated around the Fermi surface However, because of the fact that $\kappa \sim \sum_k u_k v_k$ diverges for the seniority force and for zero-range forces, Δ_{uv} turns out to depend on the pairing window. This is, however, no problem for the finite-range pairing forces used in this investigation. In addition, in the majority of the cases the Δ_{vv} values are larger than the Δ_{lcs} ones, which, as follows from the discussion below, overestimate experimental data. Therefore, in the current paper, we consider only Δ_{uv} and Δ_{lcs}.

The calculated quantities are presented in Figs. 2 and 3 both for the Gogny force D1S in Eq. (24) and for its separable approximation (25). It is interesting to compare them with the five-point indicator $\Delta^{(5)}$ discussed in Refs. [68,70], which is a better measure of pairing correlations because it is less polluted by mean-field effects as compared with the $\Delta^{(3)}$ indicator. This quantity represents a smooth curve and the $\Delta^{(3)}$ indicator oscillates around it (see Fig. 2 of Ref. [68] for the graphical example of the relation between the $\Delta^{(3)}$ and the $\Delta^{(5)}$ indicators). It turns out that far from spherical shell closures, the Δ_{uv} values come close to the calculated $\Delta^{(5)}$ indicators. However, the Δ_{lcs} values always overestimate the $\Delta^{(5)}$ indicators. This result is contrary to the conclusions of Ref. [68], which concludes that the Δ_{lcs} value is a better measure of pairing correlations. The difference maybe attributable to the zero-range pairing forces in Ref. [68], while finite-range pairing forces are used in our paper.

Figures 2 and 3 also show that the pairing gaps Δ_{lcs} and Δ_{uv} calculated with the D1S Gogny force and its separable limit are very close to each other. Thus, all systematic calculations in this paper are performed with the separable form of the Gogny force D1S. This reduces the computational time considerably.

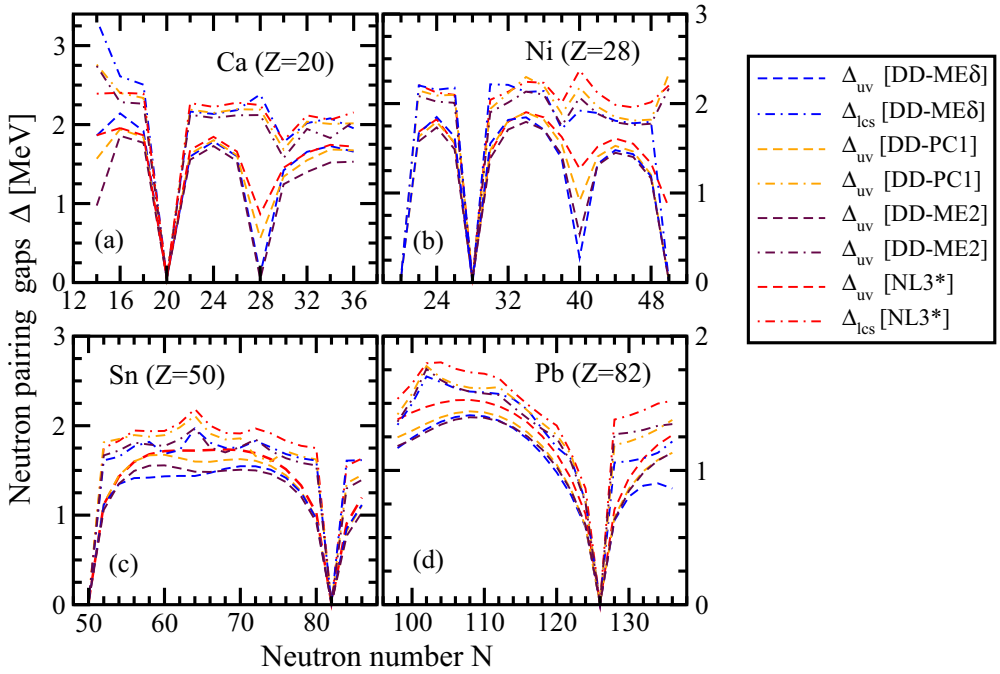

FIG. 4. (Color online) Calculated neutron pairing gaps Δ_{uv} and Δ_{lcs} as a function of the neutron number N for different isotonic chains. The results of RHB calculations with the separable pairing force (25) are presented for the indicated CEDF's.

Figures 4 and 5 compare the pairing gaps Δ_{lcs} and Δ_{uv} obtained in the calculations with different CEDF's. Apart from proton number $Z = 14$ in the $N = 20$ and the $N = 28$ isotope chains (see Fig. 5) and the proton subshell closure at $Z = 40$ in the Ni isotopes (see Fig. 4), the calculated gaps are similar for the different parameterizations. The spread in the calculated values indicates that scaling factors f used here are reasonable within the limits of a few percent. For example, the change of scaling factor f by 4% in ^{182}Pb leads to a change of the pairing gaps Δ_{lcs} and Δ_{uv} by ∼0.14 MeV. The weak dependence of the scaling factor f on the CEDF has already been seen in the studies of pairing and rotational properties in the actinides [48,50]. Thus, the same scaling factor f as defined above for the CEDF NL3* is used in the calculations with DD-PC1,

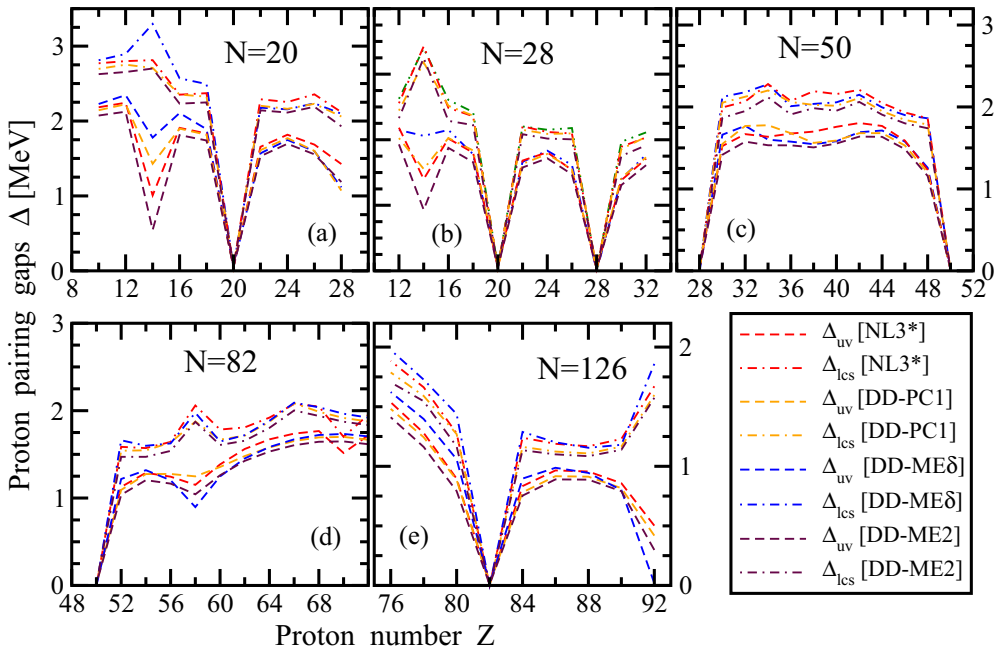

FIG. 5. (Color online) The same as Fig. 4 but for calculated proton pairing gaps Δ_{uv} and Δ_{lcs} as a function of the proton number Z for different isotopic chains.

TABLE III. The rms deviations $\Delta E_{\rm rms}$, $\Delta(S_{2n})_{\rm rms}$ [$\Delta(S_{2p})_{\rm rms}$] between calculated and experimental binding energies E and two-neutron (-proton) separation energies S_{2n} (S_{2p}). They are given in MeV for the indicated CDFT parametrizations with respect to "measured" and "measured + estimated" sets of experimental masses.

EDF	Measured	Measured + estimated		
	$\Delta E_{\rm rms}$	$\Delta E_{\rm rms}$	$\Delta(S_{2n})_{\rm rms}$	$\Delta(S_{2p})_{\rm rms}$
NL3*	2.96	3.00	1.23	1.29
DD-ME2	2.39	2.45	1.05	0.95
DD-MEδ	2.29	2.40	1.09	1.09
DD-PC1	2.01	2.15	1.16	1.03

DD-ME2, and DD-MEδ. Considering the global character of this study, this is a reasonable choice. Definitely there are nuclei in which the choice of the scaling factor f is not optimal. However, the change of scaling factor by 1% changes the binding energy only by approximately 100 keV. The impact on physical observables such as two-particle separation energies and the positions of two-proton and two-neutron drip lines is even smaller because they are sensitive to the differences in the binding energies. Changes of scaling factor by a few percent will only marginally affect the deformations, radii, and neutron skin thicknesses.

V. BINDING ENERGIES

In Table III we list the rms deviations $\Delta E_{\rm rms}$ between theoretical and experimental binding energies for the global RHB calculations with the different CEDF's investigated in this paper. The masses given in the AME2012 mass evaluation [71] can be separated into two groups: One represents nuclei with masses defined only from experimental data, the other contains nuclei with masses depending in addition on either interpolation or extrapolation procedures. For simplicity, we call the masses of the nuclei in the first and second groups as measured and estimated. There are 640 measured and 195 estimated masses of even-even nuclei in the AME2012 mass evaluation. One can see in Table III that the extension to include also estimated masses leads only to a slight decrease of the accuracy in the description of experimental data.

To our knowledge, for relativistic density functionals, reliable[2] global comparisons of experimental and theoretical masses have been performed so far only for the parametrizations NL3 [33], FSUGold [77], BSR4 [78], and TM1 [36] in the RMF + BCS approach using the constant gap approximation in Ref. [76] and for PC-PK1 [79] in the RMF + BCS approach with density-dependent pairing in Ref. [80]. Apart of BSR4 and PC-PK1 these CEDF's were fitted more than 10 years ago. The rms errors for the masses found for these CEDF's are 3.8 MeV for NL3, 6.5 MeV for FSUGold, 2.6 MeV for BSR4, 5.9 MeV for TM1, and 2.6 MeV for PC-PK1 (at the mean-field level).

One can see that the CEDF's NL3*, DD-ME2, DD-MEδ, and DD-PC1 investigated in the present paper provide an improved description of masses across the nuclear chart. The rms deviations for the binding energies presented in Table III are more statistically significant than those of Refs. [76] and [80] because they are defined for 835 even-even nuclei. On the contrary, rms deviations for binding energies for the NL3, FSUGold, BSR4, and TM1 CEDF's are defined only for 513 (575 for PC-PK1) even-even nuclei in Refs. [76] and [80]. The extension of the experimental database to 835 nuclei may lead to further deterioration of the rms deviations for these CEDF's.

In Fig. 7, the errors in binding energies are summarized for all experimentally known even-even nuclei. This figure is prepared in the same style as Fig. 3 of Ref. [76]. This makes it possible to compare the gross trends for the binding energy errors of the current and previous generations of the CEDF's. In particular, old CEDF's show in all cases a growing deviation from the zero line with increasing mass number (Fig. 3 in Ref. [76]). These deviations are especially pronounced for FSUGold and TM1, for which they reach 15 MeV for the highest measured masses. The deviations are smaller for the NL3 CEDF, for which they reach 10 MeV for the highest measured masses, and quite moderate for the BSR4 parametrization. On the contrary, no such problems exist in the current generation of the CEDF's. The accuracy of the description of the masses of heavy nuclei is comparable with or even better (as in the case of DD-PC1) than that of medium-mass and light nuclei (Fig. 6). The large deviation peaks seen in Fig. 6 are located in the vicinity of the doubly magic shell closures. For such nuclei, medium polarization effects associated with surface and pairing vibrations have a substantial effect on the binding energies [81].

Previous estimates of the rms deviations for binding energies with these CEDF's have been obtained only with restricted sets of experimental data. For example, the RHB(NL3*) results were compared with experiment only for approximately 180 even-even nuclei in Ref. [24]. However, no rms deviations for binding energies were presented for this set. An rms deviation of 2.4 MeV has been obtained in the analysis of 161 nuclei in the RMF + BCS calculations with DD-MEδ using monopole pairing [12]. Note, however, that the binding energies of these nuclei were used in the fit of DD-MEδ. Ninety-three deformed nuclei calculated in the RMF + BCS approach with DD-PC1 CEDF were compared with experiment in Ref. [11]. The binding energies of the most of these nuclei deviate from experiment by less than 1 MeV, which is not surprising considering that 64 of these nuclei were used in the fit of the corresponding CEDF. However, much larger deviations have been reported for this CEDF in spherical nuclei [11]. Note that,

[2]The masses were globally studied earlier in the RMF [72] or RMF + BCS [73,74] formalisms. However, the pairing correlations have been completely ignored in the studies of Ref. [72]. The treatment of pairing via the BCS approximation in Refs. [73,74] has to be taken with care in the region of the drip line because this approximation does not take into account the continuum properly and leads to the formation of a neutron gas [75] in nuclei near neutron drip line. In addition, these calculations use at most 14 fermionic shells for the harmonic oscillator basis, which according to our study and the one of Ref. [76] is not sufficient for a correct description of binding energies of actinides and superheavy nuclei and the nuclei in the vicinity of neutron drip line.

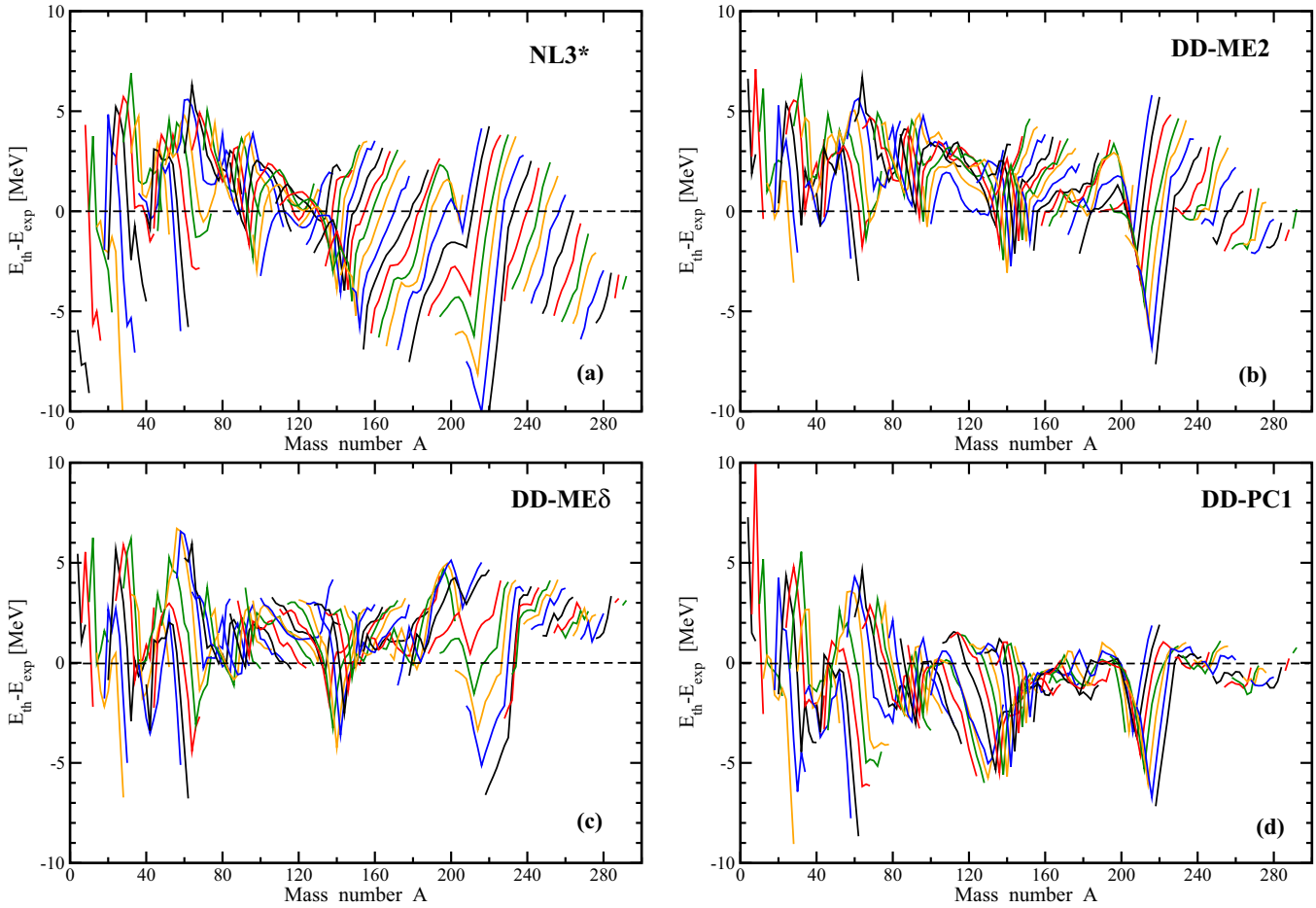

FIG. 6. (Color online) The difference between theoretical and experimental masses of 835 even-even nuclei investigated in RHB calculations with indicated CEDF's. If $E_{\rm th} - E_{\rm exp} < 0$, the nucleus is more bound in the calculations than in experiment.

so far, DD-PC1 is the only CEDF exclusively fitted to deformed nuclei. Theoretical binding energies of approximately 200 nuclei calculated in the RHB framework with DD-ME2 CEDF and the Gogny D1S interaction in the pairing channel show rms deviation of less than 0.90 MeV from experiment [23].

Comparing these rms deviations with the ones presented in Table III one can see that the increase of the size of experimental data set leads to a deterioration of the average description of the binding energies. This clearly suggests that the experimental data sets used in the fits of the CEDF's (see Sec. II for details) are not sufficiently large to provide an optimal localization of the model parameters in the parameter space and reliable extrapolation properties of the CEDF's with respect to binding energies. To our knowledge, so far, no attempt to create a "mass table" quality CEDF based on a fit to the full set of available experimental masses has been undertaken in CDFT. This is contrary to nonrelativistic models where mass tables based on an extensive use of experimental data were generated in the macroscopic + microscopic model [82], the Skyrme [83], and the Gogny [84] DFT. We have to keep in mind, however, that the number of free parameters in such fits to thousands of experimental masses is considerably larger than that used in the CEDF's investigated in this paper. In particular, many of these fits include more or less phenomenological terms for the Wigner energy [85,86] in close to $N \approx Z$ nuclei and for the rotational corrections in deformed nuclei.

One should also recognize the limitations of the description of masses at the mean-field level. This is clearly visible in Fig. 7, where the relative errors are plotted as a function of mass number A. One can see that these errors are especially pronounced in light $A \leqslant 80$ nuclei for which the configuration mixing effects (which go beyond mean field) are important [87–89]. In very light nuclei the clusterization effects can also be important [90] and for the nuclei in the $N = Z$ region the Wigner term [85,86]. Such effects are not taken into account in these density functionals. For the heavier $A \geqslant 80$ nuclei, the relative error in the description of masses stays safely within the $\pm 0.5\%$ error band. In this context, it is interesting to mention that a similar level of error ($\sim 0.3\%$) in the description of binding energies is achieved in the DFT local density approximation in condensed-matter physics [91].

In Fig. 8 we show the map of theoretical uncertainties $\Delta E(Z,N)$ defined in Eq. (1) for the description of binding energies. The comparison of this figure with Fig. 1 in Ref. [92] (which presents experimentally known nuclei in the nuclear chart) shows that the spreads in the predictions of binding energies stay within 5–6 MeV for the known nuclei. These

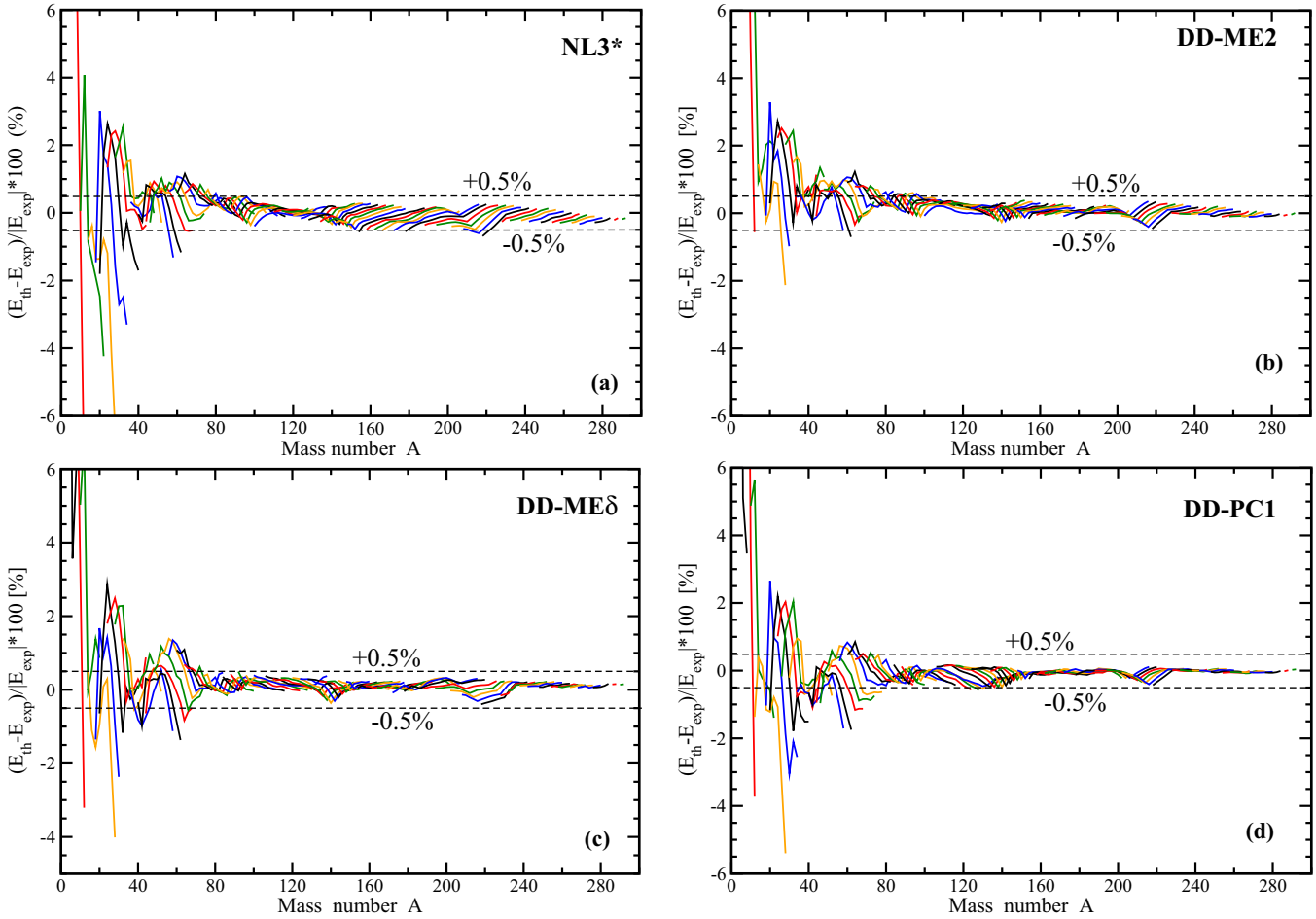

FIG. 7. (Color online) The relative accuracy of the description of experimental masses in our model calculations. The same set of data as in Fig. 6 is used. Dashed lines show the ±0.5% error band.

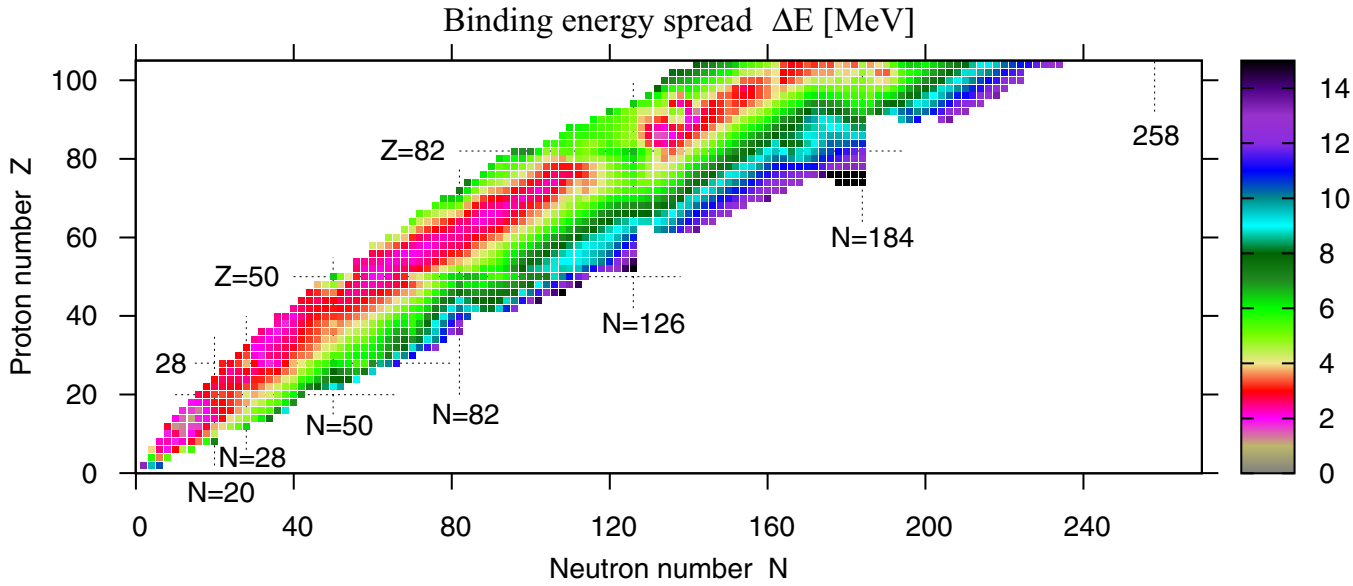

FIG. 8. (Color online) The binding energy spreads $\Delta E(Z,N)$ as a function of proton and neutron number. $\Delta E(Z,N) = |E_{\max}(Z,N) - E_{\min}(Z,N)|$, where $E_{\max}(Z,N)$ and $E_{\min}(Z,N)$ are the largest and the smallest binding energies for each (N,Z) nucleus obtained with the four CEDF's used in this investigation.

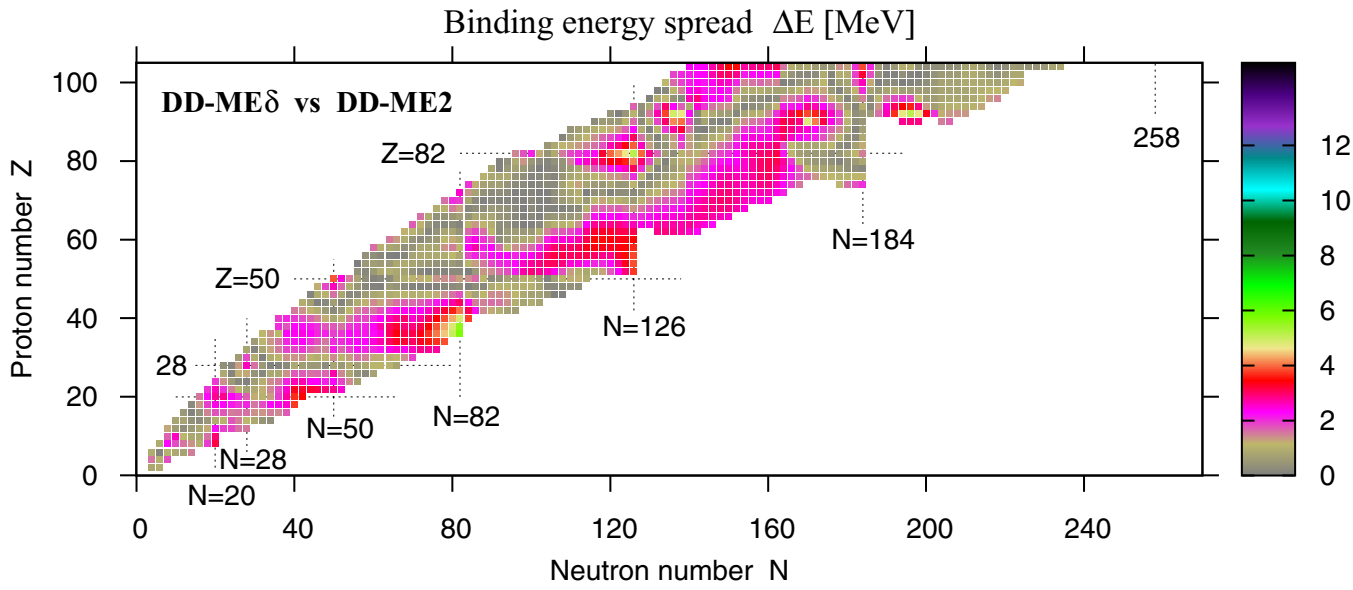

FIG. 9. (Color online) The same as Fig. 8, but only for DD-ME2 and DD-MEδ.

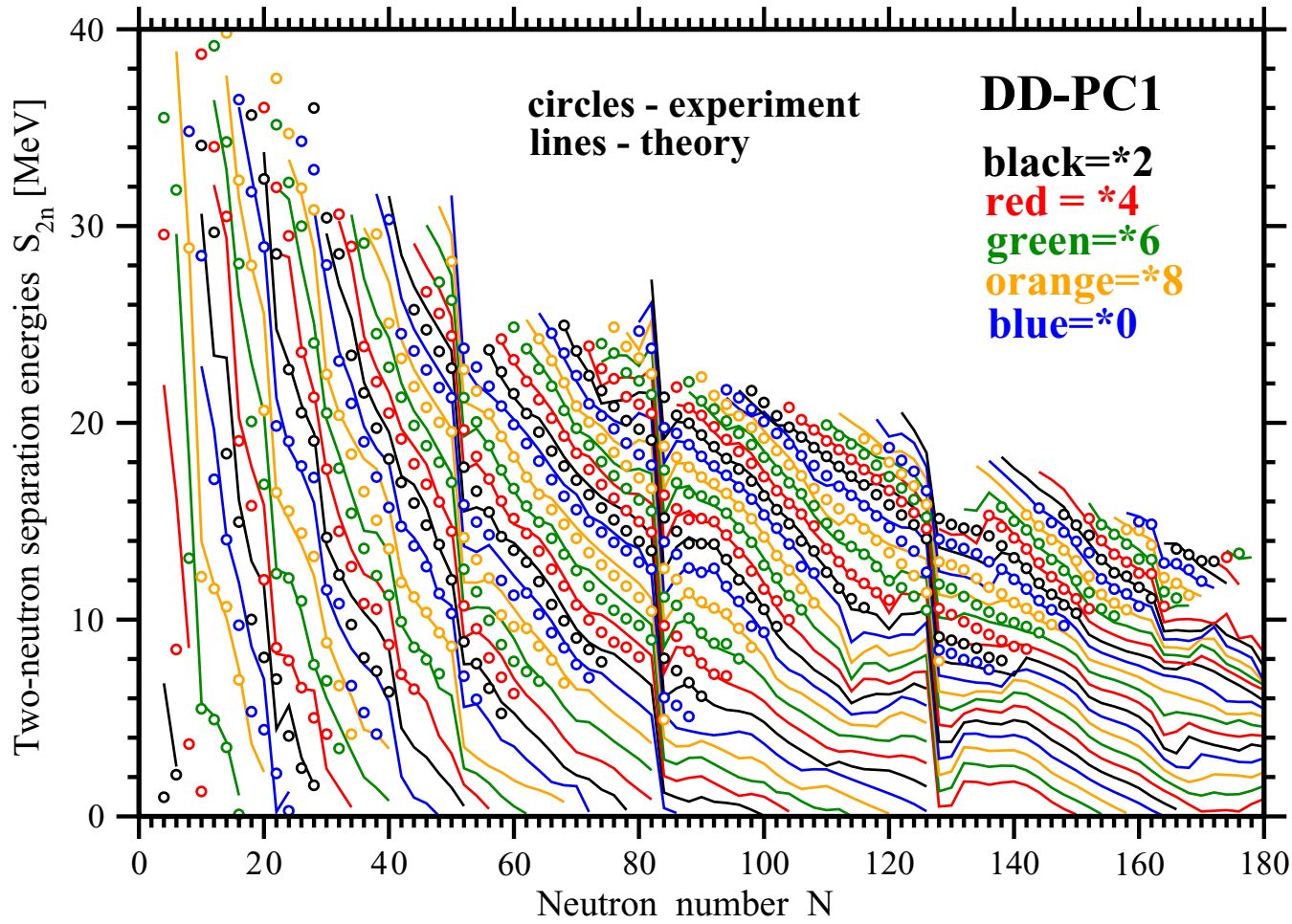

FIG. 10. (Color online) Two-neutron separation energies $S_{2n}(Z,N)$ given for different isotopic chains as a function of neutron number. To facilitate the comparison between theory and experiment, five different colors are used periodically as a function of neutron number. Black, red, green, orange, and blue colors are used for isotope chains with proton numbers ending with 2, 4, 6, 8, and 0, respectively.

spreads are even smaller (typically around 3 MeV) for the nuclei in the valley of β stability. However, the theoretical systematic uncertainties (1) for the masses increase drastically when approaching the neutron-drip line and in some nuclei they reach 15 MeV. This is a consequence of poorly defined isovector properties of many CEDF's. Comparing different pairs of CEDF's one can conclude that the smallest difference in the predictions of binding energies exists for the DD-ME2/DD-MEδ pair of CEDF's (Fig. 9). The next-smallest difference in terms of $\Delta E(Z,N)$ exists for the DD-PC1/NL3* pair of CEDF's.

VI. SEPARATION ENERGIES

Because our investigation is restricted to even-even nuclei, we consider two-neutron $S_{2n} = B(Z,N-2) - B(Z,N)$ and two-proton $S_{2p} = B(Z-2,N) - B(Z,N)$ separation energies. Here $B(Z,N)$ stands for the binding energy of a nucleus with Z protons and N neutrons. Two-neutron S_{2n} and two-proton S_{2p} separation energies are described with a typical accuracy of 1 MeV (Table III). The accuracy of the description of separation energies depends on the accuracy of the description of mass differences. As a result, it is not always the functional which provides the best description of masses that gives the best description of two-particle separation energies.

The accuracy of the description of two-neutron and two-proton separation energies is illustrated for different isotopic and isotonic chains on the example of RHB calculations with DD-PC1 in Figs. 10 and 11. Similar results were obtained also in the calculations with NL3*, DD-ME2, and DD-MEδ. One can see that two-proton separation energies are better described than two-neutron separation energies (see also Table III). In part, this is a consequence of the behavior of the calculated S_{2n} curves in the vicinity of spherical shell gaps. The experimental S_{2n} curves are smooth (frequently almost straight) as a function of neutron number between shell gaps (Fig. 10). For a given isotope chain, the calculations rather well reproduce this behavior of experimental S_{2n} curves in the regions of a few neutrons away from shell closures. However, the situation is different in the vicinity of the $N = 82$ and 126 shell closures. Here the calculations overestimate (underestimate) experimental S_{2n} values for a few nuclei before (after) the shell closure in a number of isotopic chains with $Z \geqslant 40$.

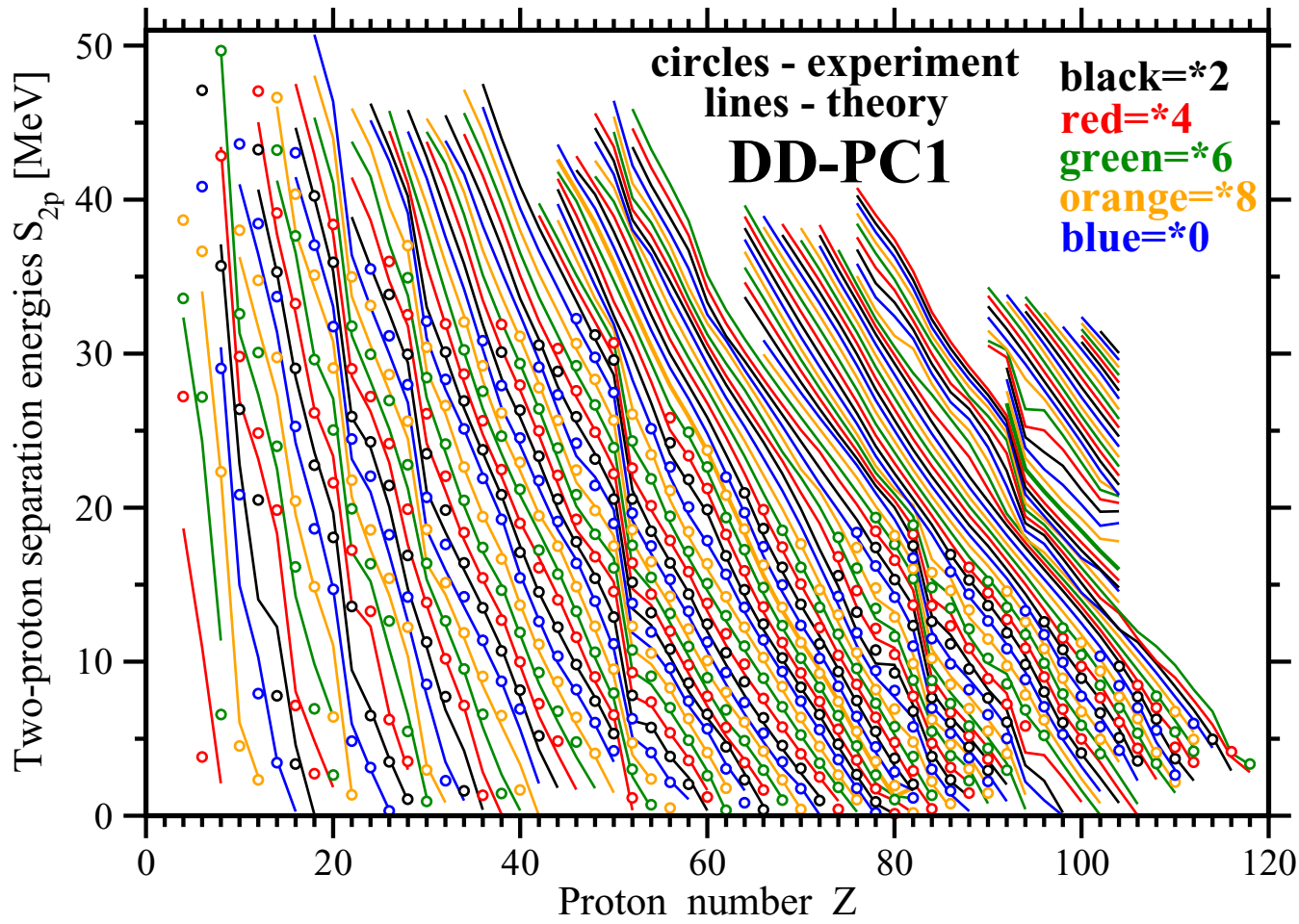

FIG. 11. (Color online) Two-proton separation energies $S_{2p}(Z,N)$ given for different isotonic chains as a function of proton number. To facilitate the comparison between theory and experiment, five different colors are used periodically as a function of proton number. Black, red, green, orange, and blue colors are used for isotonic chains with neutron numbers ending with 2, 4, 6, 8, and 0, respectively.

It is interesting that such problems do not exist for two-proton separation energies (Fig. 11). The origin of these problems is most likely related to the relative impact of proton and neutron shell closures. Figure 17 shows that the band of nuclei with spherical or near-spherical deformations (gray area in the figure) is wider around $N = 82$ and $N = 126$ as compared with the one around $Z = 50$ and $Z = 82$. Thus, the transition from spherical shapes to well-deformed shapes (where the mean-field description is justified) proceeds faster (in terms of particle number) for the proton subsystem than for the neutron subsystem. In contrast, the transitional shapes requiring a beyond-mean-field description are expected for a wider range of nuclei around the $N = 82$ and $N = 126$ shell closures. Neglecting these beyond-mean-field correlations is most likely the source for the above-mentioned discrepancies between experimental and calculated S_{2n} values in the vicinity of the $N = 82$ and $N = 126$ shell closures.

This analysis leads to a more critical look on the reappearance of two-neutron binding with increasing neutron number beyond the primary two-neutron drip line which exists in a number of DFT calculations [26,46,92]. This reappearance shows itself in the nuclear chart via the peninsulas emerging from the nuclear mainland. For example, as we see in Fig. 17, such peninsulas exist at ($Z = 62, N = 132$–146) and ($Z = 88, N = 194$–206) for DD-PC1, at ($Z = 74, N = 176$–184) and ($Z = 90, N = 194$–206) for DD-ME2, and at ($Z = 62, N = 132$–142), ($Z = 74, N = 178$–184), and ($Z = 90, N = 204$–206) for DD-MEδ, but they are absent in NL3*. The physical mechanism for their appearance was discussed in Ref. [92]. Its basic is the following: The two-neutron separation energy S_{2n} is slightly negative immediately after the large shell gap at the neutron number $N^{(1)}_{\rm drip}$ that defines the primary neutron drip line, but then with increasing neutron number it becomes slightly positive at a higher neutron number $N_{\rm penin}$ and remains like that for a range of neutron numbers up to $N^{(2)}_{\rm drip}$. A further increase of N beyond $N^{(2)}_{\rm drip}$ leads to two-neutron unbound nuclei. For example, these features are visible in Fig. 3 of Ref. [92]. However, the present analysis clearly shows that immediately after the large neutron shell closure CDFT calculations [and very likely also SDFT calculations because the shapes of calculated S_{2n} curves (see Fig. 8 in Ref. [93] and Fig. 2 in [26]) indicate the possibility of such a scenario] underestimate the experimental S_{2n} values. For some isotope chains, this underestimate may lead to negative S_{2n} values and, thus, to the formation of peninsula in the nuclear chart. Therefore, the calculated peninsulas may in some cases be an artifact of the mean-field approximation. The inclusion of correlations beyond mean field may increase the two-neutron separation energies S_{2n} and make them positive for neutron numbers from $N^{(1)}_{\rm drip}$ up to $N_{\rm penin}$. As a consequence, the peninsula will disappear and the two-neutron drip line will be located at $N^{(2)}_{\rm drip}$.

VII. THE TWO-PROTON DRIP LINE

The particle stability (and, as a consequence, a drip line) of a nuclide is specified by its separation energy, namely, the amount of energy needed to remove particle(s). If the two-neutron and the two-proton separation energies are positive, the nucleus is stable against two-nucleon emission. Conversely, if one of these separation energies is negative, the nucleus is unstable. Thus, the two-neutron or the two-proton drip line is reached when $S_{2n} \leqslant 0$ or $S_{2p} \leqslant 0$, respectively (see Fig. 12).

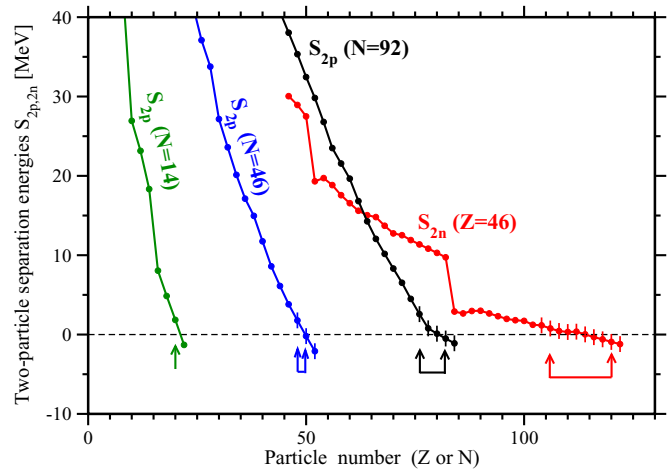

FIG. 12. (Color online) Schematic illustration of the dependence of the accuracy of the prediction for the position of the two-particle drip line on the slope of the two-particle separation energy curve as a function of the relevant particle number. The error bars for the calculated results show typical rms deviations (1 MeV) between theory and experiment (Table III). If these error bars would be taken into account (as it is effectively done when different CEDF's are compared), they would lead to the possible ranges of particle numbers corresponding to the two-particle drip line shown by arrows. For particle-bound nuclei the results for DD-PC1 are used. The separation energies for particle unbound nuclei ($S_{2n,2p} < 0$) represent extrapolations. They are used here only for illustration purposes.

The proton drip line was studied extensively more than a decade ago in the RHB framework with the finite-range Gogny pairing force D1S in Refs. [94–99]. However, the main emphasis was put on the one-proton drip line, for which, at the time of these studies, experimental data was more available than that for the two-proton drip line. In addition, only the NL3 parametrization [33] has been used in these studies. Therefore, no estimate of theoretical errors in the prediction of one- and two-proton drip lines is available. These gaps in our knowledge of the CDFT performance have been filled in Ref. [92], where the two-proton drip lines were studied with NL3*, DD-ME2, DD-PC1, and DD-MEδ. Theoretical uncertainties in the definition of two-proton drip line have been deduced.

In this section, we present a more detailed comparison of RHB results with the experiment. Figure 13 compares experimental data with calculated two-proton drip lines obtained with NL3*, DD-ME2, DD-PC1, and DD-MEδ. Note that the experimental two-proton drip line is delineated firmly or tentatively up to $Z = 84$ (see caption of Fig. 13 for details). The red line with small solid circles shows the calculated two-proton drip line. Nuclei to the left of this line are

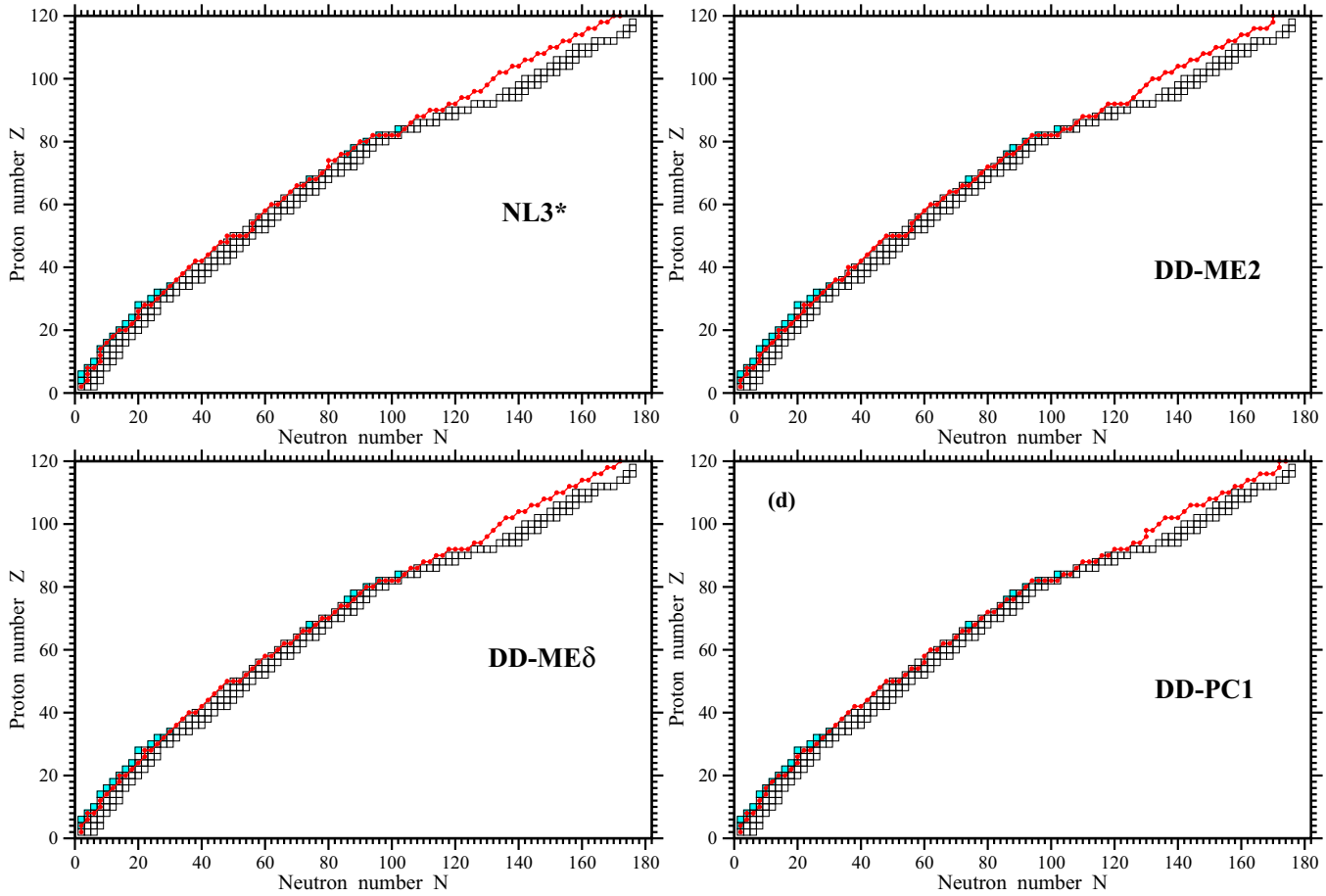

FIG. 13. (Color online) The calculated two-proton drip lines versus experimental data. For each isotope chain, the four experimentally known most proton-rich nuclei are shown by squares. Cyan shading of the squares is used for the nuclei located beyond the two-proton drip line ($S_{2p} < 0$). The experimental data are from Ref. [71]. The borderline between shaded and open squares delineates the known two-proton drip lines. Only in the cases of the $Z = 4$, 6, 8, 80, 82, and 84 isotope chains the locations of two-proton drip lines are firmly established because the masses of the nuclei on both sides of the drip line are directly and accurately measured. The two-proton drip line is only tentatively delineated for other isotope chains because either the masses of beyond the drip line nuclei are only estimated in Ref. [71] or beyond the drip line nuclei are not known experimentally. The red lines with small symbols show the calculated two-proton drip lines which go along the last two-proton bound nuclei.

proton unstable in the calculations. Nuclei which are proton unstable in experiment are shown by solid cyan squares. In the following discussion we concentrate on isotope chains containing proton-unstable nuclei because this provides the most reliable experimental information on the position of the two-proton drip line. One can see that NL3* tends to predict the two-proton drip line at too low values of the neutron number N. Indeed, experimentally known proton-unstable nuclei at $Z = 8$, 14, 16, 18, 20, 32, 34, 68, 76, 78, 80, and 82 (shown by cyan squares in Fig. 13) are predicted to be proton bound by NL3*. However, the two-proton drip line is predicted too early for the $Z = 52$ chain. Similar problems with the description of the proton unstable $Z = 4$, 8, 20, 32, 34, 76, 80, and 82 nuclei exist for DD-ME2. Note also that the two-proton drip line is predicted too early in the $Z = 26$ and 52 isotope chains in this CDFT parametrization. Also for DD-MEδ, proton unbound $Z = 4$, 8, 20, 30, 32, 80, 82 nuclei are predicted to be proton bound, and the two-proton drip line is predicted too early for $Z = 26$. A similar situation is observed with DD-PC1 for which $Z = 4$, 8, 16, 18, 20, 32, 34, 76, 80, and 82 proton unbound nuclei are bound in the calculations. In addition, the two-proton drip line is predicted too early for this parametrization for the $Z = 56$ isotopes.

The best reproduction of the two-proton drip line is achieved with DD-ME2 and DD-MEδ, which are characterized by the best residuals for two-proton separation energies S_{2p} (Table III). In general, the results of the calculations are very close to experimental data. This is because the proton drip line lies close to the valley of stability, so that extrapolation errors towards it are small. Another reason is the fact the Coulomb barrier provides a rather steep potential reducing considerably the coupling to the proton continuum. This leads to a relatively low density of the single-particle states in the vicinity of the Fermi level.

Because this density is comparable with the one for the nuclei away from two-proton drip line, the slope of the two-proton separation energy S_{2p} as a function of proton

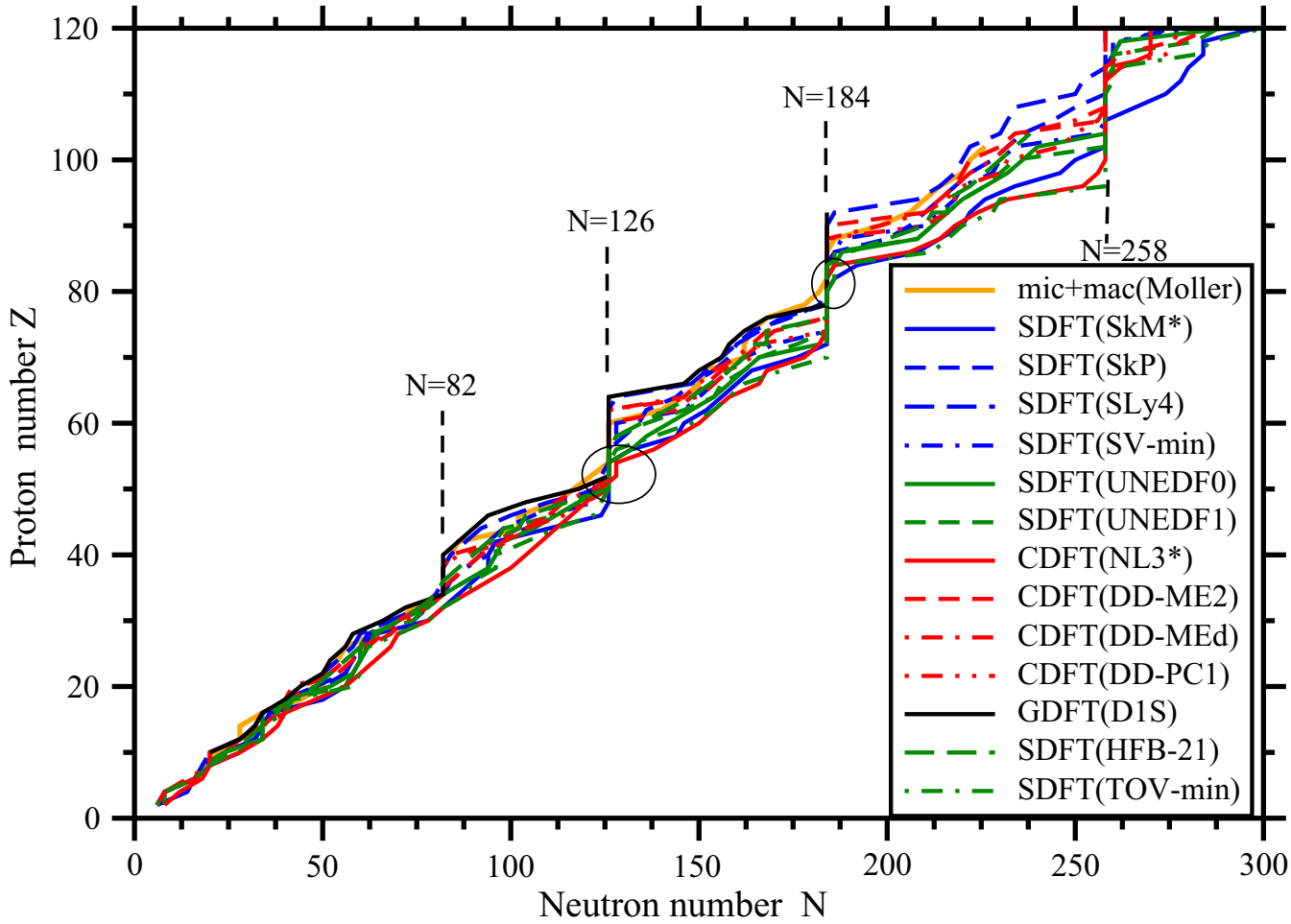

FIG. 14. (Color online) Two-neutron drip lines obtained in state-of-the-art DFT calculations. The regions of well-defined localization of the two-neutron drip line are encircled.

number for a given isotonic chain remains almost unchanged on approaching the two-proton drip line (Fig. 11). This slope is directly related to the uncertainties in the prediction of the position of two-proton drip line. For a given accuracy of the description of two-proton separation energies these uncertainties in the definition of position of the two-particle drip line increase with the decrease of the slope of $S_{2p,2n}$ (see Fig. 12). As a consequence, theoretical uncertainties for the two-proton drip line are rather small for $Z \leqslant 86$ but somewhat larger for higher Z (see Fig. 2 in Ref. [92]) owing to the increase of the single-particle level density and the related decrease of the slope of S_{2p} as a function of proton number (Fig. 11).

According to Fig. 2 of Ref. [92], theoretical uncertainties in the predictions of the position of two-proton drip line are either very small (two neutrons) or nonexistent for isotope chains with $Z \leqslant 86$. These small uncertainties may be a source of observed discrepancies between calculations and experiment for a number of isotope chains (for example, the ones with $Z =$ 4, 14, 16, 18, 20, 26, 68, 76, 78, and 80 in Fig. 2 of Ref. [92]). However, in a number of the cases (for example, in the $Z = 32$ and 34 isotopes chains) there is no uncertainty in the predicted position of two-proton drip line (Fig. 2 in Ref. [92]). Thus, the observed discrepancies between theory and experiment may be attributable to the limitations of the model description on the mean-field level. Indeed, it is well known that the Ge ($Z = 32$) [100] and Se ($Z = 34$) [88,101] isotopes show prolate-oblate shape coexistence and/or γ softness near the proton drip line. A similar shape coexistence is also observed in heavier Kr [87,89,102,103] and Rb [104] nuclei as well as in the $Z \sim 82$ proton drip-line nuclei [105,106]. By ignoring the correlations beyond mean field, which are expected to be most pronounced in light nuclei, we may introduce an error in the predicted position of two-proton drip line.

VIII. THE TWO-NEUTRON DRIP LINE

As discussed in Refs. [26,92], the situation is different for the two-neutron drip line. Figure 14 presents the compilation of known calculated two-neutron drip lines obtained with the state-of-the-art relativistic and nonrelativistic EDF's. They include four two-neutron drip lines obtained in the CDFT calculations of Ref. [92], which are tabulated in Table IV. Nonrelativistic results are represented by two-neutron drip lines obtained with the Gogny functional D1S [107] and with eight functionals of Skyrme type [26,93]. In addition, the

TABLE IV. Two-proton and two-neutron drip lines predicted by the CEDF's used in this work. Neutron numbers N (columns 2–9) corresponding to these drip lines are given for each even proton number Z (column 1). An asterisk at a neutron number at the two-neutron drip line indicates isotope chains with additional two-neutron binding at higher N values (peninsulas).

Proton	NL3*	Two-proton drip line		DD-PC1	NL3*	Two-neutron drip line		DD-PC1
number Z		DD-ME2	DD-MEδ			DD-ME2	DD-MEδ	
1	2	3	4	5	6	7	8	9
2	2	2	2	2	8	6	6	6
4	4	2	2	2	12	8	8	8
6	4	4	4	4	18	16	14	16
8	4	4	4	4	20	20	20	20
10	8	8	8	8	28	20	20	24
12	8	8	8	8	34	28	28	28
14	8	10	10	10	38	34	34	34
16	10	12	12	10	40	38	40	40
18	12	14	14	12	48	40	40	40
20	14	14	14	14	56	44	42	48
22	18	18	18	18	60	54	52	52
24	20	20	20	20	64	58	56	56
26	20	22	22	20	68	62	60	62
28	22	22	22	22	70	66	68	68
30	26	26	26	26	78	70	70	72
32	28	28	28	28	82	76	76	78
34	30	30	30	30	88	80	82	82
36	32	32	32	32	94	84	82	82
38	34	36	34	34	100	88	82	82
40	36	36	36	36	104	92	84	86
42	38	40	40	38	108	98	96	100
44	42	42	42	42	112	104	102	104
46	44	44	44	44	116	110	110	114
48	46	46	46	46	120	112	114	120
50	48	48	48	48	124	118	122	126
52	56	56	54	54	128	126	126	126
54	56	56	56	56	128	126	126	126
56	58	58	58	60	138	126	126	126
58	60	60	60	60	144	126	126	126
60	62	62	64	62	150	126	126	126
62	66	66	66	66	154	144	126*	126*
64	68	68	70	70	158	148	146	150
66	70	72	72	72	166	152	150	154
68	74	76	76	76	168	156	154	158
70	78	78	78	78	178	162	160	164
72	80	80	82	80	182	166	164	166
74	80	84	84	84	184	170*	168*	184
76	84	86	88	86	184	184	184	184
78	88	90	90	90	184	184	184	184
80	90	92	92	92	184	184	184	184
82	94	94	96	94	184	184	184	184
84	104	104	104	104	186	184	184	184
86	106	108	106	108	206	184	184	184
88	108	110	110	110	214	184	184	184*
90	112	116	114	116	218	184*	198*	210
92	118	120	118	120	224	210	210	216
94	122	126	126	126	232	214	216	218
96	126	128	130	130	252	218	218	220
98	130	130	132	130	256	220	222	230
100	132	132	134	134	258	222	228	232
102	134	136	136	136	258	230	232	246
104	138	140	140	142	258	234*	236	250
106	142	144	144	144	258	258	250	256

TABLE IV. (*Continued*.)

Proton number Z	NL3*	Two-proton drip line		DD-PC1	NL3*	Two-neutron drip line		DD-PC1
		DD-ME2	DD-MEδ			DD-ME2	DD-MEδ	
1	2	3	4	5	6	7	8	9
108	146	148	148	150	258	258	258	258
110	150	152	152	154	258	258	258	258
112	154	156	156	158	258	258	258	258
114	158	160	160	162	262	258	258	258
116	162	164	164	166	270	258	262	274
118	166	170	168	172	270	258	276	278
120	170	170	172	172	270	258*	278	286

two-neutron drip line from the microscopic + macroscopic calculations of Ref. [82] is shown. One can see that, with the exception of two encircled regions, the theoretical differences in the location of two-neutron drip line are much larger than the ones for the two-proton drip line. They are generally growing with increasing proton number.

One could ask whether there exist correlations between the position of two-neutron drip line for a given EDF and its nuclear-matter properties. With that goal Figs. 15 and 16 show the four most neutron-rich and the four least neutron-rich two-neutron drip lines among the 14 compiled lines. The nuclear-matter properties of the corresponding EDF's are shown in Table V. Let us consider the EDF's NL3* and DD-ME2 leading to the most and the least neutron-rich two-neutron drip lines amongst the relativistic functionals. It is tempting to associate the difference in the position of

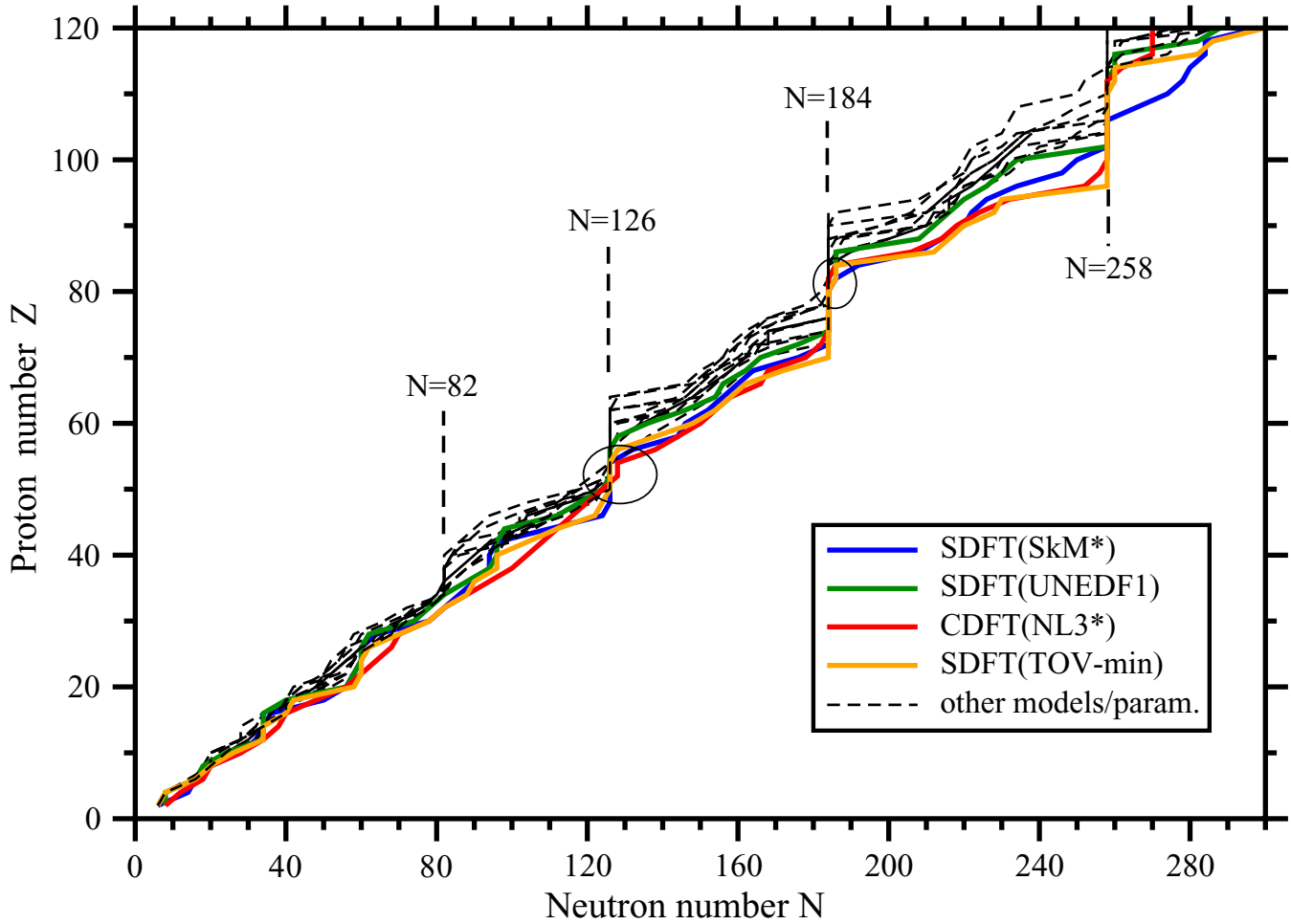

FIG. 15. (Color online) The same as in Fig. 14 but with the four most neutron-rich two-neutron drip lines shown in color and the rest in black.

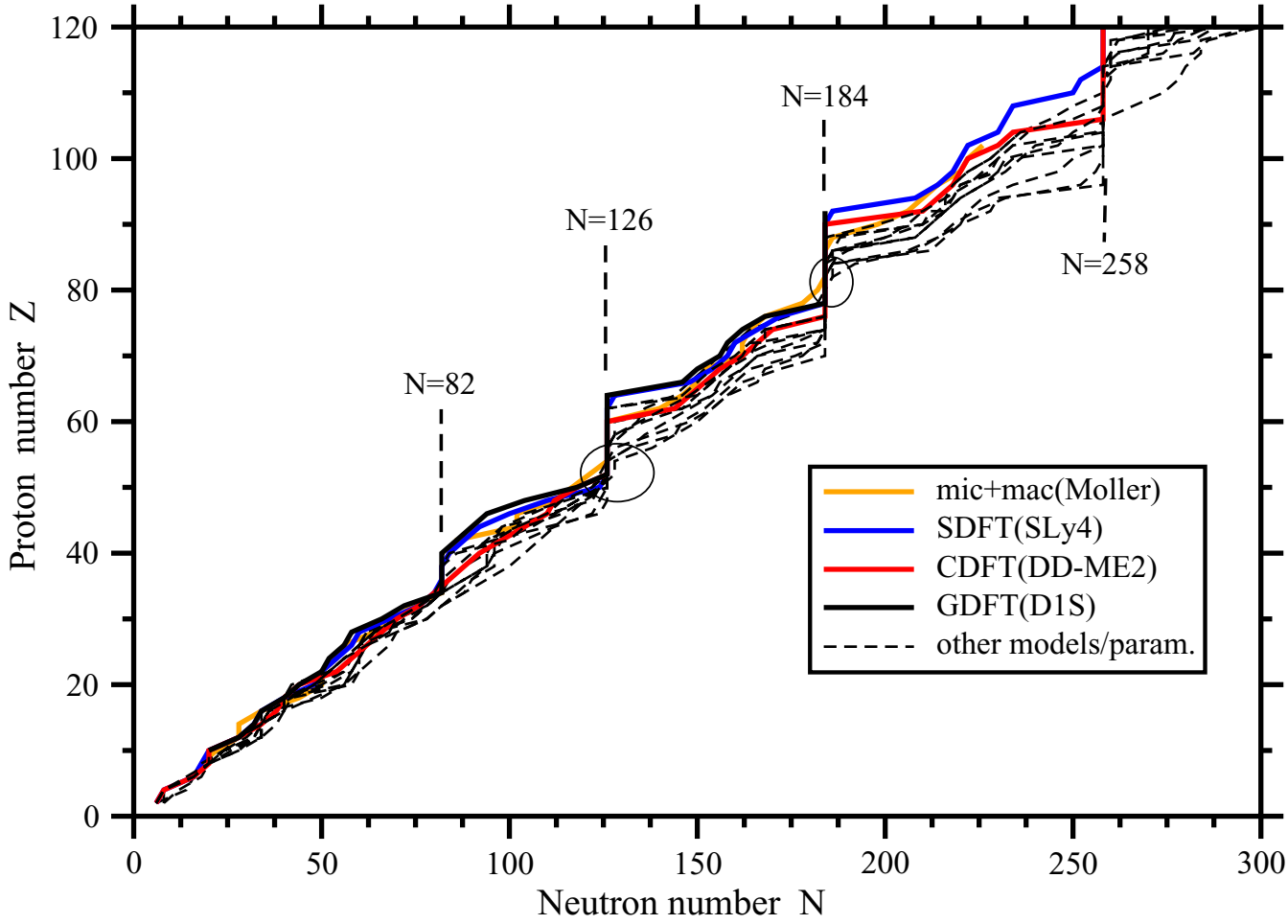

FIG. 16. (Color online) The same as in Fig. 14 but with the four least neutron-rich two-neutron drip lines shown in color and the rest in black.

TABLE V. Properties of symmetric nuclear matter at saturation for the energy density functionals used in Fig. 14: the density ρ_0, the energy per particle (E/A_∞), the incompressibility K_∞, the symmetry energy J and its slope L, and the isoscalar effective masses m^*/m of a nucleon at the Fermi surface. In the relativistic cases we show the Lorentz effective masses [108]. The results of the compilation [109] are used for the Skyrme functionals when possible.

Parameter	ρ_0 (fm^{-3})	$(E/A)_\infty$ (MeV)	K (MeV)	J (MeV)	L (MeV)	m^*/m
Four most neutron-rich two-neutron drip lines						
NL3* [24]	0.150	–16.31	258	38.68	122.6	0.67
SkM* [109,110]	0.160	–15.77	217	30.03	45.8	0.79
UNEDF1 [111]	0.159	–15.80	220	28.99	40.0	0.99
TOV-min [93]	0.161	–15.93	222	32.30	76.0	0.94
Four least neutron-rich two-neutron drip lines						
mic + mac [FRDM] [82]		–16.25	240	32.73		1.00
DD-ME2 [23]	0.152	–16.14	251	32.40	49.4	0.66
SLy4 [109,112]	0.160	–15.97	230	32.00	45.9	0.69
D1S [Gogny] [113]	0.160	–15.90	210	32.00		0.70
Remaining parametrizations (drip lines in the middle)						
UNEDF0 [111]	0.161	–16.06	230	30.54	45.1	0.90
DD-MEδ [12]	0.152	–16.12	219	32.35	52.9	0.61
SkP [109,75]	0.163	–15.95	201	30.00	19.7	1.00
SV-min [109,114]	0.161	–15.91	222	30.66	44.8	0.95
DD-PC1 [11,79]	0.152	–16.06	230	33.00	68.4	0.66
HFB-21 [BSk21] [115]	0.158	–16.05	246	30.00	46.6	0.80

two-neutron drip lines with different symmetry energies J ($J = 32.30$ MeV for DD-ME2 and $J = 38.68$ MeV for NL3*) and the slope parameter L of the symmetry energy at saturation density ($L = 51.26$ MeV for DD-ME2 and $L = 123$ MeV for NL3*). However, a detailed comparison of the positions of the 14 two-neutron drip lines presented in Figs. 14, 15, and 16 with nuclear-matter properties of their EDF's (Table V) does not reveal clear correlations between the locations of two-neutron drip lines and the nuclear-matter properties of the corresponding functional. In fact, for nuclei close to the neutron drip line the Fermi surface is very small and negative close to the continuum limit and it changes only slowly with the neutron number. The precise position of the drip line therefore depends very much on the behavior of the tail of the neutron density. At these very low densities the properties J and L of nuclear matter at saturation are not really relevant.

Possible sources of the uncertainties in the position of the two-neutron drip line have been discussed in Ref. [92]. They include the isovector properties of the EDF's [26] and the underlying shell structure connected with inevitable inaccuracies of the single-particle energies in the DFT description [92].

The isovector properties of an EDF define the depth of the nucleonic potential with respect to the continuum and may thus affect the location of two-neutron drip line. However, such uncertainties in the depth of the nucleonic potential exist also in known nuclei (see discussion in Sec. IV C of Ref. [67]). They cannot describe the observed features completely.

The shell structure effects are clearly visible in the fact that for some combinations of Z and N there is basically no (or very little) dependence of the predicted location of the two-neutron drip line on the CDFT parametrization. Such a weak (or vanishing) dependence, seen in all model calculations, is especially pronounced at spherical neutron shell closures with $N = 126$ and 184 around the proton numbers $Z = 54$ and 80, respectively. In addition, a similar situation is seen in the CDFT calculations at $N = 258$ and $Z \sim 110$. This fact is easy to understand because of the large neutron shell gap at the magic neutron numbers in all DFT's.

Inevitable inaccuracies in the DFT description of single-particle energies [49,67] also contribute to increasing uncertainties in the prediction of two-neutron drip-line position on moving away from these spherical shell closures. This move induces deformation. The comparison of Figs. 14 and 17 shows that there is a close correlation between the nuclear deformation at the neutron drip line and the uncertainties in their prediction. The regions of large uncertainties correspond to transitional and deformed nuclei. Again this is caused by the underlying level densities of the single-particle states. The spherical nuclei under discussion are characterized by large shell gaps and a clustering of highly degenerate single-particle states around them. Deformation removes this high degeneracy of single-particle states and leads to a more equal distribution of the single-particle states with energy. Moreover, the density of bound neutron single-particle states close to the neutron continuum is substantially larger than that on the proton drip line which leads to a small slope of two-neutron separation energies S_{2n} as a function of neutron number in the vicinity of two-neutron drip lines for medium- and heavy-mass nuclei (see Fig. 10). This slope is smaller than the slope of two-proton separation energies S_{2p} as a function of proton number in the vicinity of the two-proton drip line (Fig. 11). Note that the S_{2n} and S_{2p} values are described with a similar accuracy in the various parametrizations (Table III). However, the difference in the slope of S_{2n} and S_{2p} as a function of proton and neutron numbers translates into much larger uncertainties in the definition of the position of the two-neutron drip line as compared with the two-proton drip line. This also indicates that the predictions for the two-neutron drip line depend more sensitively on the single-particle energies than those for two-proton drip line.

IX. DEFORMATIONS

The solution of the variational equations of DFT yields values for the single-particle density $\rho(\boldsymbol{r})$. Therefore, DFT not only allows us to derive the binding energies of the system but, in addition, all quantities depending on $\rho(\boldsymbol{r})$. In this section we consider the charge quadrupole and hexadecupole moments,

$$Q_{20} = \int d^3r \rho(\boldsymbol{r}) (2z^2 - r_\perp^2), \tag{31}$$

$$Q_{40} = \int d^3r \rho(\boldsymbol{r}) (8z^4 - 24z^2 r_\perp^2 + 3r_\perp^4), \tag{32}$$

with $r_\perp^2 = x^2 + y^2$. In principle, these values can be directly compared with experimental data. However, it is more convenient to transform these quantities into dimensionless deformation parameters β_2 and β_4,

$$Q_{20} = 2\sqrt{\frac{4\pi}{5}} \frac{3}{4\pi} Z R_0^2 \beta_2, \tag{33}$$

$$Q_{40} = 8\sqrt{\frac{4\pi}{9}} \frac{3}{4\pi} Z R_0^4 \beta_4, \tag{34}$$

where $R_0 = 1.2A^{1/3}$. Equation (33) is used also in the extraction of experimental β_2 deformation from measured data [116]. This justifies its application despite the fact that this simple linear expression ignores the contributions of higher power/multipolarity deformations to the charge quadrupole moment. Including higher powers of β_2, as in Ref. [117], yields values of β_2 that are $\approx$10% lower. In Figs. 17 and 19 we show the distribution of proton quadrupole β_2 and hexadecapole β_4 deformations in the (N,Z) plane for the CEDF's NL3*, DD-ME2, DD-MEδ, and DD-PC1.

Direct experimental information on the deformations of nuclei can be obtained from Coulomb excitation and lifetime measurements [116]. An alternative method is to derive a quadrupole moment from the $2^+ \rightarrow 0^+$ transition energy by using the Grodzins relation [118] or its later refinements [119]. However, these prescriptions are applicable only to well-deformed nuclei. In general, it is estimated that experimental methods give an accuracy of around 10% [119] for the static charge quadrupole deformation β_2 in the case of well-deformed nuclei. The error can be larger in transitional nuclei because in this case the deformation extracted from experimental data will contain also dynamic deformation resulting from zero-point oscillations of the nuclear surface in the ground state [120].

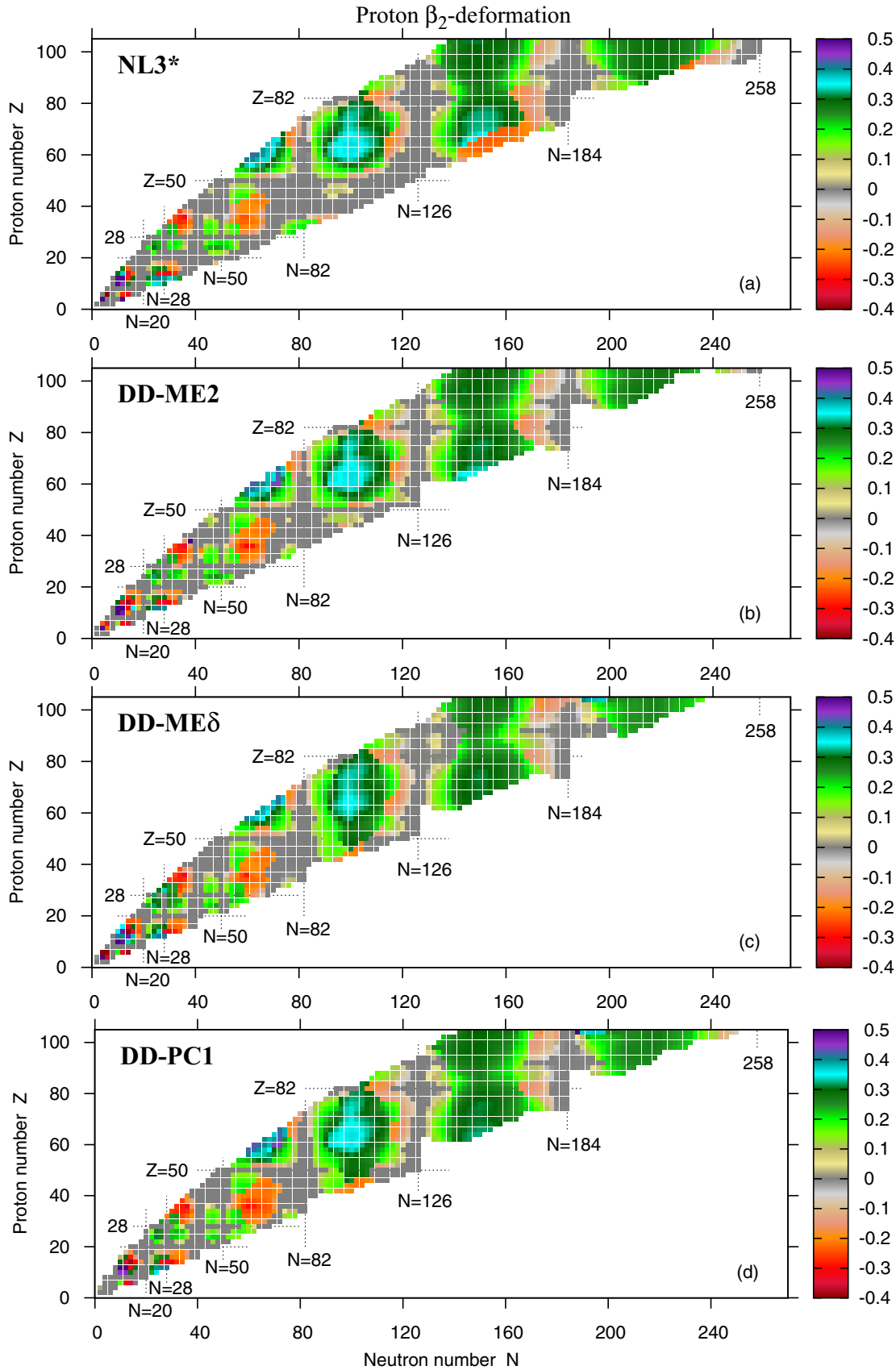

FIG. 17. (Color online) Charge quadrupole deformations β_2 obtained in the RHB calculations with indicated CEDF's.

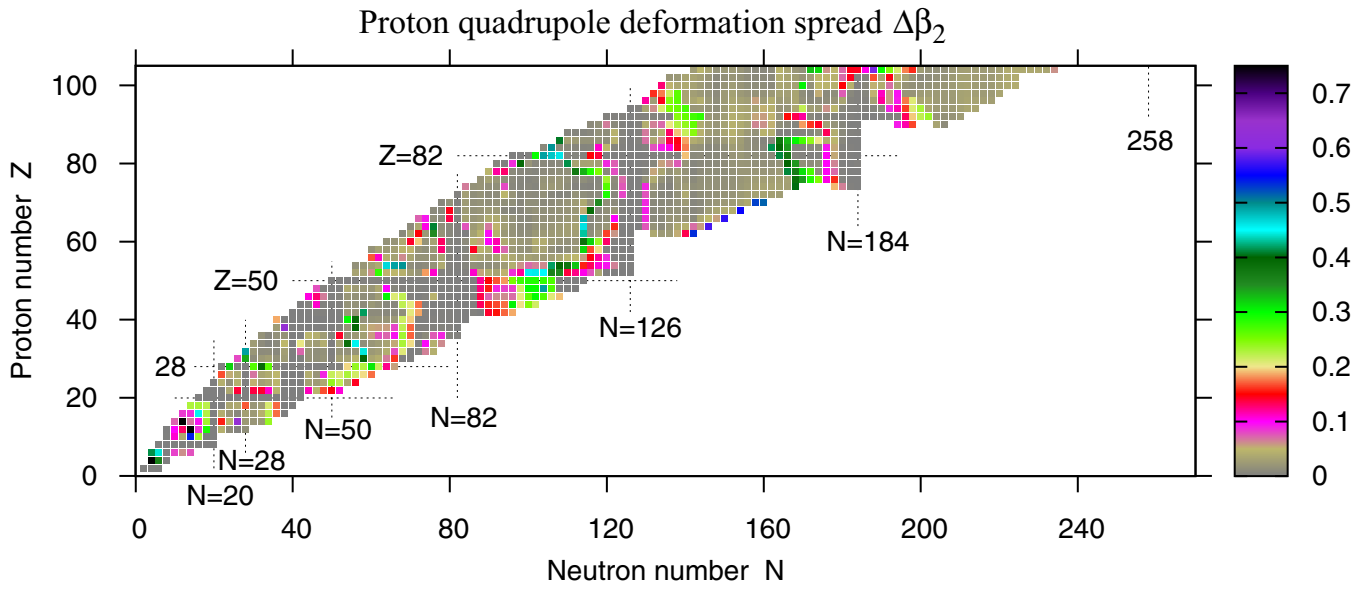

FIG. 18. (Color online) Proton quadrupole deformation spreads $\Delta\beta_2(Z,N)$ as a function of proton and neutron number. $\Delta\beta_2(Z,N) = |\beta_2^{\max}(Z,N) - \beta_2^{\min}(Z,N)|$, where $\beta_2^{\max}(Z,N)$ and $\beta_2^{\min}(Z,N)$ are the largest and smallest proton quadrupole deformations obtained with four employed CEDF's for the (Z,N) nucleus.

These considerations basically limit the possibilities of a comparison between calculated and experimental β_2 deformations to the well-deformed nuclei in the rare-earth and actinide regions. Although deformation exists also in the ground states of nuclei in many other regions, the potential energy surfaces of these nuclei are, in general, soft in β_2 or γ deformation, leading to the phenomena of shape fluctuations, shape coexistence [121], and quantum phase transitions [122]. For such situations, the mean-field description is not completely adequate, and, thus, a comparison between theoretical and experimental deformation properties is not conclusive.

A systematic comparison between calculated and experimental static charge quadrupole deformations β_2 has already been performed in each of these regions (with NL3* [50] in the actinides and with DD-ME2 and DD-PC1 [11] in the rare-earth region). They describe the experimental data well, typically within the experimental uncertainties. Figure 18 shows that in these regions of well-deformed nuclei the spread of the theoretical predictions, i.e., the difference between results obtained with various CEDF's, is rather small for static quadrupole deformations β_2. Thus, we do not repeat such a comparison here.

The distribution of calculated static quadrupole deformations β_2 is similar in all four CEDF's under consideration (see Fig. 17). The biggest difference between these results is related to the presence of two regions of oblate deformation at ($Z \sim 70$, $N \sim 160$) and ($Z \sim 95$, $N \sim 230$) in the calculations with NL3*. These regions are absent in the other CEDF's. However, this is a consequence of the fact that the two-neutron drip line is located at higher N values in NL3* as compared with other CEDF's. As a result, these regions are neutron-unbound for DD-ME2, DD-MEδ, and DD-PC1.

The width of the gray region in Fig. 17 (the gray color corresponds to spherical and near-spherical shapes) along a specific magic number corresponding to a shell closure indicates the impact of this shell closure on the structure of the neighboring nuclei. Note that proton and neutron shell gaps act simultaneously in the vicinity of doubly magic spherical nuclei. Thus, the effect of a single gap is more quantifiable away from these nuclei. One can see in Fig. 17 that the neutron $N = 82$, 126, and 184 shell gaps have a more pronounced effect on the nuclear deformations as compared with the proton shell gaps at $Z = 50$ and $Z = 82$. This feature is common for all the CEDF's under investigation in this paper.

It is interesting to compare the RHB results with those obtained in nonrelativistic models. The comparison of Fig. 17 in the present paper with HFB results based on the Gogny D1S force in Fig. 3 a of Ref. [107], with HFB results based on six Skyrme EDF's in Fig. 2 of the Supplemental Material to Ref. [26], and with the microscopic + macroscopic model in Fig. 9 of Ref. [82] show that the general structure of the distribution of charge quadrupole deformations β_2 in the nuclear chart is similar in all model calculations. Differences between models emerge mostly at the boundaries between the regions of different types of deformation, i.e., in the transitional regions, where the energy surfaces are rather flat and static deformations are not well defined. These are the boundaries between the regions of prolate and oblate shapes and between the regions of deformed and spherical shapes. This comparison also reveals that, similar to our relativistic results, also in nonrelativistic calculations the neutron shell gaps with $N = 82$, 126, and 184 have a more pronounced effect on the nuclear deformations than the proton shell gaps with $Z = 50$ and $Z = 82$.

Figure 18 shows the spreads $\Delta\beta_2(Z,N)$ among four CEDF's for the predicted charge quadrupole deformations. One can see that this spread is either nonexistent or very small for spherical or nearly spherical nuclei as well as for well-deformed nuclei in the rare-earth and actinide region. The largest uncertainties for predicting the equilibrium quadrupole

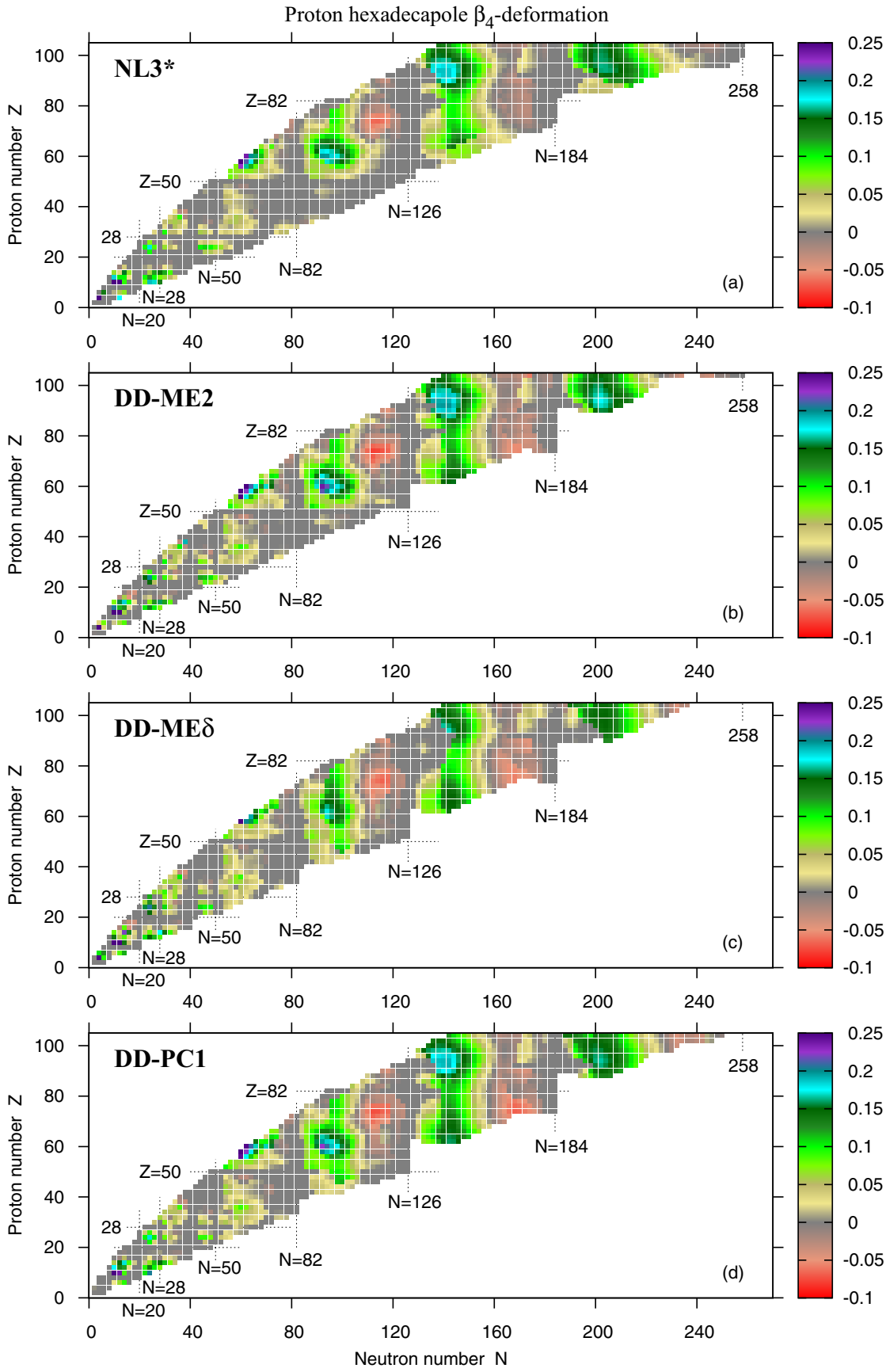

FIG. 19. (Color online) Proton hexadecapole deformations β_4 obtained in the RHB calculations with the indicated CEDF's.

deformations exist at the boundaries between regions of different deformations. They are extremely high in the regions of the prolate-oblate shape coexistence, indicating that the ground state in a given nucleus can be prolate (oblate) in one CEDF and oblate (prolate) in another CEDF. These uncertainties are more modest on the boundaries of the regions of spherical and deformed (oblate or prolate) shapes. It is well known that such nuclei are difficult to describe precisely at the mean-field level [7,121,123]. Correlations going beyond mean field have to be taken into account [87,88,105,124] and shape fluctuations do not allow a precise definition of deformation parameters. However, even if such correlations and fluctuations are taken into account properly by methods based on DFT and going beyond the mean field, there remain deficiencies of the current generations of the DFT models with respect of the description of single-particle energies [87]. Indeed, when we compare the profile of the potential energy surface (PES) as a function of the deformation in spherical or well-deformed nuclei with that in transitional nuclei, we find that this profile depends for transitional nuclei much more sensitively on the underlying single-particle structure than in the other two cases. However, it is well known that the single-particle energies (both spherical and deformed) are not very accurately described at the DFT level (see Refs. [49,67] and references quoted therein). Considering that the PES's obtained at the mean-field level form the starting points of many beyond mean field calculations, further improvement in the description of the single-particle energies is needed to describe experimental data in transitional and shape-coexistent nuclei reliably and consistently across the nuclear chart with a high level of predictive power by the methods going beyond mean field.

In Figs. 19 and 20 we present the distribution of the calculated charge hexadecapole deformations β_4 in the (N,Z) plane and the spreads (1) for this observable. The detailed comparison of Figs. 20 and 19 reveals a large degree of correlation between the uncertainties in the predictions of proton quadrupole and hexadecapole deformations. Similar to quadrupole deformation (see discussion above), the largest spread of the calculated hexadecapole deformations exists near the borderline separating the regions with different quadrupole deformations. For nonrelativistic theories, the distribution of hexadecapole deformations of ground states in the nuclear chart has been published so far only in the microscopic + macroscopic (MM) model (see Fig. 11 in Ref. [82]). Although the general trends for hexadecapole deformations seem to be similar with our results, the direct comparison between the two models is very difficult. In the MM model [82], the deformation parameters determine the shape of the potentials and the multipole moments of the corresponding density distributions are complicated nonlinear functions of deformations: $Q_{L0} = Q_{L0}(\beta_2,\beta_4)$ for $(L = 2,4)$. On the contrary, in the present investigation the deformation parameters are defined from the Q_{L0} moments via the linear expressions (33) and (34), where all the nonlinear coupling effects are neglected (see, for instance, Ref. [125]).

In Fig. 21 we present isovector deformations $\beta_2^{IV} = \beta_2(\nu) - \beta_2(\pi)$. So far, there are no experimental data on such a quantity. However, it is important to understand how consistent are the predictions for β_2^{IV} among modern DFT models. The results presented in the Supplemental Material of Ref. [26] show that for the absolute majority of nuclei Skyrme functionals favor smaller neutron β_2 deformations as compared with the proton values. This result has been verified for six Skyrme EDF's; although some differences between Skyrme parametrizations exist, it appears as a general rule. The situation is different in covariant functionals. The neutron β_2 deformation is larger than the corresponding proton deformation in approximately 2/3 of the nuclei, while in 1/3 of the nuclei the opposite situation is seen. The absolute

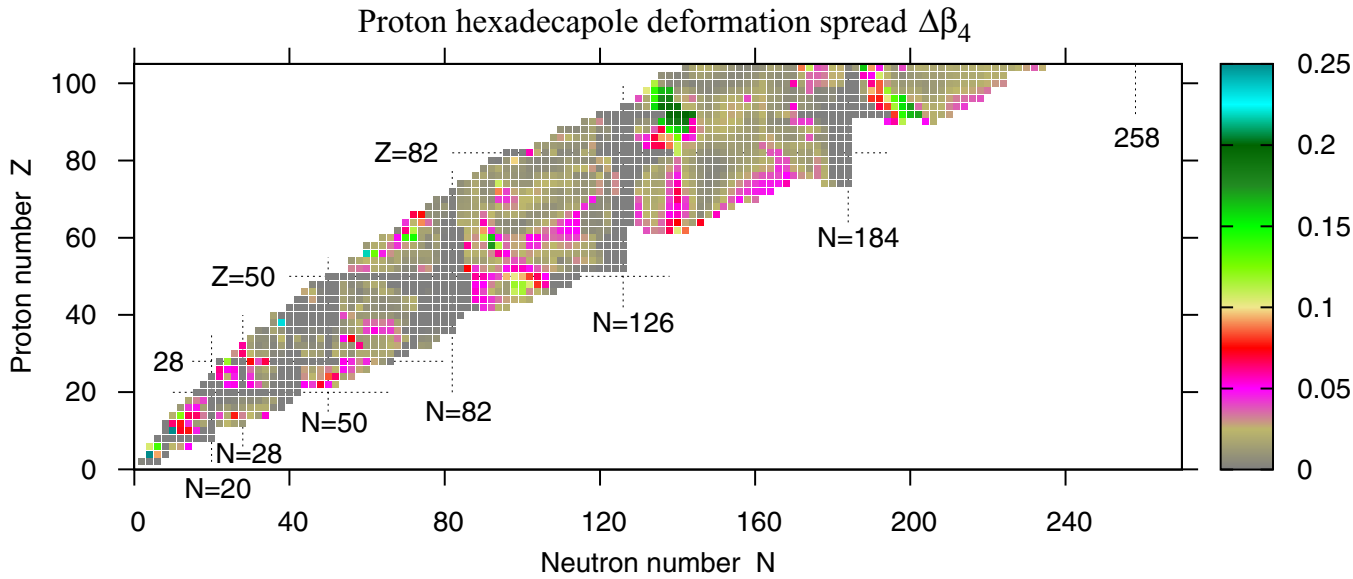

FIG. 20. (Color online) Proton hexadecapole deformation spreads $\Delta\beta_4(Z,N)$ as a function of the proton and neutron numbers. $\Delta\beta_4(Z,N) = |\beta_4^{\max}(Z,N) - \beta_4^{\min}(Z,N)|$, where $\beta_4^{\max}(Z,N)$ and $\beta_4^{\min}(Z,N)$ are the largest and smallest proton hexadecapol deformations obtained with four employed CDFT parametrizations for the (Z,N) nucleus.

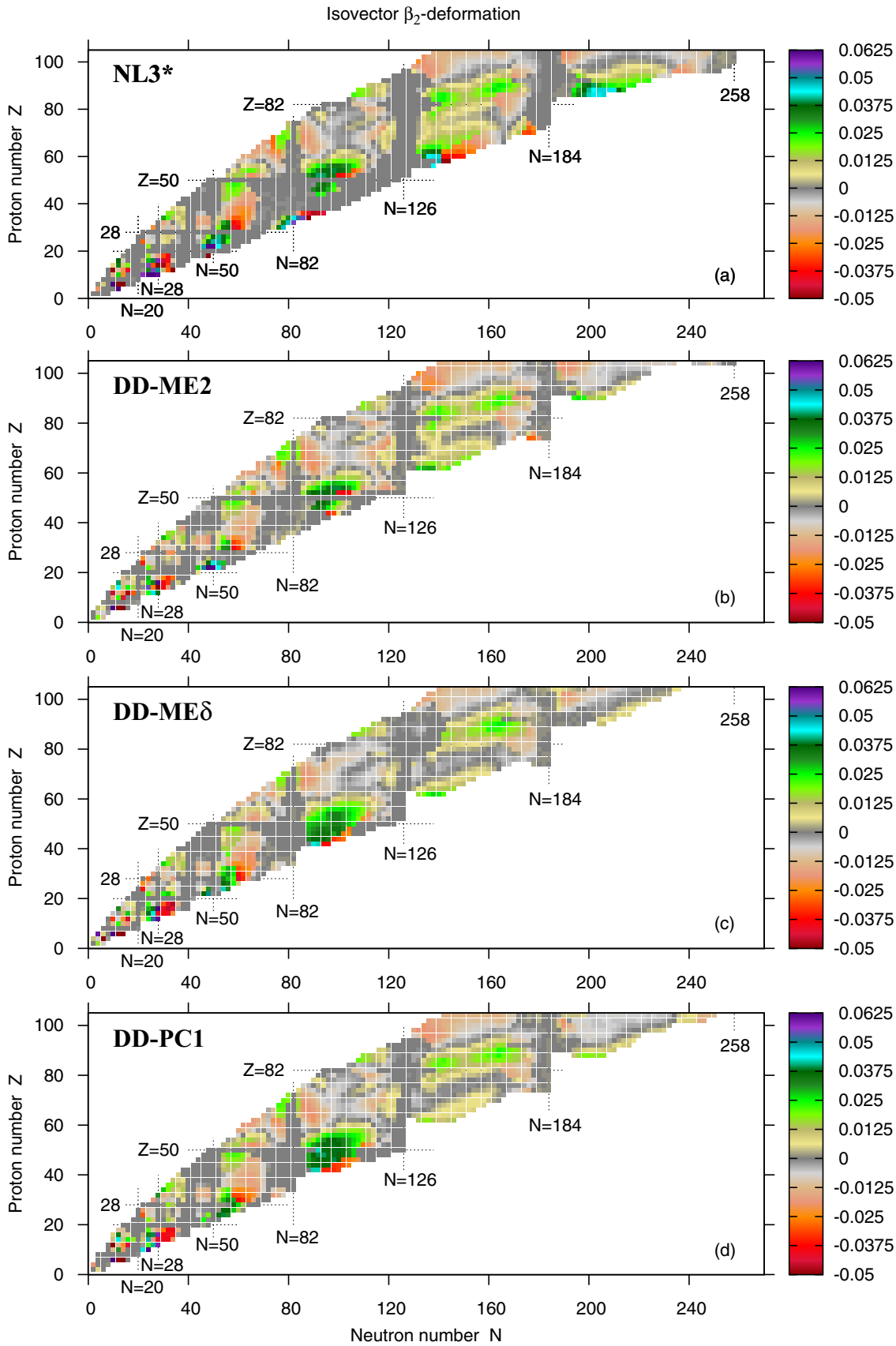

FIG. 21. (Color online) Isovector $\beta_2^{IV} = \beta_2(\nu) - \beta_2(\pi)$ deformations obtained in the RHB calculations with the indicated CDFT parametrizations.

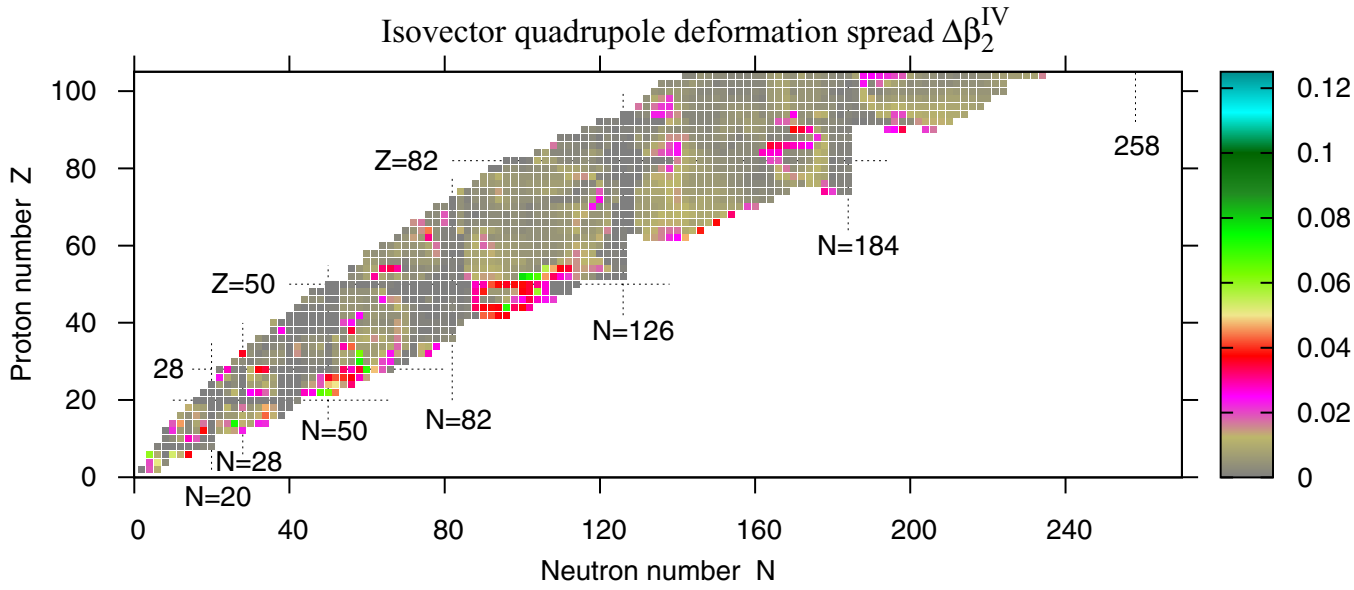

FIG. 22. (Color online) Isovector quadrupole deformation spreads $\Delta\beta_2^{IV}(Z,N)$ as a function of proton and neutron number. $\Delta\beta_2^{IV}(Z,N) = |\beta_{2,\max}^{IV}(Z,N) - \beta_{2,\min}^{IV}(Z,N)|$, where $\beta_{2,\max}^{IV}(Z,N)$ and $\beta_{2,\min}^{IV}(Z,N)$ are the largest and smallest isovector quadrupole deformations, respectively, obtained with four CDFT parametrizations for the (Z,N) nucleus.

difference between proton and neutron β_2 deformations is less than 0.0125 in approximately 70% of the deformed nuclei. As illustrated by Fig. 22, these results do not depend much on the selection of the CEDF. On the contrary, the difference exceeds 0.02 for at least half of the deformed nuclei in the Skyrme DFT (see Fig. 3 in Supplemental Material of Ref. [26]). Thus, the MM model, which assumes the same deformations for protons and neutrons, is better justified in CDFT than in Skyrme DFT. One also should note that in CDFT there are several regions in the periodic chart, where the differences of neutron and proton quadrupole deformations become substantial. These are ($Z \sim 16, N \sim 34$), ($Z \sim 28$, $N \sim 60$), and $Z \sim 50$, $N \sim 100$) regions located in the vicinity of two-neutron drip line (Fig. 21). They are present in all CDFT parametrizations. At the moment we do not understand all these details, but we have to emphasize that most of the regions with large differences between neutron and proton deformations are close to the neutron drip line, where the neutron densities are more dilute than those of the protons. In addition, the neutron densities are more deformed than the proton ones in these regions. Of course, in the future it would be interesting to investigate these facts in more detail.

X. CHARGE RADII AND NEUTRON SKIN THICKNESS

The charge radii were calculated from the corresponding point proton radii as

$$r_{ch} = \sqrt{\langle r^2 \rangle_p + 0.64}\ \text{fm}, \tag{35}$$

where the factor 0.64 accounts for the finite-size effects of the proton. Here we have neglected the small contributions to the charge radius originating from the electric neutron form factor and the electromagnetic spin-orbit coupling [126,127] as well as the corrections owing to the center-of-mass motion. Note that in the fits of the three density functionals NL3* [24], DD-ME2 [23], and DD-MEδ [12] the same finite size of the proton of 0.8 fm has been used and that the functional DD-PC1 [11] has been adjusted only to nuclear binding energies.

The accuracy of the description of charge radii is illustrated on the example of the CEDF DD-PC1 in Fig. 23. We do not present such a comparison for the CEDF's NL3*, DD-ME2, and DD-MEδ because they show very similar results. This similarity is clearly seen from Fig. 24, which presents the spreads (1) in the theoretical results on charge radii, and from Table VI, which presents the rms deviations between calculated and experimental radii. These comparisons are based on the latest compilation of experimental charge radii in Ref. [128], which includes charge radii for 351 even-even nuclei,

One can see that the calculations provide, in general, a good description of experimental data. However, there are four exceptions. First, there are very light nuclei He, Be, and C [Fig. 23(a)], where the mean-field description has obvious limitations. The discrepancy between theory and experiment is especially pronounced in the case of the He nuclei. Then there is a substantial discrepancy between theory and experiment for charge radii of Se, Kr, and Sr isotopes at neutron numbers $N = 38$–46 [see Fig. 23(b)]. The calculated ground state quadrupole deformations of these nuclei are predicted to be either spherical or near spherical (see Fig. 17). However, the PES's are soft. This indicates that a proper description of their structure requires the inclusion of beyond-mean-field correlations. Next, the ground states of some proton-rich Hg and Pb isotopes are predicted to be oblate (or prolate), in contradiction with experiment. These earlier observed features [129] are in part attributable to incorrect position of the

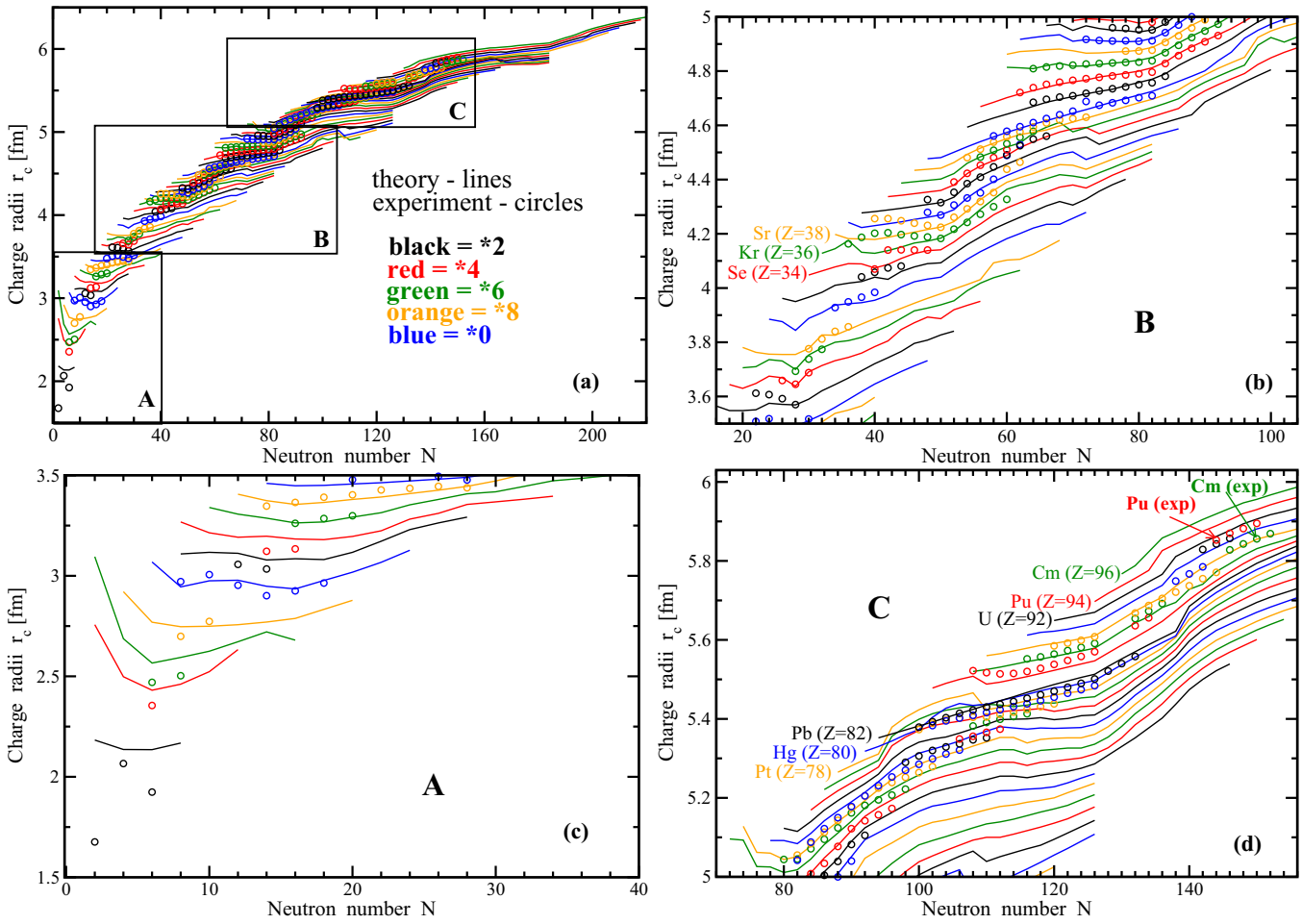

FIG. 23. (Color online) Experimental and theoretical charge radii as a function of neutron number. The calculations are performed with DD-PC1. Black, red, green, orange, and blue colors are used for isotope chains with proton numbers ending with 2, 4, 6, 8, and 0, respectively. The experimental data are taken from Ref. [128]. Panels (b), (c), and (d) show the comparison in an enlarged scale.

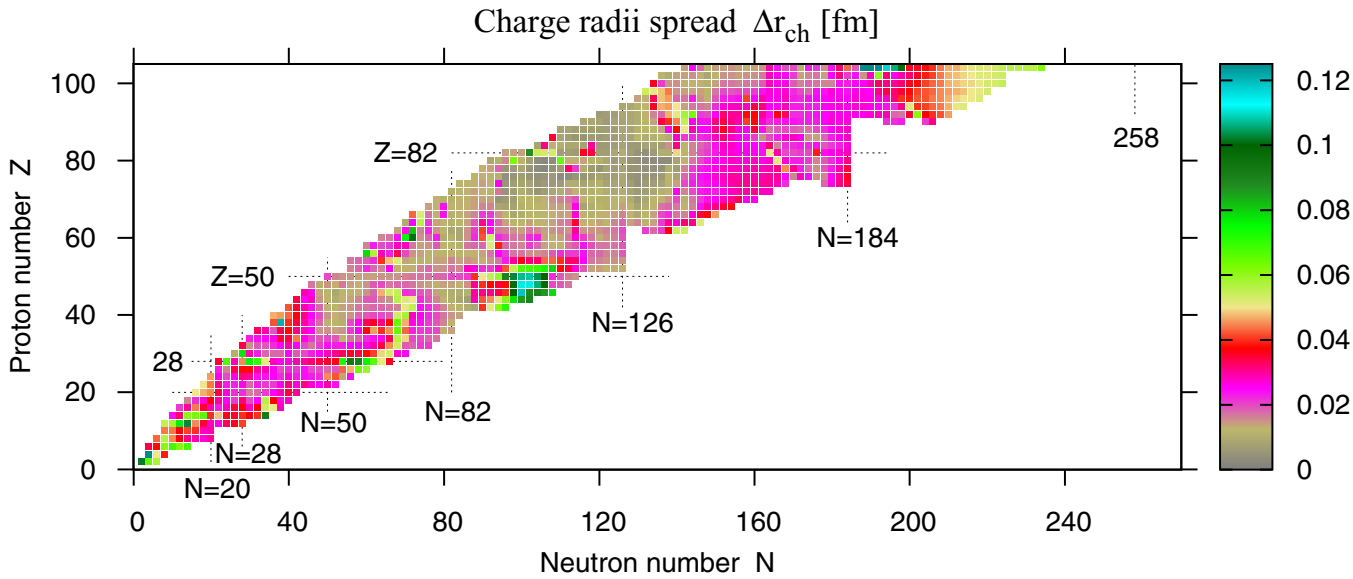

FIG. 24. (Color online) Charge radii spread $\Delta r_{\rm ch}(Z,N)$ as a function of proton and neutron number. $\Delta r_{\rm ch}(Z,N) = |r_{\rm ch}^{\rm max}(Z,N) - r_{\rm ch}^{\rm min}(Z,N)|$, where $r_{\rm ch}^{\rm max}(Z,N)$ and $r_{\rm ch}^{\rm min}(Z,N)$ are the largest and the smallest charge radii obtained with the four CDFT parameterizations for the (Z,N) nucleus.

TABLE VI. The rms deviations $\Delta r_{\rm ch}^{\rm rms}$ between calculated and experimental charge radii. They are given in fm for the indicated CEDF's. For the calculations of the rms values, all experimental data are used in column 2, while the data on radii of He ($Z = 2$) and Cm ($Z = 96$) isotopes are excluded in column 3. See text for the discussion of these cases.

CEDF	$\Delta r_{\rm ch}^{\rm rms}$ (fm)	$\Delta r_{\rm ch}^{\rm rms}$ (fm)
1	2	3
NL3*	0.0407	0.0283
DD-ME2	0.0376	0.0230
DD-MEδ	0.0412	0.0329
DD-PC1	0.0402	0.0253

proton $1h_{9/2}$ spherical subshell [48,129] and they are present in all the CEDF's used here (see Fig. 17). When comparing theory with experiment we use for these nuclei the radii from the minimum of the PES corresponding to the experimental minimum, i.e., the spherical minimum for the $N = 104$–114 Pb isotopes and the oblate minimum for the $N = 100$–108 Hg isotopes. Finally, the last case is related to the unusual behavior of the charge radii in the U-Pu-Cm isotopes [see Fig. 23(d)]. For a fixed neutron number, the increase of proton number leads in these isotopes to an increase of the calculated charge radius. Such a feature is seen not only for the CDFT results, but also for the results of the nonrelativistic DFT calculations based on the Gogny D1S force (see Supplemental Material to Ref. [107]). However, in experiment the charge radii of the Cm ($Z = 96$) nuclei are lower than those of Pu ($Z = 94$) and U ($Z = 92$). This is the only case in the nuclear chart where such an inversion exists. Considering that both the ground state quadrupole deformations are very stable in this region, i.e., their variations with particle number are much less pronounced than in the rare-earth region, and that CDFT describes the experimental deformations in the actinides well [48,50], it is impossible based on the current CDFT's and on the Gogny functional D1S to understand this highly unusual behavior of experimental charge radii in the Cm isotopes.

In neutron-rich nuclei the excess of neutrons over protons creates a neutron skin. The neutron skin thickness is commonly defined as the difference of proton and neutron root-mean-square (rms) radii,

$$r_{\rm skin} = \langle r_n^2 \rangle^{1/2} - \langle r_p^2 \rangle^{1/2} . \tag{36}$$

The neutron skin thickness is an important indicator of isovector properties. It is closely related with a number of observables in finite nuclei which are sensitive to isovector properties [25,130,131] and it affects the physics of neutron stars [25,132–134].

The experimental data on the neutron skin thickness in ^{208}Pb is contradictory. On the one hand, there is a large set of experiments which suggests that the neutron skin is around 0.2 fm or slightly smaller (see Table 1 in Ref. [136]). However, these experimental data are extracted in model-dependent ways (see Ref. [137] and references quoted therein). The neutron skin thicknesses $r_{\rm skin} = 0.161 \pm 0.042$ [136] and $r_{\rm skin} = 0.190 \pm 0.028$ [138] obtained recently from the energy of the antianalog GDR rely on relativistic proton-neutron quasiparticle random-phase approximation calculations based on the RHB model. Another recent value of the neutron skin thickness of $r_{\rm skin} = 0.15 \pm 0.03({\rm stat})^{+0.01}_{-0.03}({\rm sys})$ fm has been extracted from coherent pion photoproduction cross sections [139]. However, the extraction of information on the nucleon density distribution depends on the comparison of the measured (γ,π^0) cross sections with model calculations. Alternatively, a measurement using an electroweak probe has very recently been carried out in parity violating electron scattering on nuclei (PREX) [37]. It utilizes the preferential coupling of the exchanged weak boson to neutrons. The electroweak probe has the advantage over experiments using hadronic probes that it allows a nearly model-independent extraction of the neutron radius that is independent of most strong interaction uncertainties [140]. However, a first measurement at a single momentum

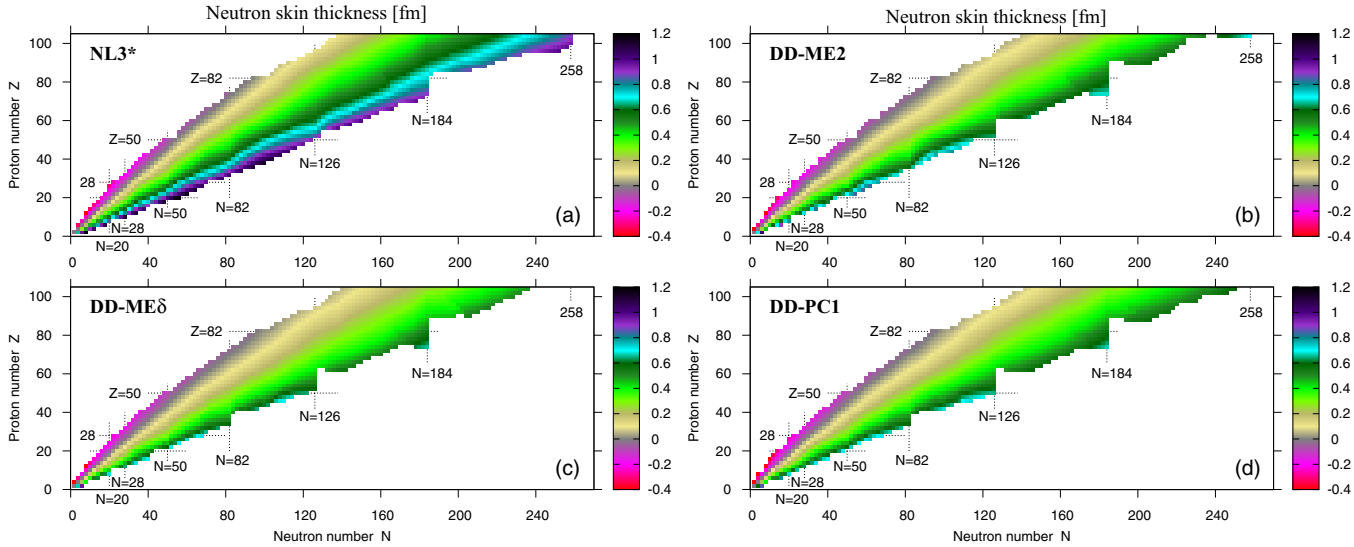

FIG. 25. (Color online) Neutron skin thicknesses obtained in RHB calculations with several CEDF's.

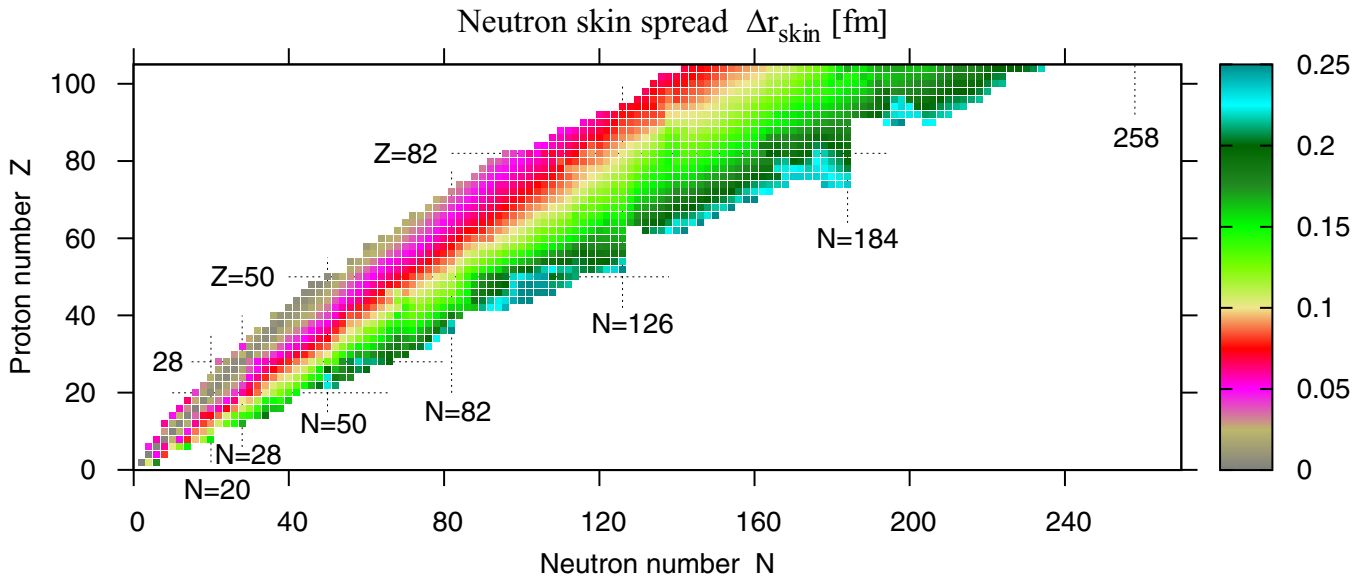

FIG. 26. (Color online) Neutron skin thickness spreads $\Delta r_{skin}(Z,N)$ as a function of proton and neutron number. $\Delta r_{skin}(Z,N) = |r^{max}_{skin}(Z,N) - r^{min}_{skin}(Z,N)|$, where $r^{max}_{skin}(Z,N)$ and $r^{min}_{skin}(Z,N)$ are the largest and smallest proton hexadecapol deformations obtained with four CDFT parametrizations for the (Z,N) nucleus.

transfer gave $r_{skin} = 0.33 \pm 0.17$ with a relatively large error bar [37]. A central value of 0.33 fm is particularly intriguing because it is around 0.13 fm higher than central values obtained in other experiments (see Table 1 in Ref. [136]). The analysis performed in Ref. [135] has found no compelling reason to rule out the models with large neutron skin in ^{208}Pb. However, as indicated in Ref. [135], the parameters of these models do not follow from a strict optimization procedure. All systematic fits with density-dependent couplings in the isovector channel for DD-ME1 [39], DD-ME2 [23], DD-MEδ [12], DD-PC1 [11], or FSUGold [77] find for the neutron skin thickness in ^{208}Pb values close to 0.2 fm (see Table VII). Only in the first two cases the small neutron skins have been used in the fit. For the CEDF's DD-MEδ and DD-PC1 the density dependence in the isovector channel has been determined from *ab initio* calculations of nuclear matter.

It is clear that the already approved follow-up PREX measurement [141] designed to achieve the original 1% error in the neutron radius of ^{208}Pb will provide useful constraints on the selection of the proper CEDF. Table VII also provides the predictions for neutron skin thickness in ^{48}Ca. It will be measured in the approved CREX experiment at JLab with an accuracy of around 0.02 fm [141]. Again the neutron skin thickness is the largest for the NL3* CEDF and the density-dependent (DD) CEDF's provide similar, but smaller, predictions for it. However, the difference between the NL3* and the DD CEDF's is less pronounced in ^{48}Ca as compared with ^{208}Pb. Apart from NL3*, the neutron skin thicknesses are only slightly (by $\sim$0.05 fm) smaller in ^{48}Ca as compared with ^{208}Pb.

On going to the neutron drip line we observe the same trends which are already seen in ^{48}Ca and ^{208}Pb (see Table VIII). First, the neutron skin thicknesses obtained with DD CEDF's cluster around the same value. Second, the neutron skin thickness obtained with NL3* exceeds substantially those found with DD CEDF's. It is interesting that the neutron skin thicknesses obtained with DD CEDF's are very close to those found in Skyrme DFT's calculations with SV-min and UNEDF0 in Ref. [28].

In Fig. 25 we present calculated distributions of neutron skin thicknesses in the (Z,N) chart. One can see that they are very similar for the DD CEDF's. However, the neutron skin thickness is larger for NL3*. In some nuclei it can reach 1.2 fm. This is a consequence of two factors. First, the neutron

TABLE VII. Neutron skin thicknesses r_{skin} in ^{48}Ca and ^{208}Pb obtained in calculations with the indicated CEDF's. The results of the calculations with FSUGold are taken from Ref. [135].

CEDF	$r_{skin}(^{48}\text{Ca})$ (fm)	$r_{skin}(^{208}\text{Pb})$ (fm)
NL3*	0.236	0.288
DD-ME2	0.187	0.193
DD-MEδ	0.177	0.186
DD-PC1	0.198	0.201
FSUGold		0.21

TABLE VIII. Neutron skin thicknesses r_{skin} (in fm) in selected neutron-rich nuclei obtained in calculations with relativistic functionals (CEDF) and Skyrme functionals (SEDF). The latter results are extracted from Fig. 3 of Ref. [28].

EDF	Ca ($N = 42$)	Zr ($N = 84$)	Er ($N = 68$)
CEDF(NL3*)	0.688	0.666	0.752
CEDF(DD-ME2)	0.598	0.522	0.582
CEDF(DD-MEδ)	0.542	0.495	0.529
CEDF(DD-PC1)	0.539	0.509	0.532
SEDF(SV-min)	0.55	0.470	0.490
SEDF(UNEDF0)	0.55	0.510	0.560

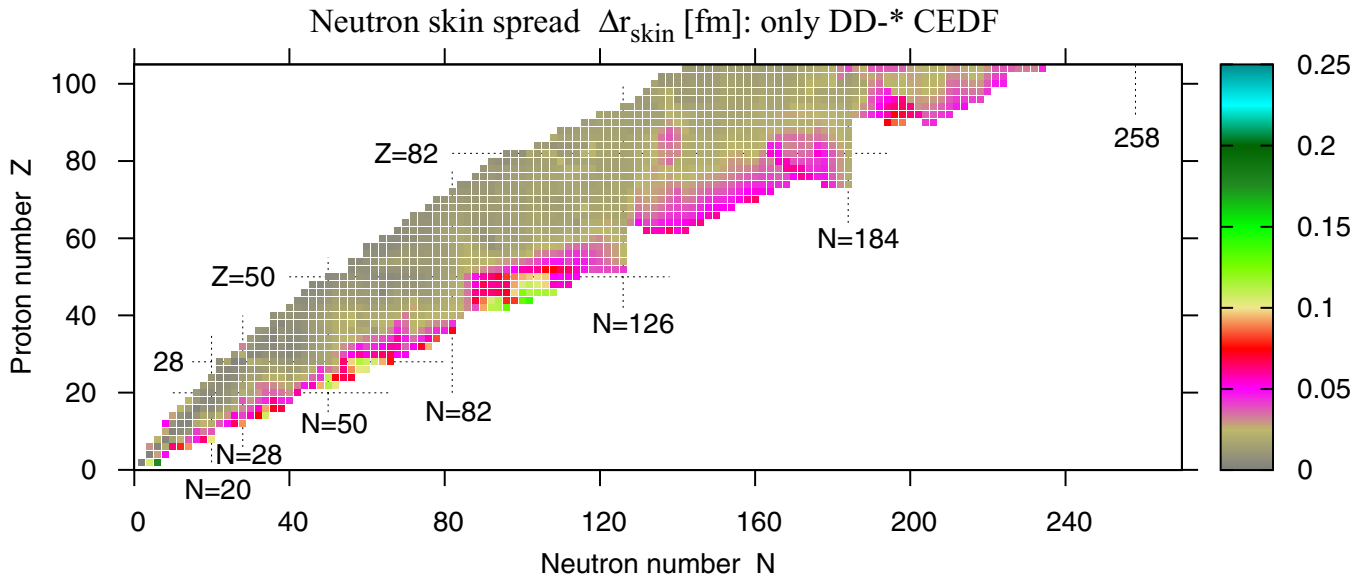

FIG. 27. (Color online) The same as Fig. 26 but for neutron skin thickness spreads obtained with exclusion of the NL3*.

skin is larger for NL3* than for the DD CEDF's already in the valley of β stability and the neutron skin thickness increases with isospin. Second, the two-neutron drip line extends to more neutron-rich nuclei in NL3* as compared with DD CEDF's (see Sec. VIII) leading to these high values of r_{skin}. The comparison of the results for DD CEDF's shows significant similarities with the results obtained for six Skyrme functionals in Ref. [28]. In part, this is a consequence of the fact that, similar to the DD CEDF's, these Skyrme EDF's (SEDF's) favor smaller values for the neutron skin in ^{208}Pb.

As shown in Fig. 26 the spreads (1) of theoretical predictions in the neutron skin thickness increase with isospin and become rather large in neutron-rich nuclei (reaching 0.25 fm in some cases). They are larger than those found in Skyrme calculations in Ref. [28]. This is a consequence of the use of NL3*, which, contrary to DD CEDF's of the present paper and the Skyrme EDF's used in Ref. [28], favors large neutron skins. As illustrated in Fig. 27, the spreads (1) in the neutron skin thicknesses become substantially smaller if we exclude NL3* from our consideration. This again stresses the importance of future PREX-II and CREX experiments. If PREX-II confirms the large neutron skin in ^{208}Pb ($r_{skin} \sim 0.33$ fm) obtained in the first PREX experiment, this would also require to look for density-dependent CEDF's and Skyrme EDF's with larger neutron skins. If this experiment will lead to a smaller neutron skin thickness $r_{skin} \sim 0.2$ fm, then the EDF's with large neutron skins (such as NL3*) should be excluded from further consideration. In either case, this experiment will lead to a reduction of the uncertainty in the prediction of neutron skins in neutron-rich nuclei.

XI. CONCLUSIONS

The global performance of CEDF's has been assessed investigating the state-of-the-art functionals NL3*, DD-ME2, DD-MEδ, and DD-PC1. They represent three classes of functionals which differ by basic model assumptions and fitting protocols. The available experimental data on ground state properties of even-even nuclei have been confronted with the results of the calculations. For the first time, theoretical systematic uncertainties in the prediction of physical observables [as defined in Eq. (1)] have been investigated on a global scale for relativistic functionals. Special attention has been paid to the propagation of these uncertainties towards the neutron drip line.

The main results can be summarized as follows.

(i) The current generation of CEDF's investigated in the present paper provides an improved description of masses across the nuclear chart as compared with the previous generation. This leads not only to reduced global rms deviations but also to improved gross trends of the deviations between theory and experiment as a function of the mass number. The rms deviations for the available experimental masses of 835 even-even nuclei range from 2.15 MeV (DD-PC1) to 3.00 MeV (NL3*). This is achieved with a relatively small number of model parameters fitted to a rather modest set of data on finite nuclei ranging from 12 (for NL3* and DD-ME2) to 161 (for DD-MEδ) nuclei. The spread for binding energies increases on going from the β-stability valley towards the neutron drip line. This is a consequence of poorly defined isovector properties of the current generation of CEDF's. In the light of the model limitations and the relatively narrow isospin range measured in experiment, it still remains an open question whether the isovector properties of EDF's can accurately be defined from masses alone.

(ii) The analysis of discrepancies between theory and experiment for two-neutron separation energies and their sources leads to a more critical look on the reappearance of two-neutron binding with increasing

neutron number beyond the primary two-neutron drip line. This reappearance shows itself in the nuclear chart via peninsulas emerging from the nuclear mainland and it is directly related to the behavior of two-neutron separation S_{2n} energies with neutron number. This effect exists in a number of DFT calculations [26,46,92], but it maybe an artifact of the mean-field approximation. These peninsulas usually appear above the $N = 126$ and $N = 184$ shell closures. However, the range of nuclei around these shell closures, in which transitional shapes are expected, is wide. Thus, the inclusion of correlations beyond mean field may lead to the merging of these peninsulas with the nuclear mainland.

(iii) The calculated two-proton drip lines are very close to experiment. The best reproduction of the two-proton drip line is achieved for the CEDF's DD-ME2, and DD-MEδ, which are characterized by the best residuals for the two-proton separation energies S_{2p}. Because the proton drip line lies close to the valley of stability, the extrapolation errors towards it are small. In addition, the Coulomb barrier provides a rather steep potential, reducing considerably the coupling to the proton continuum. This leads to a relatively low density of the single-particle states in the vicinity of the Fermi level, which helps to minimize the errors in the prediction of two-proton drip line.

(iv) A detailed analysis of the sources of the spread in the predictions of the two-neutron drip lines existing in nonrelativistic and covariant DFT has been performed. Poorly known isovector properties of the EDF's, the underlying shell structure and inevitable inaccuracies in the DFT description of the single-particle energies contribute to these uncertainties. However, no clear correlations between the location of the two-neutron drip line and the nuclear-matter properties of the corresponding EDF have been found.

(v) The spread between the different models in the definition of the two-neutron drip line at $Z \sim 54$, $N = 126$ and $Z \sim 82$, $N = 184$ are very small owing to the impact of the spherical shell closures at $N = 126$ and 184. The largest difference between covariant and Skyrme DFT exist in superheavy nuclei, where the first model (contrary to the second) consistently predicts a significant impact of the $N = 258$ spherical shell closure. The spread of the theoretical predictions grows on moving away from these spherical closures. This is caused by the increasing deformation.

(vi) The experimental static β_2 deformations of well-deformed nuclei are well described in these calculations. The difference between the four CEDF's is small and within the experimental uncertainties. As a result, such experimental data cannot be used to differentiate between the functionals. Theoretical uncertainties for this physical observable are either nonexistent or very small for spherical or nearly spherical nuclei as well as for well-deformed nuclei in the rare-earth and in the actinide regions. The largest spreads for predicting the equilibrium quadrupole deformations exist at the boundaries between regions of different deformations. They are extremely high in the regions of the prolate-oblate shape coexistence, indicating that the ground state in a given nucleus can be prolate (oblate) in one CEDF and oblate (prolate) in another CEDF. These uncertainties are attributable to the deficiencies of the current generations of the DFT models with respect of the description of single-particle energies.

(vii) The analysis of isovector deformations β_2^{IV} reveals that the neutron β_2 deformation is typically larger than the corresponding proton deformation. However, in most of the nuclei the absolute value of β_2^{IV} is small. Only in the ($Z \sim 16, N \sim 34$), ($Z \sim 28$, $N \sim 60$), and ($Z \sim 50$, $N \sim 100$) regions located in the vicinity of two-neutron drip line is the isovector deformation substantial in all relativistic functionals. On the contrary, for Skyrme functionals in the majority of the nuclei the neutron β_2 deformations are smaller than proton ones and the absolute values of β_2^{IV} are larger. Thus, the microscopic + macroscopic model, which assumes the same deformations for protons and neutrons, is better justified in CDFT than in Skyrme DFT.

(viii) A comparable level of accuracy (with a slightly better description by DD-ME2) is achieved by all the functionals under investigation for charge radii. Figure 24 shows that the spread in predicting charge radii are not necessarily larger near the neutron drip line as compared with the valley of β-stability.

(ix) The experimental data on the neutron skin thickness $r_{\rm skin}$ in ^{208}Pb are somewhat contradictory. Hadronic probes give $r_{\rm skin} \sim 0.2$ fm, whereas in the PREX experiment the electroweak probe provides a central value of $r_{\rm skin} = 0.3$ fm, however with very large error bars. The NL3* results come close to the central PREX value, while DD-ME2, DD-MEδ, and DD-PC1 give much smaller neutron skins in the vicinity of $r_{\rm skin} = 0.2$ fm. This can be understood by the fact that the last three functionals have a density dependence in the isovector channel, which leads to a smaller slope L of the symmetry energy at saturation and, therefore, to larger values of the symmetry energy in the region of densities $\rho \sim 0.1$ fm below saturation (see Refs. [39,130]). As a consequence, the neutrons are less bound to the protons in this region of densities. Globally, the spreads in the neutron skin thickness increase with isospin and become rather large in neutron-rich nuclei (reaching $r_{\rm skin} = 0.25$ fm in some cases) reflecting the difference between NL3* and the DD CEDF's. There is hope that these uncertainties can be reduced if future PREX-II and CREX experiments provide neutron skin thicknesses in ^{208}Pb and ^{48}Ca with the required accuracy.

The current investigation shows that the biggest uncertainties in theoretical description exist in transitional nuclei. On the one hand, this is expected because these nuclei have usually flat potential energy surfaces, often in the β and γ

directions. The minima are not well defined in these flat energy surfaces and the fluctuations cannot be neglected. These nuclei have to be treated by the methods going beyond mean field [7,89,105]. On the other hand, the mean field is the starting point of these approaches. However, in some specific cases we find a strong dependence of the equilibrium deformations and the potential energy surfaces of transitional and shape-coexistent nuclei on the employed EDF which originates from the deficiencies of mean-field methods in the description of single-particle energies. These uncertainties will eventually affect the results of beyond-mean-field calculations. The analysis indicates that further improvement in the description of the single-particle energies is needed to describe experimental data in transitional and shape-coexistent nuclei reliably and consistently across the nuclear chart with a high level of predictive power by the methods going beyond mean field.

Historically, it was considered an advantage of the CDFT over nonrelativistic DFT that no single-particle information has been used in the fit of CEDF's. However, it is clear from the current investigation that such an approach has its own limits because further improvement of CEDF's may require additional terms, such as tensor terms, in the functional which cannot be firmly constrained by only nuclear-matter properties and by the fit to masses and radii of finite nuclei [142]. The inclusion of experimental data on giant resonances in the spin and isospin degrees of freedom and/or on the energies of the single-particle states into the fitting protocol may offer such an extra tool and make it possible to define the functional with better single-particle properties. However, we also have to consider that, according to the concept of DFT [1,2], single-particle energies are only auxiliary quantities, which are not automatically reproduced well. As is well known, very often, in particular in the relativistic case, DFT theories suffer from low effective masses and the corresponding low-level densities at the Fermi surface. One has to go beyond mean field and to take into account energy-dependent self-energies [143–145], as, for instance, particle-vibrational coupling, to deal with this problem [67,146].

As an example, the data set of the calculated properties of even-even nuclei obtained with DD-PC1 CEDF is provided as Supplemental Material with this article at Ref. [147].

ACKNOWLEDGMENTS

The authors would like to thank J. Erler for valuable discussions. This work has been supported by the US Department of Energy under Grant No. DE-FG02-07ER41459 and by the DFG cluster of excellence "Origin and Structure of the Universe" (www.universe-cluster.de). This work was also supported partially through CUSTIPEN (China-US Theory Institute for Physics with Exotic Nuclei) under DOE Grant No. DE-FG02-13ER42025 and by an allocation of advanced computing resources provided by the National Science Foundation. The computations were partially performed on Kraken at the National Institute for Computational Sciences (http://www.nics.tennessee.edu/).

[1] W. Kohn and L. J. Sham, Phys. Rev. **137**, A1697 (1965).
[2] W. Kohn and L. J. Sham, Phys. Rev. **140**, A1133 (1965).
[3] P. Ring, Phys. Scr. T **150**, 014035 (2012).
[4] M. Bender, P.-H. Heenen, and P.-G. Reinhard, Rev. Mod. Phys. **75**, 121 (2003).
[5] Lect. Notes Phys., edited by G. A. Lalazissis, P. Ring, and D. Vretenar (Springer-Verlag, Heidelberg, 2004), Vol. 641.
[6] D. Vretenar, A. V. Afanasjev, G. A. Lalazissis, and P. Ring, Phys. Rep. **409**, 101 (2005).
[7] T. Nikšić, D. Vretenar, and P. Ring, Prog. Part. Nucl. Phys. **66**, 519 (2011).
[8] S. Fayans, JETP Lett. **68**, 169 (1998).
[9] M. Baldo, P. Schuck, and X. Viñas, Phys. Lett. B **663**, 390 (2008).
[10] J. Drut, R. Furnstahl, and L. Platter, Prog. Part. Nucl. Phys. **64**, 120 (2010).
[11] T. Nikšić, D. Vretenar, and P. Ring, Phys. Rev. C **78**, 034318 (2008).
[12] X. Roca-Maza, X. Viñas, M. Centelles, P. Ring, and P. Schuck, Phys. Rev. C **84**, 054309 (2011).
[13] T. D. Cohen, R. J. Furnstahl, and D. K. Griegel, Phys. Rev. C **45**, 1881 (1992).
[14] W. Koepf and P. Ring, Nucl. Phys. A **493**, 61 (1989).
[15] A. V. Afanasjev and H. Abusara, Phys. Rev. C **81**, 014309 (2010).
[16] U. Hofmann and P. Ring, Phys. Lett. B **214**, 307 (1988).
[17] A. V. Afanasjev and P. Ring, Phys. Rev. C **62**, 031302(R) (2000).
[18] A. V. Afanasjev and H. Abusara, Phys. Rev. C **82**, 034329 (2010).
[19] R. Brockmann and H. Toki, Phys. Rev. Lett. **68**, 3408 (1992).
[20] F. Hofmann, C. M. Keil, and H. Lenske, Phys. Rev. C **64**, 034314 (2001).
[21] M. Serra, T. Otsuka, Y. Akaishi, P. Ring, and S. Hirose, Prog. Theor. Phys. **113**, 1009 (2005).
[22] S. Hirose, M. Serra, P. Ring, T. Otsuka, and Y. Akaishi, Phys. Rev. C **75**, 024301 (2007).
[23] G. A. Lalazissis, T. Nikšić, D. Vretenar, and P. Ring, Phys. Rev. C **71**, 024312 (2005).
[24] G. A. Lalazissis, S. Karatzikos, R. Fossion, D. P. Arteaga, A. V. Afanasjev, and P. Ring, Phys. Lett. B **671**, 36 (2009).
[25] P. G. Reinhard and W. Nazarewicz, Phys. Rev. C **81**, 051303(R) (2010).
[26] J. Erler, N. Birge, M. Kortelainen, W. Nazarewicz, E. Olsen, A. M. Perhac, and M. Stoitsov, Nature (London) **486**, 509 (2012).
[27] J. Dobaczewski, W. Nazarewicz, and P.-G. Reinhard, arXiv:1402.4657v1 [nucl-th].
[28] M. Kortelainen, J. Erler, W. Nazarewicz, N. Birge, Y. Gao, and E. Olsen, Phys. Rev. C **88**, 031305(R) (2013).
[29] Y. K. Gambhir, P. Ring, and A. Thimet, Ann. Phys. (NY) **198**, 132 (1990).
[30] J. D. Walecka, Ann. Phys. (NY) **83**, 491 (1974).

[31] B. D. Serot and J. D. Walecka, Adv. Nucl. Phys. **16**, 1 (1986).
[32] J. Boguta and R. Bodmer, Nucl. Phys. A **292**, 413 (1977).
[33] G. A. Lalazissis, J. König, and P. Ring, Phys. Rev. C **55**, 540 (1997).
[34] S. Typel and H. H. Wolter, Nucl. Phys. A **656**, 331 (1999).
[35] P.-G. Reinhard, M. Rufa, J. Maruhn, W. Greiner, and J. Friedrich, Z. Phys. A **323**, 13 (1986).
[36] Y. Sugahara and H. Toki, Nucl. Phys. A **579**, 557 (1994).
[37] S. Abrahamyan *et al.*, Phys. Rev. Lett. **108**, 112502 (2012).
[38] B.-A. Li, A. Ramos, G. Verde, and I. Vidañ (Eds), Eur. J. Phys. A **50** (2014) [Topical issue on nuclear symmetry energy].
[39] T. Nikšić, D. Vretenar, P. Finelli, and P. Ring, Phys. Rev. C **66**, 024306 (2002).
[40] B. A. Nikolaus, T. Hoch, and D. G. Madland, Phys. Rev. C **46**, 1757 (1992).
[41] H. Kucharek and P. Ring, Z. Phys. A **339**, 23 (1991).
[42] P. Ring, Prog. Part. Nucl. Phys. **37**, 193 (1996).
[43] A. V. Afanasjev, P. Ring, and J. König, Nucl. Phys. A **676**, 196 (2000).
[44] P. Ring and P. Schuck, *The Nuclear Many-Body Problem* (Springer-Verlag, Berlin, 1980).
[45] J. Meng and P. Ring, Phys. Rev. Lett. **77**, 3963 (1996).
[46] Y. N. Zhang, J. C. Pei, and F. R. Xu, Phys. Rev. C **88**, 054305 (2013).
[47] L. Li, J. Meng, P. Ring, E.-G. Zhao, and S.-G. Zhou, Phys. Rev. C **85**, 024312 (2012).
[48] A. V. Afanasjev, T. L. Khoo, S. Frauendorf, G. A. Lalazissis, and I. Ahmad, Phys. Rev. C **67**, 024309 (2003).
[49] A. V. Afanasjev and S. Shawaqfeh, Phys. Lett. B **706**, 177 (2011).
[50] A. V. Afanasjev and O. Abdurazakov, Phys. Rev. C **88**, 014320 (2013).
[51] P. Ring, Y. K. Gambhir, and G. A. Lalazissis, Comput. Phys. Commun. **105**, 77 (1997).
[52] P. Bonche, H. Flocard, and P. H. Heenen, Comput. Phys. Commun. **171**, 49 (2005).
[53] T. Bürvenich, M. Bender, J. A. Maruhn, and P.-G. Reinhard, Phys. Rev. C **69**, 014307 (2004).
[54] H. Abusara, A. V. Afanasjev, and P. Ring, Phys. Rev. C **85**, 024314 (2012).
[55] A. V. Afanasjev, S. Agbemava, D. Ray, and P. Ring (unpublished).
[56] A. K. Kerman, Ann. Phys. (NY) **12**, 300 (1961).
[57] T. Gonzalez-Llarena, J. L. Egido, G. A. Lalazissis, and P. Ring, Phys. Lett. B **379**, 13 (1996).
[58] J. F. Berger, M. Girod, and D. Gogny, Comput. Phys. Commun. **63**, 365 (1991).
[59] J. F. Berger, M. Girod, and D. Gogny, Nucl. Phys. A **428**, 23c (1984).
[60] Y. Tian, Z. Y. Ma, and P. Ring, Phys. Lett. B **676**, 44 (2009).
[61] J. Dobaczewski, P. Magierski, W. Nazarewicz, W. Satula, and Z. Szymański, Phys. Rev. C **63**, 024308 (2001).
[62] A. V. Afanasjev, J. König, P. Ring, L. M. Robledo, and J. L. Egido, Phys. Rev. C **62**, 054306 (2000).
[63] A. V. Afanasjev, Phys. Scr. **89**, 054001 (2014).
[64] L. J. Wang, B. Y. Sun, J. M. Dong, and W. H. Long, Phys. Rev. C **87**, 054331 (2013).
[65] D. Ray and A. V. Afanasjev (unpublished).
[66] J. Decharge and D. Gogny, Phys. Rev. C **21**, 1568 (1980).
[67] E. V. Litvinova and A. V. Afanasjev, Phys. Rev. C **84**, 014305 (2011).
[68] T. Duguet, P. Bonche, P.-H. Heenen, and J. Meyer, Phys. Rev. C **65**, 014311 (2001).
[69] J. Dobaczewski, W. Nazarewicz, T. R. Werner, J. F. Berger, C. R. Chinn, and J. Dechargé, Phys. Rev. C **53**, 2809 (1996).
[70] M. Bender, K. Rutz, P.-G. Reinhard, and J. A. Maruhn, Eur. Phys. J. A **8**, 59 (2000).
[71] M. Wang, G. Audi, A. H. Wapstra, F. G. Kondev, M. MacCormick, X. Xu, and B. Pfeiffer, Chin. Phys. C **36** (2012).
[72] D. Hirata, K. Sumiyoshi, I. Tanihata, Y. Sugahara, T. Tachibana, and H. Toki, Nucl. Phys. A **616**, 438c (1997).
[73] G. A. Lalazissis, S. Raman, and P. Ring, At. Data Nucl. Data Table **71**, 1 (1999).
[74] L. Geng, H. Toki, and J. Meng, Prog. Theor. Phys. **113**, 785 (2005).
[75] J. Dobaczewski, H. Flocard, and J. Treiner, Nucl. Phys. A **422**, 103 (1984).
[76] P.-G. Reinhard and B. K. Agrawal, Int. J. Mod. Phys. E **20**, 1379 (2011).
[77] B. G. Todd-Rutel and J. Piekarewicz, Phys. Rev. Lett. **95**, 122501 (2005).
[78] B. K. Agrawal, Phys. Rev. C **81**, 034323 (2010).
[79] P. W. Zhao, Z. P. Li, J. M. Yao, and J. Meng, Phys. Rev. C **82**, 054319 (2010).
[80] Q. S. Zhang, Z. M. Niu, Z. P. Li, J. M. Yao, and J. Meng, arXiv:1305.1736v2 [nucl-th].
[81] S. Baroni, F. Barranco, P. F. Bortignon, R. A. Broglia, G. Coló, and E. Vigezzi, Phys. Rev. C **74**, 024305 (2006).
[82] P. Möller, J. R. Nix, W. D. Myers, and W. J. Swiatecki, At. Data Nucl. Data Table **59**, 185 (1995).
[83] S. Goriely, N. Chamel, and J. M. Pearson, Phys. Rev. Lett. **102**, 152503 (2009).
[84] S. Goriely, S. Hilaire, M. Girod, and S. Péru, Phys. Rev. Lett. **102**, 242501 (2009).
[85] E. Wigner, Phys. Rev. **51**, 947 (1937).
[86] W. D. Myers and W. J. Światecki, Nucl. Phys. A **612**, 249 (1997).
[87] M. Bender, P. Bonche, and P.-H. Heenen, Phys. Rev. C **74**, 024312 (2006).
[88] N. Hinohara, T. Nakatsukasa, M. Matsuo, and K. Matsuyanagi, Phys. Rev. C **80**, 014305 (2009).
[89] Y. Fu, H. Mei, J. Xiang, Z. P. Li, J. M. Yao, and J. Meng, Phys. Rev. C **87**, 054305 (2013).
[90] W. von Oertzen, M. Freer, and Y. Kanada-En'yo, Phys. Rep. **432**, 43 (2006).
[91] S. Kümmel and L. Kronik, Rev. Mod. Phys. **80**, 3 (2008).
[92] A. V. Afanasjev, S. Agbemava, D. Ray, and P. Ring, Phys. Lett. B **726**, 680 (2013).
[93] J. Erler, C. J. Horowitz, W. Nazarewicz, M. Rafalski, and P.-G. Reinhard, Phys. Rev. C **87**, 044320 (2013).
[94] G. A. Lalazissis and S. Raman, Phys. Rev. C **58**, 1467 (1998).
[95] D. Vretenar, G. A. Lalazissis, and P. Ring, Phys. Rev. C **57**, 3071 (1998).
[96] G. A. Lalazissis, D. Vretenar, and P. Ring, Nucl. Phys. A **650**, 133 (1999).
[97] G. A. Lalazissis, D. Vretenar, and P. Ring, Phys. Rev. C **60**, 051302R (1999).
[98] G. A. Lalazissis, D. Vretenar, and P. Ring, Nucl. Phys. A **679**, 481 (2001).

[99] G. A. Lalazissis, D. Vretenar, and P. Ring, Phys. Rev. C **69**, 017301 (2004).
[100] A. Corsi, J.-P. Delaroche, A. Obertelli, T. Baugher, D. Bazin, S. Boissinot, F. Flavigny, A. Gade, M. Girod, T. Glasmacher, G. F. Grinyer, W. Korten, J. Libert, J. Ljungvall, S. McDaniel, A. Ratkiewicz, A. Signoracci, R. Stroberg, B. Sulignano, and D. Weisshaar, Phys. Rev. C **88**, 044311 (2013).
[101] J. Ljungvall *et al.*, Phys. Rev. Lett. **100**, 102502 (2008).
[102] E. Clément *et al.*, Phys. Rev. C **75**, 054313 (2007).
[103] A. V. Afanasjev and S. Frauendorf, Phys. Rev. C **71**, 064318 (2005).
[104] C. D. O'Leary, C. E. Svensson, S. G. Frauendorf, A. V. Afanasjev, D. E. Appelbe, R. A. E. Austin, G. C. Ball, J. A. Cameron, R. M. Clark, M. Cromaz, P. Fallon, D. F. Hodgson, N. S. Kelsall, A. O. Macchiavelli, I. Ragnarsson, D. Sarantites, J. C. Waddington, and R. Wadsworth, Phys. Rev. C **67**, 021301(R) (2003).
[105] J. M. Yao, M. Bender, and P.-H. Heenen, Phys. Rev. C **87**, 034322 (2013).
[106] P. Rahkila *et al.*, Phys. Rev. C **82**, 011303(R) (2010).
[107] J.-P. Delaroche, M. Girod, J. Libert, H. Goutte, S. Hilaire, S. Péru, N. Pillet, and G. F. Bertsch, Phys. Rev. C **81**, 014303 (2010).
[108] M. Jaminon and C. Mahaux, Phys. Rev. C **40**, 354 (1989).
[109] M. Dutra, O. Lourenço, J. S. S. Martins, A. Delfino, J. R. Stone, and P. D. Stevenson, Phys. Rev. C **85**, 035201 (2012).
[110] J. Bartel, P. Quentin, M. Brack, C. Guet, and H.-B. Hakansson, Nucl. Phys. A **386**, 79 (1982).
[111] M. Kortelainen, J. McDonnell, W. Nazarewicz, E. Olsen, P.-G. Reinhard, J. Sarich, N. Schunck, S. M. Wild, D. Davesne, J. Erler, and A. Pastore, arXiv:1312.1746v1 [nucl-th].
[112] E. Chabanat, P. Bonche, P. Haensel, J. Meyer, and R. Schaeffer, Nucl. Phys. A **635**, 231 (1998).
[113] F. Chappert, M. Girod, and S. Hilaire, Phys. Lett. B **668**, 420 (2008).
[114] P. Klüpfel, P.-G. Reinhard, T. J. Bürvenich, and J. A. Maruhn, Phys. Rev. C **79**, 034310 (2009).
[115] S. Goriely, N. Chamel, and J. M. Pearson, Phys. Rev. C **82**, 035804 (2010).
[116] S. Raman, C. H. Malarkey, W. T. Milner, C. W. Nestor, Jr., and P. H. Stelson, At. Data Nucl. Data Tables **36**, 1 (1987).
[117] W. Nazarewicz and I. Ragnarsson, in *Handbook on Nuclear Properties*, edited by D. N. Poenaru and W. Greiner (Claredon Press, Oxford, 1996), p. 80.
[118] L. Grodzins, Phys. Lett. **2**, 88 (1962).
[119] R.-D. Herzberg *et al.*, Phys. Rev. C **65**, 014303 (2001).
[120] I. N. Boboshin, V. V. Varlamov, B. S. Ishkhanov, S. Y. Komarov, and V. Orlin, Bull. Russ. Acad. Sci.: Phys. **71**, 320 (2007).
[121] K. Heyde and J. L. Wood, Rev. Mod. Phys. **83**, 1467 (2011).
[122] T. Nikšić, D. Vretenar, G. A. Lalazissis, and P. Ring, Phys. Rev. Lett. **99**, 092502 (2007).
[123] J. B. Snyder, W. Reviol, D. G. Sarantites, A. V. Afanasjev, R. V. F. Janssens, H. Abusara, M. P. Carpenter, X. Chen, C. J. Chiara, J. P. Greene, T. Lauritsen, E. A. McCutchan, D. Seweryniak, and S. Zhu, Phys. Lett. B **723**, 61 (2013).
[124] Z. P. Li, T. Nikšić, D. Vretenar, J. Meng, G. A. Lalazissis, and P. Ring, Phys. Rev. C **79**, 054301 (2009).
[125] J. Libert and P. Quentin, Phys. Rev. C **25**, 571 (1982).
[126] W. Bertozzi, J. Friar, J. Heisenberg, and J. W. Negele, Phys. Lett. B **41**, 408 (1972).
[127] M. Nishimura and D. W. L. Sprung, Prog. Theor. Phys. **77**, 781 (1987).
[128] I. Angeli and K. P. Marinova, At. Data Nucl. Data Tables **99**, 69 (2013).
[129] T. Nikšić, D. Vretenar, P. Ring, and G. A. Lalazissis, Phys. Rev. C **65**, 054320 (2002).
[130] A. Brown, Phys. Rev. Lett. **85**, 5296 (2000).
[131] X. Roca-Maza, M.Centelles, X. Viñas, and M. Warda, Phys. Rev. Lett. **106**, 252501 (2011).
[132] C. J. Horowitz and J. Piekarewicz, Phys. Rev. Lett. **86**, 5647 (2001).
[133] A. W. Steiner, M. Prakash, J. M. Lattimer, and P. J. Ellis, Phys. Rep. **411**, 325 (2005).
[134] F. J. Fattoyev and J. Piekarewicz, Phys. Rev. C **86**, 015802 (2012).
[135] F. J. Fattoyev and J. Piekarewicz, Phys. Rev. Lett. **111**, 162501 (2013).
[136] A. Krasznahorkay, N. Paar, D. Vretenar, and M. N. Harakeh, Phys. Scr. T **154**, 014018 (2013).
[137] M. B. Tsang, J. R. Stone, F. Camera, P. Danielewicz, S. Gandolfi, K. Hebeler, C. J. Horowitz, J. Lee, W. G. Lynch, Z. Kohley, R. Lemmon, P. Möller, T. Murakami, S. Riordan, X. Roca-Maza, F. Sammarruca, A. W. Steiner, I. Vidaña, and S. J. Yennello, Phys. Rev. C **86**, 015803 (2012).
[138] A. Krasznahorkay, M. Csatlós, L. Csige, T. K. Eriksen, F. Giacoppo, A. Görgen, T. W. Hagen, M. N. Harakeh, R. Julin, P. Koehler, N. Paar, S. Siem, L. Stuhl, T. Tornyi, and D. Vretenar, arXiv:1311.1456v2 [nucl-ex].
[139] C. M. Tarbert *et al.*, arXiv:1311.0168v2 [nucl-ex].
[140] C. J. Horowitz, Phys. Rev. C **57**, 3430 (1998).
[141] The PREX-II proposal (unpublished), available at hallaweb.jlab.org/parity/prex.
[142] G. A. Lalazissis, S. Karatzikos, M. Serra, T. Otsuka, and P. Ring, Phys. Rev. C **80**, 041301 (2009).
[143] D. Vretenar, T. Nikšić, and P. Ring, Phys. Rev. C **65**, 024321 (2002).
[144] S. Typel, Phys. Rev. C **71**, 064301 (2005).
[145] T. Marketin, D. Vretenar, and P. Ring, Phys. Rev. C **75**, 024304 (2007).
[146] E. Litvinova and P. Ring, Phys. Rev. C **73**, 044328 (2006).
[147] See Supplemental Material at http://link.aps.org/supplemental/10.1103/PhysRevC.89.054320 for a table with the results of the calculations based on the DD-PC1 CEDF.